Mississippi State University

Scholars Junction

Theses and Dissertations Theses and Dissertations

5-11-2013

Navigation System Design with Application to the Ares I Crew Launch Vehicle and Space Launch Systems

Ted Emerson Oliver

Follow this and additional works at: https://scholarsjunction.msstate.edu/td

Recommended Citation

Oliver, Ted Emerson, "Navigation System Design with Application to the Ares I Crew Launch Vehicle and Space Launch Systems" (2013). *Theses and Dissertations*. 3271.
https://scholarsjunction.msstate.edu/td/3271

This Graduate Thesis - Open Access is brought to you for free and open access by the Theses and Dissertations at Scholars Junction. It has been accepted for inclusion in Theses and Dissertations by an authorized administrator of Scholars Junction. For more information, please contact scholcomm@msstate.libanswers.com.

Navigation system design with application to the Ares I Crew Launch Vehicle and Space Launch Systems

By

Ted Emerson Oliver, Jr.

A Thesis
Submitted to the Faculty of
Mississippi State University
in Partial Fulfillment of the Requirements
for the Degree of Master of Science
in Aerospace Engineering
in the Department of Aerospace Engineering

Mississippi State, Mississippi

May 2013

Copyright by

Ted Emerson Oliver, Jr.

2013

Navigation system design with application
to the Ares I Crew Launch Vehicle
and Space Launch Systems

By

Ted Emerson Oliver, Jr.

Approved:

Keith Koenig
Professor of Aerospace Engineering
(Major Professor)

Carrie Olsen
Committee Participant of Aerospace Engineering
(Committee Member)

Ming Xin
Associate Professor of Aerospace Engineering
(Committee Member)

J. Mark Janus
Professor of Aerospace Engineering
(Graduate Coordinator)

Sarah A. Rajala
Dean of the James Worth Bagley College of Engineering

Name: Ted Emerson Oliver, Jr.

Date of Degree: May 10, 2013

Institution: Mississippi State University

Major Field: Aerospace Engineering

Major Professor: Dr. Keith Koenig

Title of Study: Navigation system design with application to the Ares I Crew Launch Vehicle and Space Launch Systems

Pages of Study: 212

Candidate for Degree of Master of Science

For a launch vehicle, the Navigation System is responsible for determining the vehicle state and providing state and state derived information for Guidance and Controls. The accuracy required of the Navigation System by the vehicle is dependent upon the vehicle, vehicle mission, and other consideration, such as impact foot print. NASAs Ares I launch vehicle and SLS are examples of launch vehicles with are/where to employ inertial navigation systems. For an inertial navigation system, the navigation system accuracy is defined by the inertial instrument errors to a degree determined by the method of estimating the initial navigation state. Utilization of GPS aiding greatly reduces the accuracy required in inertial hardware to meet the same accuracy at orbit insertion. For a launch vehicle with lunar bound payload, the navigation accuracy can have large implications on propellant required to correct for state errors during trans-lunar injection.

Key words: thesis, navigation, inertial navigation, INS, GPS, Ares, SLS, GN&C, NASA

DEDICATION

For my son, Ted Emerson Oliver, III.

May you do great things. May you find happiness on the way.

ACKNOWLEDGEMENTS

I would like to thank my committee for their support and comments on this work. I would like to thank the Aerospace Engineering Department Faculty as a whole for my education. I would like to thank Bill Bernard for all that he taught me and for seeing me through the process to become a navigation engineer at the beginning of my career.

I thank NASA and Marshall Space Flight Center for the opportunity to work on my dream of putting people into space. I could not ask for a better group of people to pursue that dream with than the Contractor Support Staff and Civil Servants in EV42, EV41, and on the GN&C Hardware team. A special thanks to those that cut their teeth with me on Ares I.

I thank my company, Dynamic Concepts Inc., and owners for the opportunities that I've had to learn and progress as a professional in engineering. You guys have truly built something special.

I would especially like to thank Dr. Carrie Olsen. She was first a professor, then a co-worker, then a boss and customer, but most importantly, she is my friend. Her encouragement, help, and guidance were critical to the completion of this work. Thank you.

Lastly, I would like to thank my family for their support and for the motivation to finally complete this chapter of our lives. We're finally finished with this one.

TABLE OF CONTENTS

DEDICATION ii

ACKNOWLEDGEMENTS iii

LIST OF TABLES vii

LIST OF FIGURES ix

CHAPTER

1. INTRODUCTION 1
    1.1 The Objective of this Thesis 3
    1.2 The Structure of this Thesis 4

2. A SYSTEMS APPROACH TO NAVIGATION SYSTEMS FOR LAUNCH VEHICLES 6
    2.1 Launch Vehicle Design Requirements 6
        2.1.1 Ares I Overview 6
        2.1.2 Space Launch Systems 10
    2.2 The General Design Process 14
    2.3 The General Analysis Process 17
    2.4 System Sensitivities and Design Considerations 22
        2.4.1 Sizing and Constraints Analysis 24
            2.4.1.1 Re-Entry Footprint on Insertion Accuracy 25
            2.4.1.2 Insertion Accuracy on Impact Footprint 27
            2.4.1.3 Insertion Accuracy on Payload 30
            2.4.1.4 Decomposition of Vehicle Insertion Accuracy . . . 36
        2.4.2 Requirements Analysis and Constraints Summary 43
        2.4.3 Navigation Architecture and Technologies 48
            2.4.3.1 Position Fixing 49
            2.4.3.2 Dead Reckoning and Inertial Navigation 52
            2.4.3.3 Aided Inertial Navigation 56

3. NAVIGATION SYSTEM MODEL DEVELOPMENT 58

3.1 Navigation Model Architecture 58
3.2 The INS Input Interface 60
3.2.1 Trajectory Truth 60
3.2.2 Sub-Step Size Latency and Sensor Dynamics 63
3.2.3 High Frequency Environment 65
3.2.4 Gravity Anomaly 65
3.3 The Instrument Error Model 66
3.4 Navigation Software 77
3.4.1 Quaternions 78
3.4.2 Inertial Navigation 80
3.4.3 Gyrocompassing, Coarse Alignment 83
3.4.4 Gyrocompassing, Fine Alignment 86
3.4.5 GPS Aiding 89
3.5 The System Error Model and Output Interface 89
3.5.1 Quantization 90
3.5.2 System Precision 92
3.5.3 Time Errors 96
3.5.4 Anti-Aliasing 97
3.5.5 Step Size Delays and Output Interface 99

4. NAVIGATION SYSTEM SENSITIVITIES AND ANALYSIS 101

4.1 Monte Carlo Analysis and Sampling Error 101
4.2 Navigation Error Sensitivity Study 111
4.2.1 Insertion Error Sensitivity Analysis with Uncorrelated Alignment Errors 111
4.2.2 Alignment Error Sensitivities 121
4.2.3 Insertion Error Sensitivity Analysis with Correlated Alignment Errors 125
4.2.4 Insertion Error Sensitivity Analysis with GPS Aiding . . . 133
4.3 Effect of Non-Sensor Misalignment 138
4.3.1 Ares I Physical Mounting Misalignment Sensitivity Study . 139
4.3.1.1 Analysis Methods 141
4.3.1.2 Misalignment Coarse Parameter Study 144
4.3.1.3 Misalignment Fine Parameter Study 148
4.3.1.4 Ares I Misalignment Study Conclusion 152
4.3.2 SLS Misalignment Study 156
4.3.2.1 Misalignment Summary and Applicability to Aided Inertial Navigation 161
4.4 Insertion Accuracy Trade Study 161
4.4.1 Insertion Accuracy Reference Trajectories 162

        4.4.2 Error Budgets 168
        4.4.3 Predicted Alignment Capability 173
        4.4.4 Predicted Ascent Accuracy Capability 174
        4.4.5 Predicted Vehicle Insertion Accuracy Impact on Payload . 188
        4.4.6 Trade Study Conclusions 190
    4.5 Lunar Injection/Trajectory Correction Maneuver Sensitivities . . . 192

5. CONCLUSIONS 202

REFERENCES 206

LIST OF TABLES

2.1 Ares I Insertion Accuracy and Navigation Accuracy 37

2.2 Approximate Ares I Insertion Accuracy Non-Navigation Allocation 38

2.3 Ares I Insertion Error, Top Correlated Dispersions 40

2.4 SLS Insertion Error, Top Correlated Dispersions 44

2.5 Range and Tracking Source Accuracy 52

4.1 Insertion Error Sensitivities Error Sources 113

4.2 Monte Carlo Analysis with Uncorrelated Alignment Error, Alignment Dispersion 115

4.3 Monte Carlo Analysis with Uncorrelated Alignment Error, Monte Carlo Result 116

4.4 Monte Carlo Analysis, Initial Attitude Error from Gyrocompassing 122

4.5 Monte Carlo Analysis with Correlated Alignment Error, Alignment from Gyrocompassing 125

4.6 Monte Carlo Analysis with Correlated Alignment Error, Monte Carlo Result 126

4.7 Insertion Accuracy Error Analysis, Correlated Vs. Uncorrelated Initial Attitude Errors 132

4.8 Monte Carlo Analysis with GPS Aiding, GPS Errors 134

4.9 Monte Carlo Analysis with GPS Aiding, Monte Carlo Result 135

4.10 Misalignment Dispersion Analysis Statistics 150

4.11 Trajectory 1, Ares I Variant, Insertion State 163

4.12 Trajectory 2, SLS Variant, Insertion State 164

4.13 Trajectory 3, SLS Variant, Insertion State 164

4.14 Inertial Instrument Trade Study, Gyrocompass Alignment Capability 174

4.15 Inertial Navigation Trade, Insertion Accuracy Summary, Trajectory 1 . . . 177

4.16 Inertial Navigation Trade, Insertion Accuracy Summary, Trajectory 2 . . . 180

4.17 Inertial Navigation Trade, Insertion Accuracy Summary, Trajectory 3 . . . 183

4.18 Inertial Navigation Trade, Insertion Accuracy Summary, Trajectory 3 . . . 187

4.19 Inertial Navigation Trade, Payload Impact, Trajectory 1 189

4.20 Inertial Navigation Trade, Payload Impact, Trajectory 2 189

4.21 Inertial Navigation Trade, Payload Impact, Trajectory 3 189

4.22 Inertial Navigation Trade, Payload Impact with GPS Aiding, Trajectory 3 . 190

LIST OF FIGURES

1.1 GN&C System Data Flow 2

2.1 Ares Vehicles 8

2.2 Ares I Mission 9

2.3 SLS Vehicles 11

2.4 SLS Block 1 Diagram 12

2.5 ICPS Mission 13

2.6 Navigation Design and Analysis Cycle 18

2.7 NEAT: Top Level 20

2.8 Ares I Debris Footprint Example from Trajectory Analysis 26

2.9 In-plane Error Vs. Footprint for -47x130nmi target 29

2.10 Simple Wedge Angle Diagram 32

2.11 Wedge Angle Parametrization 33

2.12 Delta-V Parametrization for -11x100nmi Insertion Error 34

2.13 Mass Fraction Parametrization for -11x100nmi Insertion Error 35

2.14 HLV Concepts, Estimated Delta SMA and Footprint vs. MTO 42

2.15 Abridged Requirements Flow-down to Navigation Sub-System 47

2.16 Inertial Navigation, Position and Velocity Error Growth in Time 56

3.1 INS Model Architecture 59

3.2 Ares I Sensor Model for Closed-Loop Simulation 61

3.3 Basic Error Model Components 67

3.4 Warm Gas Test Bed, Vibration Rectification from IMU 71

3.5 Example of Angular Random Walk 73

3.6 MIL-STD-1750a Floating Point Data Type Definition 95

4.1 Large Sample Monte Carlo Histogram, Position 103

4.2 Large Sample Monte Carlo Histogram, Velocity 104

4.3 Large Sample Monte Carlo Histogram, Attitude 104

4.4 Large Sample Monte Carlo with 100 Permutations σ_{error} for Position . . . 107

4.5 Large Sample Monte Carlo with 100 Permutations σ_{error} for Velocity . . . 108

4.6 Large Sample Monte Carlo with 100 Permutations, σ_{error} for Attitude . . . 109

4.7 Ares I Based Trajectory Specific Force 112

4.8 Ares I Based Trajectory Angular Rate 114

4.9 Insertion Error Sensitivities with Uncorrelated Alignment Errors, Position (ECI) 118

4.10 Insertion Error Sensitivities with Uncorrelated Alignment Errors, Velocity (ECI) 119

4.11 Insertion Error Sensitivities with Uncorrelated Alignment Errors, Attitude (ECI) 120

4.12 Monte Carlo Analysis, Initial Alignment Sensitivities from Gyrocompassing (Body) 124

4.13 Insertion Error Sensitivities with Correlated Alignment Errors, Position (ECI) 127

4.14 Insertion Error Sensitivities with Correlated Alignment Errors, Velocity (ECI) 128

4.15 Insertion Error Sensitivities with Correlated Alignment Errors, Attitude (ECI) 129

4.16 Ares I Based Trajectory, ECI Velocity 131

4.17 Insertion Error Sensitivities with Uncorrelated Alignment Errors, Orbital Elements 132

4.18 Insertion Error Sensitivities with GPS Aiding, Position and Velocity (ECI) . 136

4.19 Insertion Error Sensitivities with GPS Aiding, Attitude (ECI) 137

4.20 Misalignment Coarse Parameter Study: Wedge Angle 145

4.21 Misalignment Coarse Parameter Study: Propellant Remaining 146

4.22 Misalignment Coarse Parameter Study: Wedge Angle Close-Up 147

4.23 Misalignment Coarse Parameter Study: $Q\alpha_{Total}$ 148

4.24 Misalignment Fine Parameter Study: $Q\alpha_{Total}$ 149

4.25 Misalignment Fine Parameter Study: $Q\alpha_{Total}$ Limit 151

4.26 Misalignment Dispersion Analysis 153

4.27 Misalignment Dispersion Analysis: $Q\alpha_{Total}$ 154

4.28 Unmodified Dispersion Analysis: $Q\alpha_{Total}$ 155

4.29 SLS Misalignment Study: Sensor Misalignment Dispersions 157

4.30 SLS Misalignment Study: $Q\alpha_{Total}$ versus Blended Misalignment, Scatter . 159

4.31 SLS Misalignment Study: $Q\alpha_{Total}$ Time Histories Comparison, Carpet . . 160

4.32 Trajectory 1, Ares I Variant 165

4.33 Trajectory 2, SLS Variant with Second Stage 166

4.34 Trajectory 3, SLS Variant 167

4.35 Inertial Navigation Trade, Position Error at Insertion, Trajectory 1 175

4.36 Inertial Navigation Trade, Velocity Error at Insertion, Trajectory 1 176

4.37 Inertial Navigation Trade, Attitude Error at Insertion, Trajectory 1 176

4.38 Inertial Navigation Trade, Position Error at Insertion, Trajectory 2 178

4.39 Inertial Navigation Trade, Velocity Error at Insertion, Trajectory 2 178

4.40 Inertial Navigation Trade, Attitude Error at Insertion, Trajectory 2 179

4.41 Inertial Navigation Trade, Position Error at Insertion, Trajectory 3 181

4.42 Inertial Navigation Trade, Velocity Error at Insertion, Trajectory 3 181

4.43 Inertial Navigation Trade, Attitude Error at Insertion, Trajectory 3 182

4.44 Inertial Navigation Trade, Position Error at Insertion, Trajectory 3 185

4.45 Inertial Navigation Trade, Velocity Error at Insertion, Trajectory 3 185

4.46 Inertial Navigation Trade, Attitude Error at Insertion, Trajectory 3 186

4.47 ICPS Analysis, 6DOF Trajectory, Specific Force 196

4.48 ICPS Analysis, 6DOF Trajectory, Angular Rate 196

4.49 ICPS Analysis, 6DOF Trajectory, Position 197

4.50 ICPS Analysis, 6DOF Trajectory, Velocity 197

4.51 ICPS Analysis, 6DOF Trajectory, Attitude 198

4.52 ICPS Analysis, TCM ΔV from Navigation Error 200

4.53 ICPS Analysis, TCM ΔV from Navigation Error, Close-up 201

CHAPTER 1

INTRODUCTION

So often asked in jest to the navigation engineer by the former Marshall Space Flight Center Ares I Flight Mechanics Integration Group Lead was the question: Where are we? For a launch vehicle, this is the critical question evaluated by navigation. More specifically, the question can be expanded to performing the task of describing the vehicle state, i.e. the position, velocity, and orientation with respect to a known reference frame. Further expanded, the navigation system can be asked to determine the best estimates for the vehicle state based upon multiple observations or for state derivatives such as angular rate and acceleration or derived quantities such as altitude, relative velocity, aerodynamic angles, etc.. A well designed navigation system performs these tasks within the flight environment to the accuracy required by other sub-systems and such that the entire system meets overall system accuracy requirements, that is, the vehicle is able to achieve the mission.

Figure 1.1 is an example Guidance, Navigation, and Control (GN&C) system data flow diagram which depicts the general relationship between the GN&C subsystems. The Vehicle represents the vehicle plant model, or system dynamics. IMU stands for Inertial Measurement Unit (IMU) and refers to the hardware which produces the inertial measurements utilized by the Navigation sub-system for state estimation. The $\Delta\Theta$ and ΔV quantities

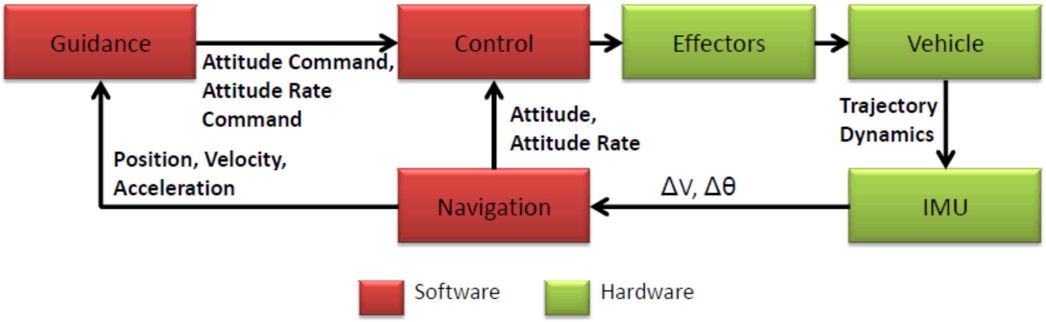
Guidance
Attitude Command,
Attitude Rate
Command
Control
Effectors
Vehicle
Attitude,
Attitude Rate
Trajectory
Dynamics
Position, Velocity,
Acceleration
Navigation
ΔV, Δθ
IMU
Software
Hardware

Figure 1.1

GN&C System Data Flow

from the IMU are the inertial measurements. The figure is notional and depicts a general understanding of the data flow for launch vehicle GN&C.

The Guidance system is responsible for answering the questions, where do I want to go, and based on where I am, how do I direct myself such that I get where I want to go. The latter question is sometimes answered by a sub-system denoted as Steering. Where the Guidance sub-system may produce low-rate attitude and attitude rate commands in terms of the vehicle state, e.g. attitude, attitude rate, and/or velocity, the Steering sub-system propagates a low-rate command forward at a higher rate according to a number of possible concerns, such as limitations on vehicle maneuverability and structural loading or minimization of transients in commands to the Control sub-system. The control function operates on the steering commands, augmenting them such that stability margins are maintained in the presence of flight dynamics. It is not uncommon for the Controls sub-system to use additional state data at different locations along the vehicle if vehicle flexibility is a stability concern. The Control system is ultimately responsible for producing effector commands and may consider dynamics such as rigid body dynamics, flexible body dynamics, propellant slosh, dynamic wind loading, pogo dynamics, and their interactions. The Navigation sub-system provides the input for the overall GN&C system.

Ultimately, the Guidance and Controls sub-systems can only drive error down to that which is inherent in their respective initial conditions. Those initial conditions are developed by the Navigation sub-system. In terms of vehicle level requirements such as orbital insertion accuracy, a well designed closed loop Guidance system will perform extremely well for a launch vehicle. Given reasonable hardware and trajectory constraints, a closed loop Guidance sub-system will drive the vehicle to the navigated vehicle target. Given reasonable performance margins, a well designed control system will maintain vehicle stability during ascent without impacting vehicle target insertion accuracy. These assumptions have been demonstrated in simulation for the Ares I and Space Launch System vehicles and will be discussed in Chapter 2. Other examples of where these assumptions hold true can be seen in United Launch Alliance's Atlas V and Delta IV and NASA's Shuttle programs. [13][1]. A well designed navigation sub-system will minimize the accumulated error and reliably provide state data as needed to the other GN&C sub-systems.

1.1 The Objective of this Thesis

This thesis focuses on the navigation sub-system, design and analysis considerations, and their impact on the other vehicle sub-systems within the context of launch vehicles. This includes the Navigation sub-system interactions with other sub-systems and the contribution of overall vehicle performance to Navigation sub-system components and design.

This thesis will:

- identify constraints and Navigation sub-system requirements from vehicle level requirements
- define a navigation system design and analysis process from a systems level approach
- define modeling and analysis techniques for launch vehicle navigation
- define navigation sub-system sensitivities and trades

NASA's Ares I vehicle and Space Launch Systems vehicles will be used as examples for context. Through examination of the examples in the context of the objectives, this thesis will supply a look into the process of taking a general top level requirement for a launch vehicle insertion orbit and decompose it into sub-system hardware specifications. Along the way, sensitivities and constraints will be identified. The resultant process and modeling and analysis techniques are presented in such a manner that they could be applied or easily modified for a similar system.

1.2 The Structure of this Thesis

This thesis consists five chapters, the first being the Introduction. The Introduction presents the basic concepts of navigation, the objective of this work, and the structure of the paper. Chapter 2 addresses the vehicle and system level approach to navigation. Within Chapter 2, types of launch vehicle navigation, vehicle level requirements decomposition, and design/analysis processes are defined and discussed. Navigation system modeling and development is described in Chapter 3. Inertial instrument technology and inertial instrument error modeling are discussed. Inertial navigation algorithms including initial alignment techniques are defined. Modeling for Global Navigation Satellite System (GNSS) error models and a Global Positioning System (GPS) aided navigation method are also developed. Chapter 4 presents typical navigation system sensitivities and analyses that are performed. System and Sub-System sensitivities are illustrated and vehicle level trade studies are defined. Finally, Chapter 5 summarizes the conclusions of this work.

CHAPTER 2

A SYSTEMS APPROACH TO NAVIGATION SYSTEMS FOR LAUNCH VEHICLES

2.1 Launch Vehicle Design Requirements

This section addresses Navigation system requirements and sizing. It has been stated that design, in general, is the work of physicists and mathematicians, with the details left to the engineers. Regardless of the statement's truth, the majority of this work is based on application with context from the following two example programs. The first of the two programs is the Ares I launch vehicle. The second programs is NASA's Space Launch Systems (SLS). Currently under design, SLS is a heritage based heavy lift launch vehicle with an extensive evolutionary path to even higher performance capability.

2.1.1 Ares I Overview

The Ares I vehicle was a part of the Constellation Program, which was NASA's primary program of record when this work began. The Constellation program was the product of NASA's Exploration Systems Architecture Study (ESAS) study released to the public in December of 2005. Until recently, NASA had been working on detailed design and development of Constellation, touted as America's next generation of launch vehicles for human space flight and manned exploration beyond our planet.

Although the focus of this work is not the Ares I vehicle or the Constellation program, it is important to briefly describe the program and the role of Ares I. Figure 2.1 graphically depicts one version of the Constellation vehicles. The fleet consisted of the Ares I crew launch vehicle and the Ares V Cargo Launch Vehicle, or Heavy Lift Vehicle. As the names suggests, Ares I was to be responsible for delivering crew to Low Earth Orbit (LEO) in the Orion Crew Exploration Vehicle (CEV) where they would rendezvous with either the International Space Station (ISS) or the Earth Departure Stage (EDS) and Altair Lunar Module (LM), formerly the Lunar Surface Access Module (LSAM). For the Constellation lunar reference mission, Altair and the EDS were to be boosted into orbit in advance of the crew by Ares V. For Ares I, there were two reference missions considered, a Lunar or Due East reference mission in which the vehicle was to launch due east to an approximate 29 degree orbit inclination to maximize up-mass, and an ISS mission with insertion into an orbit of approximately 51.5 degree inclination. For Ares I, the mission concluded at the insertion of Orion into orbit, 30 seconds post Main Engine Cut-off (MECO). The remainder of the mission, including the trans-lunar injection maneuver was the responsibility of Altair and Orion. The GN&C function, post-LEO insertion, resided in Orion.[11]

At some time after insertion, the Orion would separate and circularize its orbit while the Ares I Upper Stage fell back to the Earth. These two events defined the insertion accuracy requirements for the Ares I vehicle. The propellant reserve that the Orion had to allocate for transfer to a stable orbit was a function of the accuracy in which the capsule was inserted. It was expected that, during this initial maneuver to reach a stable orbit, Orion would compensate for any orbit error necessary. The insertion error that Orion had

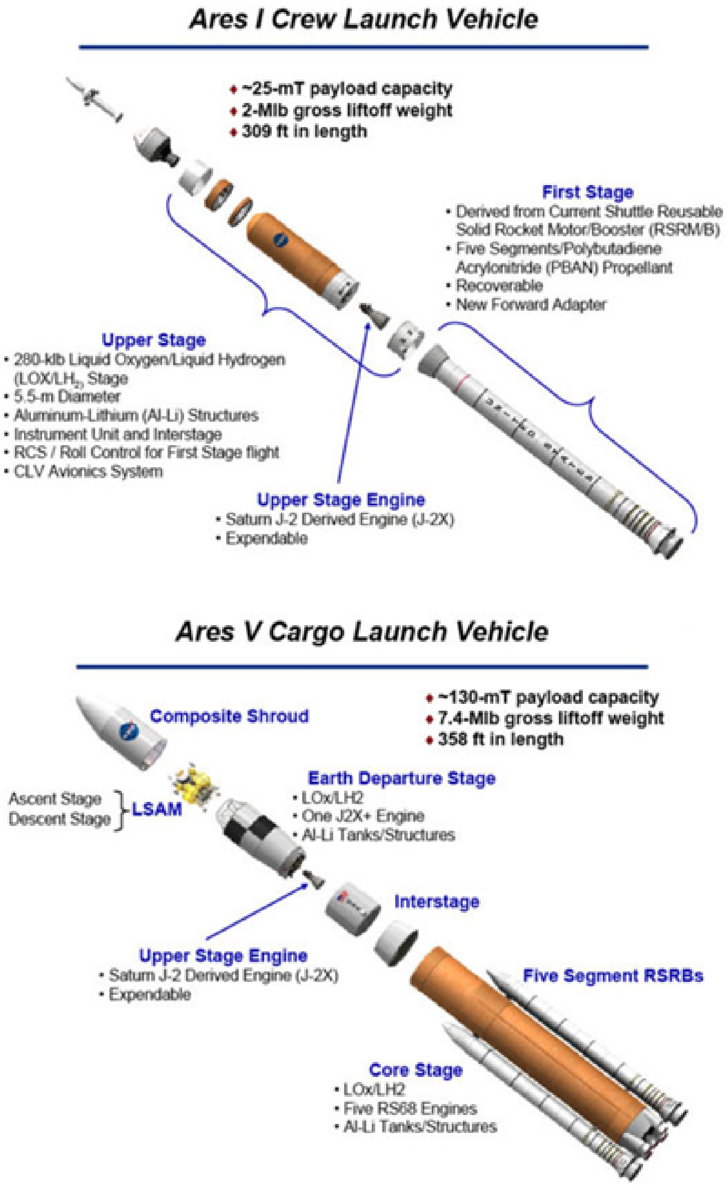
Ares I Crew Launch Vehicle
~25-mT payload capacity
2-Mlb gross liftoff weight
309 ft in length
First Stage
• Derived from Current Shuttle Reusable Solid Rocket Motor/Booster (RSRM/B)
• Five Segments/Polybutadiene Acrylonitride (PBAN) Propellant
• Recoverable
• New Forward Adapter
Upper Stage
• 280-klb Liquid Oxygen/Liquid Hydrogen (LOX/LH2) Stage
• 5.5-m Diameter
• Aluminum-Lithium (Al-Li) Structures
• Instrument Unit and Interstage
• RCS / Roll Control for First Stage flight
• CLV Avionics System
Upper Stage Engine
• Saturn J-2 Derived Engine (J-2X)
• Expendable
Ares V Cargo Launch Vehicle
Composite Shroud
~130-mT payload capacity
7.4-Mlb gross liftoff weight
358 ft in length
Ascent Stage
Descent Stage
LSAM
Earth Departure Stage
• LOx/LH2
• One J2X+ Engine
• Al-Li Tanks/Structures
Interstage
Upper Stage Engine
• Saturn J-2 Derived Engine (J-2X)
• Expendable
Five Segment RSRBs
Core Stage
• LOx/LH2
• Five RS68 Engines
• Al-Li Tanks/Structures

Figure 2.1

Ares Vehicles

to compensate for was a function of the Ares I insertion accuracy and, therefore, a function of the Ares I navigation system accuracy. Further, the spent Ares I Upper Stage would be left in an unstable orbit and would eventually re-enter the Earth's atmosphere breaking up and depositing debris into the Indian Ocean. This size of the debris footprint would be a function of the achieved insertion orbit and its relative accuracy, also directly related to the Ares I navigation system accuracy.

Although the exact mission profile evolved over time, it is essentially described in some detail in Figure 2.2. This represents Design Analysis Cycle 1, Revision 3.[65] More updated mission timelines have been designated sensitive by NASA and are not available for publication, but the general mission concept is represented well below.

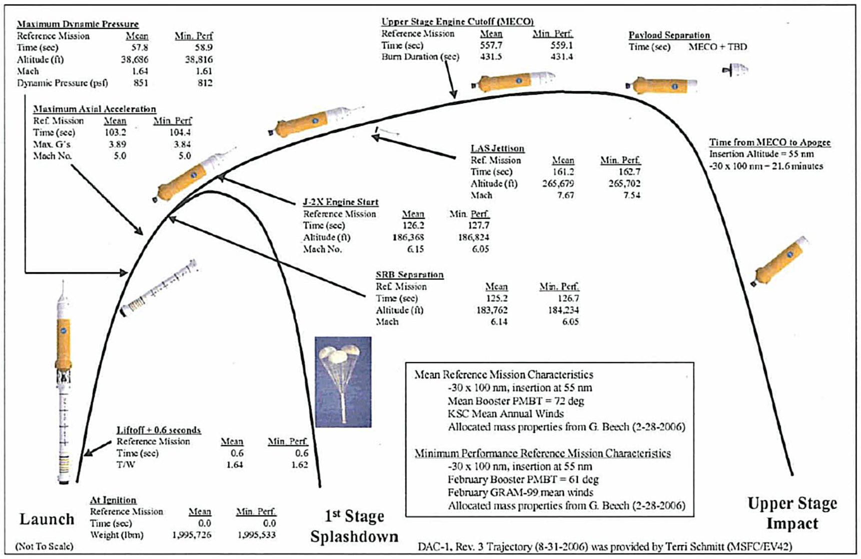
Maximum Dynamic Pressure
Reference Mission Mean Min. Perf
Time (sec) 57.8 58.9
Altitude (ft) 38,686 38,816
Mach 1.64 1.61
Dynamic Pressure (psf) 851 812
Maximum Axial Acceleration
Ref. Mission Mean Min. Perf
Time (sec) 103.2 104.4
Max. G's 3.89 3.84
Mach No. 5.0 5.0
Upper Stage Engine Cutoff (MECO)
Reference Mission Mean Min. Perf.
Time (sec) 557.7 559.1
Burn Duration (sec) 431.5 431.4
Payload Separation
Time (sec) MECO + TBD
LAS Jettison
Ref. Mission Mean Min. Perf.
Time (sec) 161.2 162.7
Altitude (ft) 265,679 265,702
Mach 7.67 7.54
Time from MECO to Apogee
Insertion Altitude = 55 nm
-30 x 100 nm – 21.6 minutes
J-2X Engine Start
Reference Mission Mean Min. Perf.
Time (sec) 126.2 127.7
Altitude (ft) 186,368 186,824
Mach No. 6.15 6.05
SRB Separation
Ref. Mission Mean Min. Perf.
Time (sec) 125.2 126.7
Altitude (ft) 183,762 184,234
Mach 6.14 6.05
Mean Reference Mission Characteristics
-30 x 100 nm, insertion at 55 nm
Mean Booster PMBT = 72 deg
KSC Mean Annual Winds
Allocated mass properties from G. Beech (2-28-2006)
Minimum Performance Reference Mission Characteristics
-30 x 100 nm, insertion at 55 nm
February Booster PMBT = 61 deg
February GRAM-99 mean winds
Allocated mass properties from G. Beech (2-28-2006)
Liftoff + 0.6 seconds
Reference Mission Mean Min. Perf.
Time (sec) 0.6 0.6
T/W 1.64 1.62
At Ignition
Reference Mission Mean Min. Perf.
Time (sec) 0.0 0.0
Weight (lbm) 1,995,726 1,995,533
Launch
(Not To Scale)
1st Stage Splashdown
Upper Stage Impact

DAC-1, Rev. 3 Trajectory (8-31-2006) was provided by Terri Schmitt (MSFC/EV42)

Figure 2.2

Ares I Mission

The Ares I GN&C system provided four primary functions; Navigation, Guidance, Steering and Control. A single Redundant Inertial Navigation Unit (RINU) in the Instrument Unit (IU), occupying the forward most section of the Upper Stage, was to be used for navigation state data and acceleration measurements for all of flight, and angular rate measurements for Upper Stage flight. Additional angular rate measurements from Rate Gyro Assemblies (RGA) in the Interstage and First Stage Aft Skirt were to be used by the Controls subsystem during first stage flight. The Interstage is located at the forward edge of the First Stage. The First Stage engine was a 5-stage Solid Rocket Motor, similar to the 4-segment Solid Rocket Boosters (SRB) used on Shuttle but with distinct differences in addition to the fifth segment. The Upper Stage engine was to be a newly developed J2X engine.

2.1.2 Space Launch Systems

In April of 2010, the President announced in a speech at Kennedy Space Center (KSC) that he intended to cancel the Constellation program. The Authorization Bill of 2010, passed by Congress, officially canceled Ares I and redirected efforts to the design and development of a new heavy lift vehicle. At Marshall Space Flight Center, effort was shifted from development of Ares I to trade studies for a heavy lift launch vehicle. SLS was born from these trade studies.

The resultant SLS Program, has a focus on affordability, a short development period, and maximum reuse of existing resources and vehicle elements. SLS is really several vehicles with an evolvable path. A preliminary rendering of the SLS vehicles are depicted

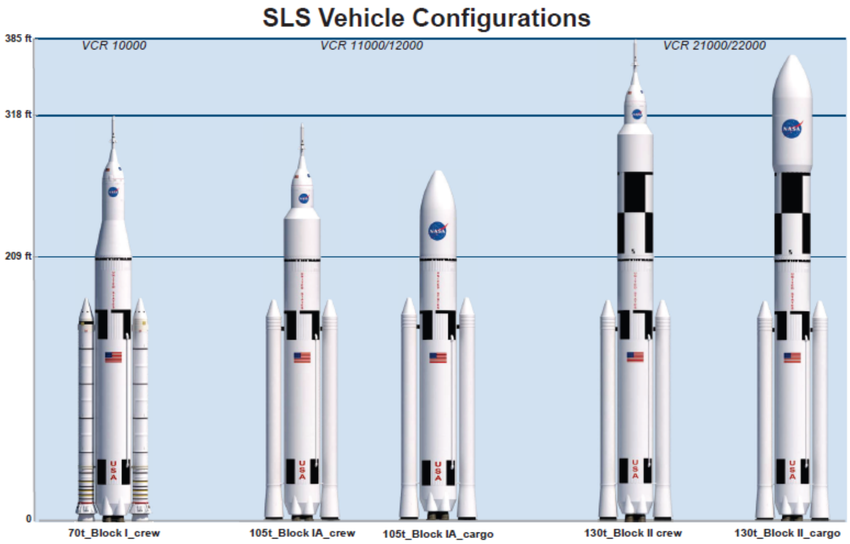
SLS Vehicle Configurations
385 ft
318 ft
209 ft
0
VCR 10000
VCR 11000/12000
VCR 21000/22000
70t_Block I_crew
105t_Block IA_crew
105t_Block IA_cargo
130t_Block II crew
130t_Block II_cargo

Figure 2.3

SLS Vehicles

in Figure 2.3 with the common Core Stage. The initial phase, or Block, consists of a vehicle derived from existing hardware. The Block 1 vehicle would fly a modified Shuttle external tank as its Core stage with actual Shuttle RS-25D engines. Solid rocket motors which were modified from 4-segment Shuttle SRBs to 5-segment Reusable Solid Rocket Motor Boosters (RSRMB) for Ares I, are attached to the Core Stage. The Core Stage Avionics are derived from the Upper Stage avionics developed for Ares I.[75]

The SLS mission extends beyond the Ares I mission in that trans-lunar injection is the responsibility of SLS. This contrasts from the predecessor program in that the trans-lunar injection was the responsibility of Orion and Altair. For the initial two missions, comprising the design reference missions for the Block 1 vehicle, a second stage will be included that is based upon a Delta IV upper stage. It is denoted the Delta Cryogenic

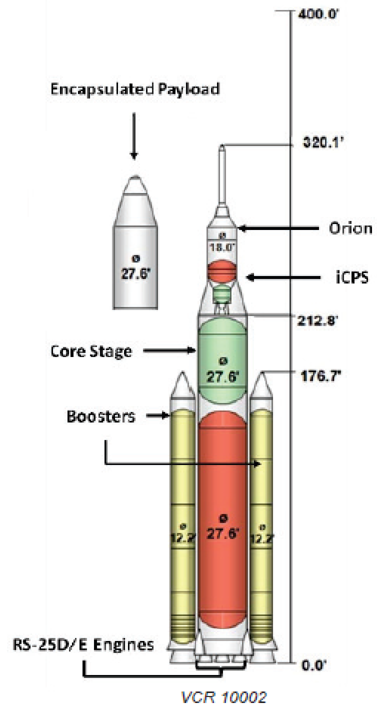
400.0'
Encapsulated Payload
320.1'
ø
27.6'
Orion
ø
18.0'
iCPS
212.8'
Core Stage
ø
27.6'
176.7'
Boosters
ø
12.2'
ø
27.6'
ø
12.2'
RS-25D/E Engines
0.0'
VCR 10002

Figure 2.4

SLS Block 1 Diagram

Second Stage (DCSS). Under the SLS program, the DCSS will be modified. The modified DCSS based SLS second stage for the Block 1 vehicle is denoted the Interim Cryogenic Propulsive Stage (ICPS), shown in early form in Figure 2.4. The successor of the SLS ICPS is the SLS Cryogenic Propulsive Stage (CPS). While ICPS is heavily based on a heritage design, CPS is to be a new NASA-designed Stage.[75]

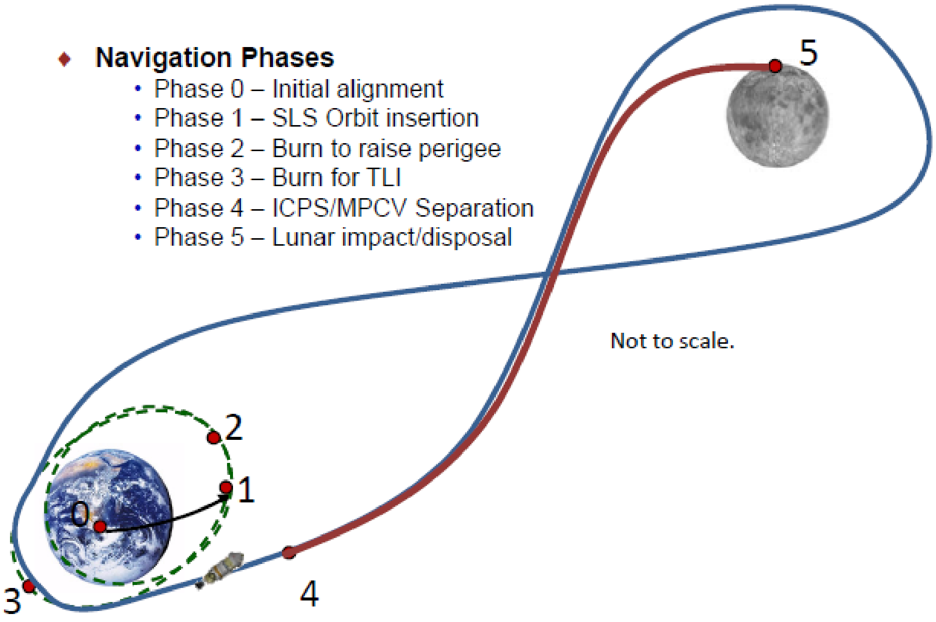
Navigation Phases
Phase 0 – Initial alignment
Phase 1 – SLS Orbit insertion
Phase 2 – Burn to raise perigee
Phase 3 – Burn for TLI
Phase 4 – ICPS/MPCV Separation
Phase 5 – Lunar impact/disposal
Not to scale.
0
1
2
3
4
5

Figure 2.5

ICPS Mission

During SLS ascent, the ICPS is to remain passive. The ICPS assumes the responsibility of the main propulsive element after the Core Stage has inserted SLS into LEO. After separation, the Core Stage will fall back to the Earth, and the ICPS will raise the low perigee of the insertion orbit to that of a sustainable orbit. After a coast period on this transfer orbit, ICPS will provide the propulsive maneuver required to put Orion onto a trans-lunar trajectory. This maneuver will likely occur around the transfer orbit apogee. The ICPS is then charged with safe self-disposal after Orion separation. In keeping with the precedents set by the Apollo program, the disposal will likely consist of a lunar impact or injection into heliocentric space. Figure 2.5 illustrates the approximated mission timeline in terms of phases.[56]

2.2 The General Design Process

Given a general set of example vehicle configurations and top level mission requirements, the question of how to design and verify a navigation system arises. At the on-set of the principal task of designing the navigation system for the Ares I vehicle, some general sub-tasks were laid out. A synopsis of this multi-step process is presented:

1. Define vehicle mission objectives and perform requirements analysis.
2. Coarsely define the operational timelines as they apply to navigation.
3. Discuss hardware availability with the hardware authority and define architecture.
4. Define required analysis platform capabilities and develop analysis software.
5. Perform navigation accuracy analysis based on mission objectives and understand error sources and system sensitivities.
6. Conduct system architecture trades.
7. Define hardware specifications and required technical deliveries.
8. Perform detailed navigation accuracy analysis based on mission objectives and hardware details.
9. Develop navigation algorithms and embedded navigation flight software.
10. Perform integration testing/lab testing.
11. Flight test for model validation.

It was accepted that this initial list would, in time, be moved around, added to, possibly de-scoped, and otherwise adjusted. The list served as a rough road map of how to proceed. An example of an Ares I task that was de-scoped is number 9. Navigation algorithms were developed but it became the responsibility of other organizations to develop and implement the embedded software based upon a System Design Document and system requirements flowed down through a component specification. After the architecture trades and Inertial Navigation System (INS) contract award, the INS vendor took over the task of writing and implementing the embedded software for inertial navigation and initial alignment. The task of developing the embedded code for the remainder of the navigation software from defined algorithms, simulation code, and design definitions fell to the Ares Upper Stage Flight Software organization. SLS has implemented a different approach from Ares in which pseudo-code, in the form of functional C-code, is developed in lieu of a traditional Design Document containing algorithms.[9] That code is then delivered to the embedded software developers for review and implementation on the target computer. This process was adopted in part from Orion and is referred to as the Model Based Design approach to Flight Software.[77] In addition to Step 9, steps 10 and 11 were eventually de-scoped in part. Ares I achieved a partial test in the flight of the Ares 1-X test vehicle on October 28, 2009. This First Stage-only flight test is used today as the basis for 6-DOF simulation validation. SLS has no official test flight scheduled, but will use the first uncrewed mission as a true validation of design.

Although the list was developed with Ares I in mind, SLS has proceeded along a similar coarse. The list could be considered general enough such that, in most cases, it can serve as a starting point for any navigation systems design. Of course, any one of these ”steps” can represent a large undertaking.

As the Ares I design process evolved additional tasks for the navigation team became necessary. These tasks included the design of an accelerometer filter for stage separation timing which supplied a smooth and accurate axial acceleration measurement in an effort to separate the stages without re-contact while optimizing for energy loss prior to Upper Stage engine ignition. Sensor redundancy algorithms were developed and implemented to produce properly down-selected and down-sampled angular rate measurement from necessarily redundant high rate measurements at the Interstage and First Stage Aft Skirt Rate Gyro Assembly (RGA) locations suitable for control systems. Pre-launch timelines for navigation and navigation sensors with check-out procedures and operations test verification requirements (TVR-O) for navigation sensors and systems were developed. Algorithms were developed to assess sensor measurement quality for use by the control system. Sensor latency budgets and subsequent requirements on vehicle avionics were defined. Also, analysis was performed for the development of alignment requirements for the Inertial Navigation System (INS) hardware and RGAs with respect to mount, vehicle, and stage. These additional items are not covered in this work; however they were each important aspects of the Ares I design and are mentioned in order to reflect the entirety of a typical launch vehicle Navigation system development. The remaining applicable steps are discussed in the sections to come, and details as to how they were accomplished for the Ares I navigation system design and SLS are included wherever possible. Chapter 3 specifically focuses on step 4 while Chapter 4 focuses on steps 5 and 6.

2.3 The General Analysis Process

At MSFC, the mainstream launch vehicle navigation analysis structure is describes by the Figure 2.6.[55] Although it may appear complicated, there is a very natural flow to the process. To start, the target accuracy for insertion is determined and a general architecture is defined in Step 1 of the design process. A general error model is estimated from an understanding of existing inertial hardware and navigation error sensitivity analysis to meet the insertion requirements. Inertial hardware sensitivities are discussed in depth in Chapter 4. General models are implemented in the primary closed loop six degree of freedom (6-DOF) vehicle simulation tool. Navigation error statistics and insertion error statistics are computed from Monte Carlo analysis of the launch vehicle using the 6-DOF vehicle simulation. The application of Monte Carlo analysis to launch vehicle design and requirements analysis is discussed in great detail by Hanson and Beard and with specific application to Ares I by Hanson and Hall.[25][26] Correlation data from the 6-DOF Monte Carlo analysis is computed and analyzed to determine the relative impact of navigation error and instrument error sources to the resultant vehicle insertion error. A navigation accuracy requirement can then be revised based upon the allocation of insertion error to other error sources. An example of this from Ares I is the Upper Stage Engine tail-off transient uncertainties which, as the design progressed, became larger than expected. The navigation accuracy was revised to allow for the larger allocation to the engine tail-off uncertainty. Revising the navigation accuracy requirement subsequently requires the instrument error budget to be subsequently revised. The Vehicle 6-DOF simulation is then re-run for a reference navigation trajectory or trajectories and to test the new instrument error budget. Something to further note about Figure 2.6 is that every leg of the process shown was exercised at least once during the course of the Ares I design process. The exterior legs required large efforts usually involving coordination and negotiation with multiple organizations.

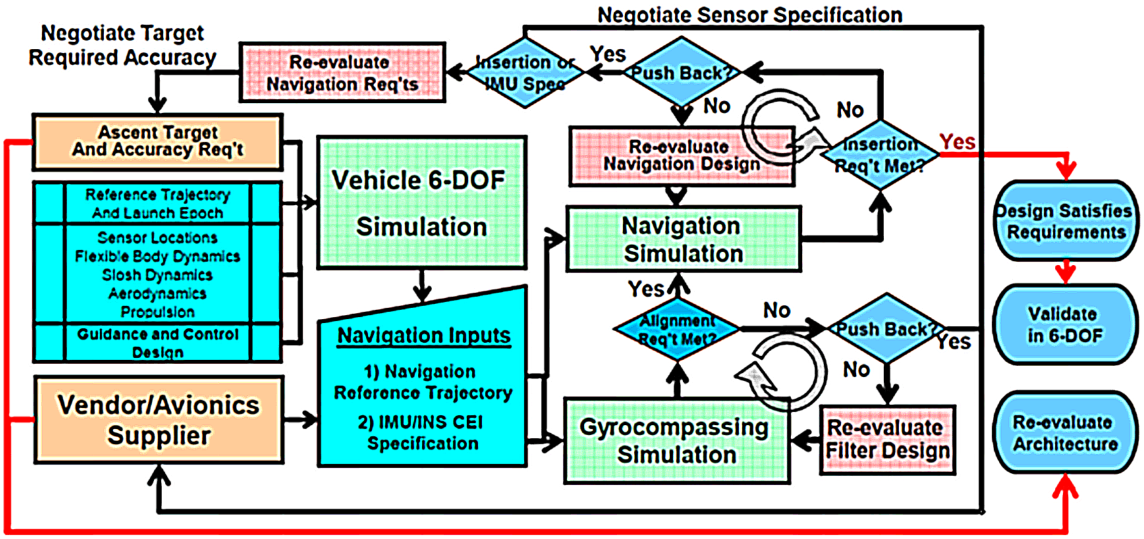
Negotiate Target Required Accuracy
Re-evaluate Navigation Req'ts
Insertion or IMU Spec
Yes
Negotiate Sensor Specification
Push Back?
No
No
Re-evaluate Navigation Design
Insertion Req't Met?
Yes
Ascent Target And Accuracy Req't
Reference Trajectory And Launch Epoch
Sensor Locations
Flexible Body Dynamics
Slosh Dynamics
Aerodynamics
Propulsion
Guidance and Control Design
Vehicle 6-DOF Simulation
Navigation Simulation
Design Satisfies Requirements
Validate in 6-DOF
Yes
Alignment Req't Met?
No
Push Back?
Yes
No
Navigation Inputs
1) Navigation Reference Trajectory
2) IMU/INS CEI Specification
Vendor/Avionics Supplier
Gyrocompassing Simulation
Re-evaluate Filter Design
Re-evaluate Architecture

Figure 2.6

Navigation Design and Analysis Cycle

For both Ares I and SLS, the primary 6-DOF simulation software used was/is the Marshall Aerospace Vehicle Representation in C (MAVERIC).[42] MAVERIC is a variable-fidelity vehicle simulation capable of dynamics in both three and six degrees of freedom. It is capable of simulating multiple stages, multiple vehicles, and complex discrete and pseudo-continuous models. It allows for the simulation of trajectory dependent and independent vehicle dynamics resulting from mass interaction, aerodynamics, propulsive elements, propellant slosh, and other flight physics. It is also capable of simulating flight timelines, discrete events, and the interactions of flight software such as guidance, navigation, and control systems with detailed sensor and effector models. This time domain simulation handled the bulk of the vehicle performance analysis for Ares I, was previously used for Ares 1-X, X-33, and Shuttle and is currently used for SLS. This simulation was validated successfully against Ares 1-X test flight data. Models such as the inertial instrument error models and navigation algorithms presented in Chapter 3, were implemented in MAVERIC. The use of this simulation represents the beginning of the analysis cycle, in Figure 2.6, by the definition of the navigation reference trajectory and also the end of the cycle with the validation of the navigation error budget and architecture against the navigation system requirements.

The primary navigation-specific tool used at the onset of the Ares I work was the Strapdown Navigation Analysis Program (SNAP) developed by NASA MSFC and Control Dynamics.[84] Due to specific limitations associated with this tool, a new development was commissioned. The new tool came to be known as the Navigation Error Analysis Tool (NEAT) and was developed continuously as the Ares I design progressed and has continued in development through SLS.[59] There currently are five variants of NEAT: NEAT, NEAT cpp, NEAT Lite, NEAT SF, NEAT Truth, and NEAT v2. NEAT consists of an instrument error model, inertial navigation software, and statistical analysis capabilities. When gyrocompassing software was added to NEAT, the version without gyrocompassing became NEAT Lite. Gyrocompassing is one method of estimating the initial attitude for an inertial navigation system. The gyrocompassing software includes both deterministic coarse alignment algorithms and fine alignment algorithms for gyrocompassing. Versions of NEAT include both Monte Carlo and covariance analysis capabilities for statistical analysis. The models included in NEAT and the analysis methodologies used are discussed in depth in Chapter 3. The figure below depicts the top level block of the Matlab Simulink variant of NEAT. NEAT cpp was the redesign of NEAT programmed in C due to computational inefficiencies associated with the use of Matlab Simulink in Monte Carlo analysis and subsequent delay in turning out results. NEAT v.2 is an offspring of NEAT cpp used for SLS analysis which includes an expanded error model, a slightly different filter and algorithm set, a low fidelity GPS model, and additional post-processing capabilities. NEAT was originally developed under NASA contract by Dynamic Concepts, Inc by a small engineering team of two, including this author. NEAT development continued after the contract by this author. All variants of NEAT are referred to as NEAT and are representative of the same basic core.

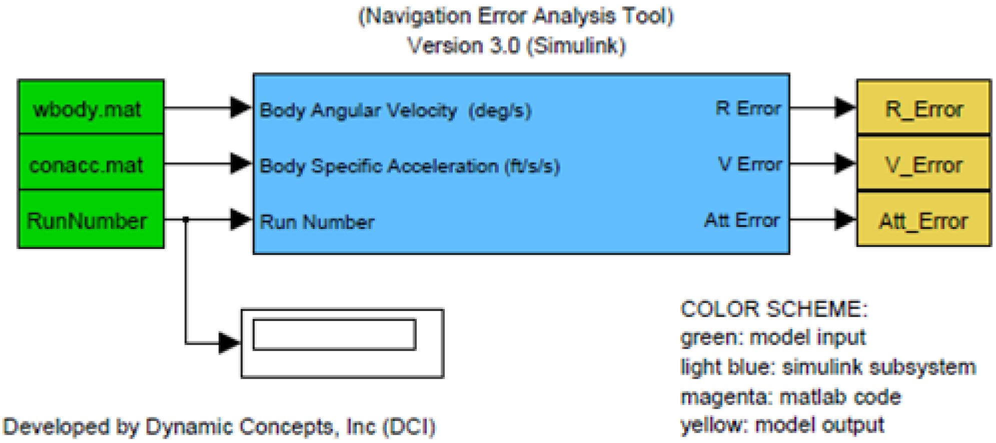
(Navigation Error Analysis Tool)
Version 3.0 (Simulink)
wbody.mat
conacc.mat
RunNumber
Body Angular Velocity (deg/s)
Body Specific Acceleration (ft/s/s)
Run Number
R Error
V Error
Att Error
R_Error
V_Error
Att_Error
COLOR SCHEME:
green: model input
light blue: simulink subsystem
magenta: matlab code
yellow: model output
Developed by Dynamic Concepts, Inc (DCI)

Figure 2.7

NEAT: Top Level

Given that the dispersed trajectory does not vary greatly from the defined navigation reference trajectory spatially and in duration, the navigation analysis tool can exist separate from the closed loop simulation. This is due to a lesser dependence in navigation error on many of the non-instrument error sources and dispersions implemented in the closed loop vehicle simulation. Otherwise stated, the correlation of navigation error to non-instrument error vehicle dispersions is low in comparison to instrument errors correlations. This fact is supported by the correlation data discussed in Section later in this Chapter. Navigation accuracy requirements are refined based on full closed-loop 6-DOF correlation data and the development of an enveloping reference case is dependent on the models implemented in the closed loop 6-DOF simulation, but instrument error budget development and refinement can be done open-loop.

SLS required the use of more specialized tools due to the inclusion of the ICPS into the mission architecture. Copernicus was used to generate optimized 3-DOF LEO and lunar trajectories to model the post-insertion portion of the SLS mission. Copernicus is a generalized spacecraft trajectory design and optimization tool.[85] By the very nature of 3-DOF trajectory generation, it is not uncommon for a 3-DOF trajectory to not include angular rates or vehicle attitude. If attitude angles are supplied, they are often respective of the guidance command or vehicle velocity vector and are not suitable for navigation analysis due to the absence of the attitude differential equation in the equation of motion for the simulation that generated the trajectory. To expedite the navigation analysis, a capability was added to the NEAT suite to generate a 6-DOF trajectory with real attitude and angular rates from 3-DOF trajectories with a limited capability to simulated attitude maneuvering. Additionally, tools were developed to compute the change in velocity required by the spacecraft to correct for navigation error at the initiation of the TLI maneuver. To maximize effectiveness and assure validity, capabilities were incrementally built upon previously developed and tested capabilities. The techniques and methods associated with the tools used are discussed further in Chapter 3.

2.4 System Sensitivities and Design Considerations

This section deals with requirements analysis and constraint identification cited in the design process. Only after the problem has been sufficiently defined can tools be developed and analysis performed for the system design. It is critical to fully understand the constraints on the governing requirements when defining them. This is an effort that can easily be omitted in lieu of acting according to precedent or doing what is convenient. An example of this was seen in the definition of the out-of-plane error created early in Ares I development. The requirement was defined based on Shuttle precedent without consideration for the differences in the vehicles, both in architecture and mission. There were differences in mission and navigation architectures between the vehicles that were not considered, e.g. Shuttle was an on-orbit vehicle while the Ares I mission ended at insertion and Shuttle flew a gimballed platform while Ares I was slated to fly a strapdown INS. This resulted in the development of an insertion orbit plane error requirement that dictated an inertial instrument quality that could not be met by the organization responsible for the specification and procurement of avionics hardware. Another example where precedent was accepted without proper assessment was seen in the initial development of the accuracy requirements set for ICPS for SLS. The initial requirement was based upon a survey of commercial Evolved Expendable Launch Vehicle (EELV) capability. Requirements for different types of missions were mixed with respect to required accuracy, parameterized as orbital elements. This resulted in an inconsistent requirements specification. A dispersion on semi-major axis, for example, for LEO cannot be directly compared to a dispersion on semi-major axis for a Geostationary Transfer Orbit (GTO) without considering the sensitivity of the inherent errors in position and velocity to this orbital parameter. Not only does this type of constraint violate the intention of the accuracy requirement, but for an unaided inertial navigation system, using the principals of dead reckoning, it can create a requirement set which is impossible to meet from either a physical or cost perspective. A similar mistake was quickly corrected for SLS when the target orbit was changed from a slightly eccentric orbit to a substantially eccentric orbit. The intention was not to impact the accuracy required of the navigation system, but by changing the target orbit, the parameterization of the insertion accuracy into orbital elements meant something very different in terms of the inherent position and velocity errors despite having the same insertion altitude. These few examples depict how important it is to understand the design space in terms of driving elements and sensitivities in terms of quantity and parameterization prior to vehicle sizing and requirements development. Launch vehicle specific design drivers and examples are presented in the following sections.

2.4.1 Sizing and Constraints Analysis

As discussed, the launch vehicle navigation system design begins with the governing vehicle level requirements, e.g. deliver some amount of payload mass into some defined orbit. This section details the general constraints for launch vehicle insertion performance with examples from Ares I and SLS. The constraints analysis begins with the assumption that a general launch vehicle configuration has been developed, missions have been defined, and trajectories have been developed. After the general paper development, the trade becomes: how well *must the mission objectives be met versus how well* can the mission objectives be met. Of course, the focus in this work is on the navigation system and the decomposition of the requirements that apply to navigation system performance.

The design and analysis cycle, Figure 2.6, indicates that the top level requirement must be negotiated and allows for re-negotiation. Properly defining the trade space requires a fundamental understanding of the primary drivers and sensitivities for the vehicle insertion accuracy requirement. A simplistic look at a typical launch vehicle mission timeline shows that the vehicle begins on the launch pad, inserts a payload into orbit, and falls back to the Earth. For sizing the launch vehicle navigation accuracy, the approach begins with assessing the insertion into orbit. How accurately the launch vehicle must insert into orbit obviously depends upon the requirements of the post-insertion payload/spacecraft mission. A slightly less obvious constraint is found in the descent phase, where the spent launch vehicle falls back to the surface of the Earth. A civilized nation would not want to drop a hot and used rocket stage into a populated area; therefore the impact footprint must be considered and constrained.

2.4.1.1 Re-Entry Footprint on Insertion Accuracy

NASA-STD 8719.14 states that a launch vehicle must not fall on populated landmass. The standard goes further to state that the debris impact footprint must be constrained such that is does not violate a 200 nautical mile keep-out zone around non-sovereign land, or territory not under the United States government.[48] This is a major constraint on target orbit and insertion altitude for trajectory design.

Figure 2.8 depicts an example analysis product from trajectory design. The impact footprints depicted are specific to the Ares I Upper Stage re-entry. Note that the depicted result was not representative of the Ares I Upper Stage impact footprint at the end of the program. In the figure, impact footprints for 3 target orbits are depicted. For a target orbit with apogee of 110nm and perigee of -20nm, the debris field impacts Western Australia and must be avoided. Being that these footprints are from trajectory analysis, they represent ballistic impact based upon 3-DOF analysis with a small set of dispersion in the vehicle configurations. They do not include errors specific to guidance or navigation.

Other than orbital debris footprint, the payload objectives must be considered for sizing of the orbit accuracy. In the case of Ares I, the intended payload was the Orion Crew Exploration Vehicle, sometimes referred to as the Mult-Purpose Crew Vehicle. Hanson identified three major impacts of the launch vehicle, Ares I, on Orion.[24]

1. A low apogee altitude could result in thermal issues related to atmospheric drag as well as a issues related to phasing for orbit rendezvous for Orion.
2. Orion must make up shortfalls associated with an off-nominal insertion requiring the expenditure of propellant to correct for a low energy orbit or error in the intended orbit plane.
3. Insertion orbit variations can cause timing changes for subsequent rendezvous.

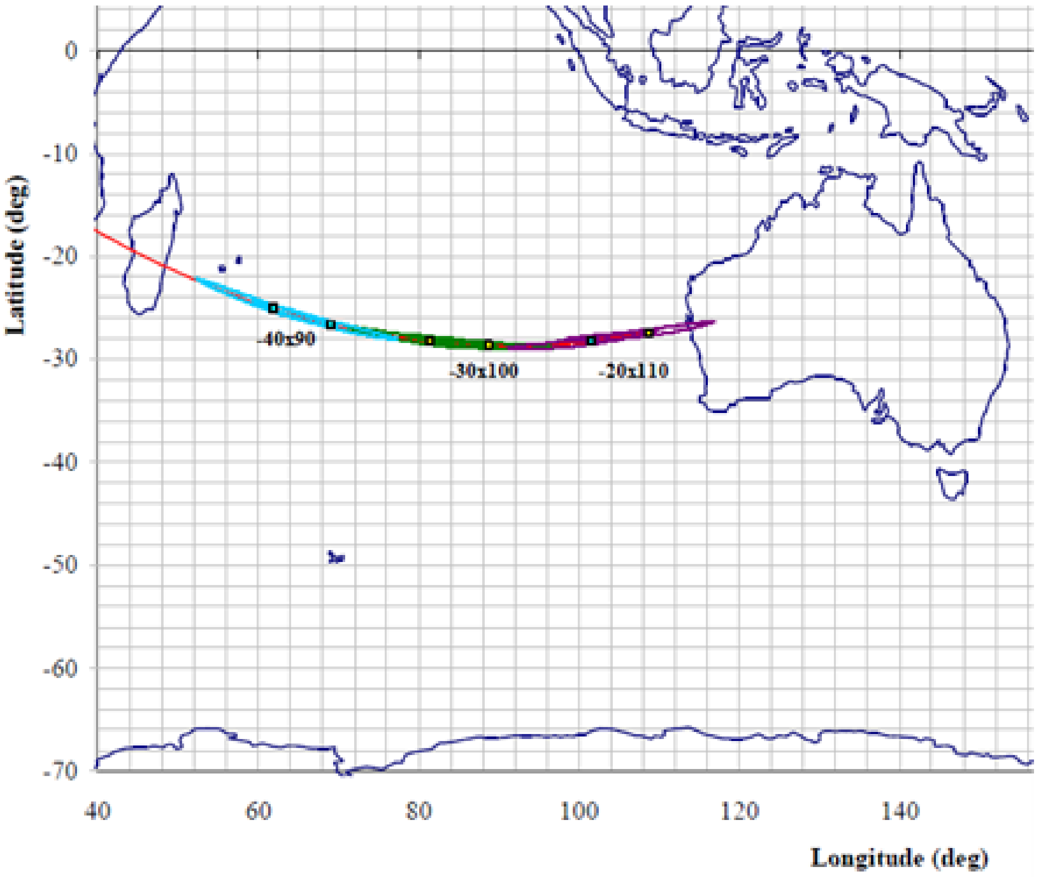
0
-10
-20
-30
-40
-50
-60
-70
Latitude (deg)
40
60
80
100
120
140
Longitude (deg)
-40x90
-30x100
-20x110

Figure 2.8

Ares I Debris Footprint Example from Trajectory Analysis

Item 3 was dismissed since its impact could be negated through on-orbit re-optimization of rendezvous maneuver. Item 2 constrains nominal trajectory design and target orbit. As a result of negotiations with Orion, the nominal apogee altitude for insertion of 55 nautical miles was increased at the request of the Orion design team due to thermal issues. The trajectory was re-designed from the example in Figure 2.8 above and re-optimized to place the nominal impact point in the middle of the Indian Ocean while maximizing orbital energy. The trajectory design team converged on a target orbit with a lower nominal perigee but higher apogee.

2.4.1.2 Insertion Accuracy on Impact Footprint

To assess sensitivities given the complicated non-linear dynamics associated with ascent and re-entry characteristic, vehicle sub-system models were developed for simulation in MAVERIC by the development team. The author of this paper was responsible for the navigation and sensor models, the analysis of the navigation and sensor model output, and the analysis of the impact to the vehicle, sub-systems, and insertion accuracy by the navigation system. In accomplishing this, best estimates for dispersions were put on model input parameters. The simulation was run for Monte Carlo analysis in which the inputs are dispersed according to defined distributions. Correlations were computed on the output. The correlations matrix was computed based upon an observation matrix. The observation matrix consists of the simulation output parameters over the set of dispersions where each row represents the result from a different set of randomly dispersed input. Equation (2.1) gives the sample covariance, from which the correlation matrix is computed, Equation (2.2).

The over bars indicate the mean value for the respective variable or column over the sample distribution. A non-zero correlation indicates a likelihood that the output parameter is a function of the input variable. A high correlation may indicate a strong dependance.

$$X = \begin{vmatrix} x_{1,1} & x_{1,2} & \dots & x_{1,m} \\ \vdots & \vdots & \vdots & \vdots \\ x_{n,1} & x_{n,2} & \dots & x_{n,m} \end{vmatrix}$$

$$Cov(X)_{j,k} = \frac{1}{n-1} \sum_{i=1}^{n} \left(x_{i,j} - \overline{x}_j\right) \left(x_{i,k} - \overline{x}_k\right) \tag{2.1}$$

$$Cor(X)_{i,j} = \frac{Cov(X)_{i,j}}{\sqrt{Cov(X)_{i,i} Cov(X)_{j,j}}} \tag{2.2}$$

MAVERIC output was used to show strong correlation of in-plane orbit insertion error expressed in semi-major axis to the distance spanned by the Ares I US impact footprint dispersion. MAVERIC output also showed a high correlation between in-plane orbit insertion error, (i.e. semi-major axis and radius of apogee), to navigation error at insertion and to the uncertainty in the engine tail-off transient. The engine tail-off represents the residual thrust generated by the vehicle after the engine has been commanded to shutdown by the guidance function. The uncertainty in that parameter represents the portion of the tail-off thrust which cannot be predicted and therefore cannot be compensated for in adjusting the shutdown trigger during flight.

For SLS, this process was repeated, with Ares I based data, to develop an understanding of the design space and basic sensitivities in order to size the new vehicle. Figure 2.9

depicts a result of this analysis in which the Ares I vehicles and models where used to develop a simplistic model for the effect of in-plane error on impact footprint for target accuracy sizing.

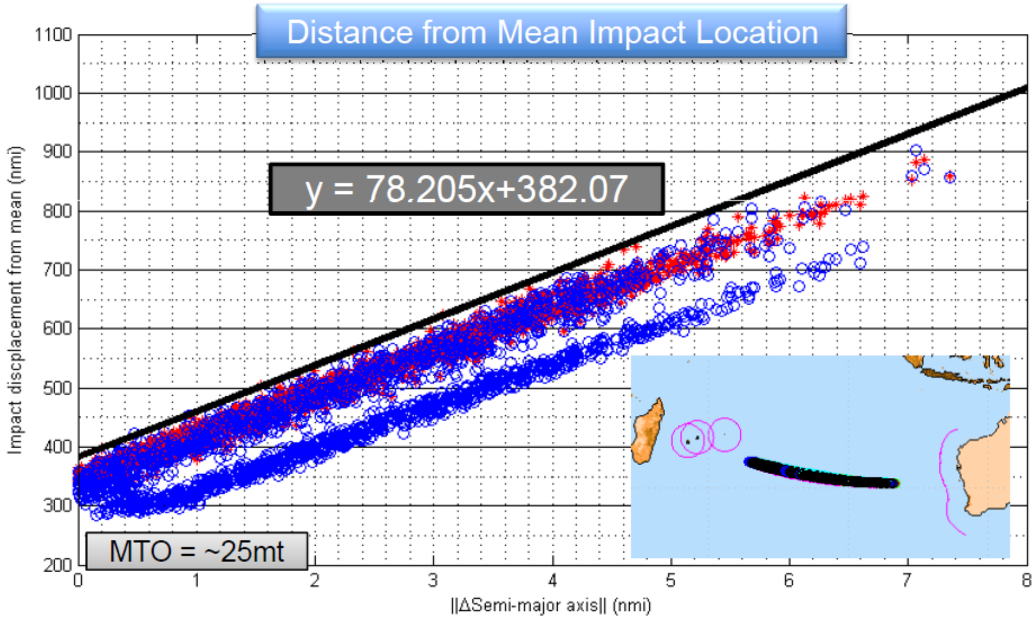

Figure 2.9

In-plane Error Vs. Footprint for -47x130nmi target

In the trajectory design process, the insertion altitude and target orbit can be traded for impact point, but the distance between land masses is fixed. The object, with regard to sizing, is to control the uncertainty in the impact footprint. In Figure 2.9, the in-plane error, parametrized by delta semi-major axis, was compared against impact displacement from the mean impact point. The two nearest land masses spanning the Indian Ocean were found to be the western most point on the Australian coast eastward and Rodriguez

Island to the west. A distance of 2745 nautical miles was computed along the geodesic between the two points. Considering the keep out zones and applying the model developed in Figure 2.9, a constraint of 12.6 nautical miles was developed for the semi-major axis error for the particular target orbit.[62]

An initial target orbit of -47 nautical miles in perigee altitude and 130 nautical miles in apogee altitude was considered for the footprint constraint analysis. Repeating the analysis for a different target orbit showed that the relationship between the in-plane vehicle insertion error and the footprint displacement remained approximately linear but the slope changed significantly with the orbit and could not be ignored in subsequent analysis.[16][58] The relationship was found to be a function of orbit shape. A lower perigee corresponded to a steeper re-entry and smaller footprint. The particular model may not have been applicable to subsequent target orbits, but the process for developing the model and the general acknowledgment of debris footprint as a constraint for accuracy sizing applies.

2.4.1.3 Insertion Accuracy on Payload

For a proper discussion on launch vehicle insertion accuracy, the concept needs to be broken into its natural components. Insertion accuracy is the measure of how well the vehicle hits its target orbit. It can be broken into in-plane error, or error within the orbit plane, and out-of-plane error. The parameterization of the insertion error in this way has distinct advantages in terms of understanding the impacts of the insertion error and on how the error is developed. Both in-plane and out-of-plane error are a function of position and velocity errors. In orbital elements, the in-plane error consists of errors in semi-major axis, radius of apogee, and radius of perigee. From the relationship in Equation (2.3), any two of the three implies a solution for the other.

$$a = \left(\frac{2}{\vec{r}} - \frac{\vec{v}^2}{\mu}\right)^{-1} = \frac{1}{2}(r_p + r_a) \tag{2.3}$$

The in-plane insertion error mostly manifests late in flight and is very sensitive to timing of engine shutdown. Under shooting or over shooting the target in time during powered flight causes significant error with regard to in-plane orbit insertion error. This concept can be demonstrated by orbital mechanics. During powered flight the vehicle will continually increase velocity. The radius vector will increase in magnitude. The specific angular momentum will increase in turn, and the proportion of thrust directed out-of-plane required to change the plane of the orbit will increase disproportional to the thrust required to change the in-plane orbit parameters.

The out-of-plane error can be parameterized into classical orbital elements as inclination and right ascension of the ascending node, although it is sometimes more convenient to lump them into one parameter representing the whole error, denoted as wedge angle. The wedge angle represents the orbit plane targeted by guidance and the error in the achieved orbit plane that must me corrected on-orbit. The wedge angle, depicted by Figure 2.10, can be quantified as the angular difference in the specific angular momentum vectors of the target orbit and the achieved orbit.

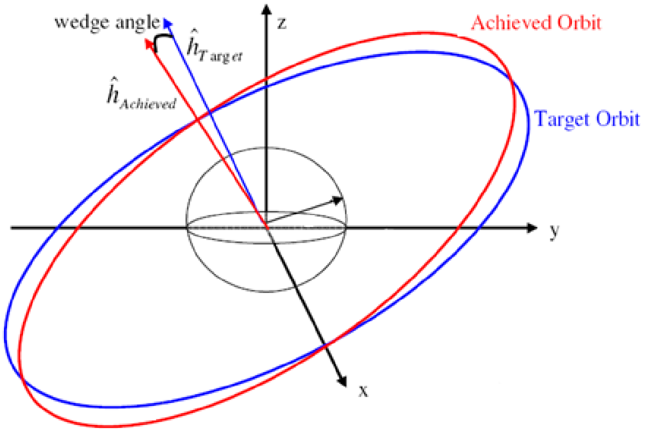

Figure 2.10

Simple Wedge Angle Diagram

The wedge angle can be described by specific angular momentum, Equation (2.4), or in terms of orbit inclination and right ascension of the ascending node by Equation (2.5). In Equation (2.4), the unit vectors $\hat{i}$,$\hat{j}$, and $\hat{k}$ are the ECI coordinate axes.

$$\vec{h} = \vec{r} \times \vec{v} = \sin i \sin \Omega \hat{\mathbf{i}} + (-\sin i \cos \Omega)\hat{\mathbf{j}} + \cos i \hat{\mathbf{k}} \tag{2.4}$$

$$wedge = \arccos\left(\frac{\vec{h}_{target} \cdot \vec{h}_{achieved}}{\|\vec{h}_{target}\|\|\vec{h}_{achieved}\|}\right) \tag{2.5}$$

$$\cos\left(wedge\right) = \frac{\hat{h}\left(\hat{h} + \delta\hat{h}\right)}{\left\|\hat{h}\right\|\left\|\hat{h} + \delta\hat{h}\right\|} = \cos\delta\Omega\cos\delta i + \left(1 - \cos\delta\Omega\right)\cos i\cos\left(i + \delta i\right) \tag{2.6}$$

Figure 2.11 depicts the parameterization of inclination and right ascension of the ascending node from wedge angle. The relationship in Equation (2.6) and the parameterization in Figure 2.11 demonstrate that the orbital element components cannot be treated as having equal weight. This is of particular importance when attempting to compare accuracies stated by EELV launch providers due to the common parameterization of out-of-plane insertion accuracy in terms of inclination and right ascension of the ascending node [13][1].

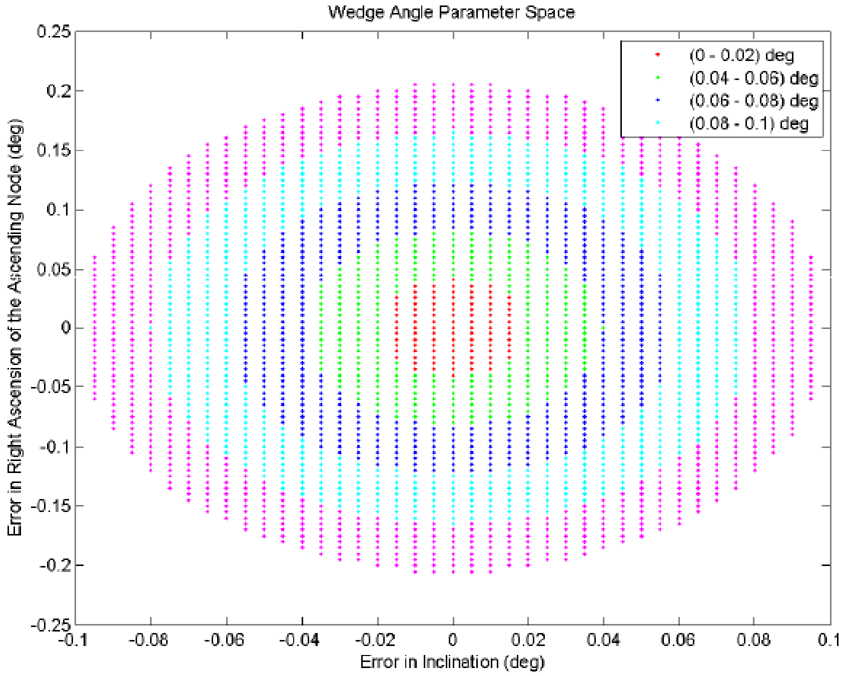

Figure 2.11

Wedge Angle Parametrization

The concepts of in-plane and out-of-plane error can be applied to item number two in Hanson's list. The shortfalls in ascent performance due to insertion error can be computed in terms of delta-velocity without consideration of spacecraft mass or engine. Equation (2.7) is the relationship for the delta-velocity required to correct for in-plane orbit insertion error. Equation (2.8) is the relationship for out-plane-error corrections.

$$\Delta v_1 = \sqrt{\mu(\frac{2}{r_a} - \frac{1}{a})} - \sqrt{\mu(\frac{2}{r_a + \delta r_a} - \frac{1}{a + \delta a})} \tag{2.7}$$

$$\Delta v_2 = 2\sqrt{\mu(\frac{2}{r_a} - \frac{1}{a})} \sin\frac{wedge}{2} \tag{2.8}$$

Given a nominal insertion target orbit with perigee altitude of -11 nautical miles and apogee altitude of 100 nautical miles, Equation (2.7) was used to produce the surface plot in Figure 2.12. The analysis assumed an arbitrary circularization maneuver to a 100x100 nautical mile orbit after separation during which the in-plane insertion error would be corrected.

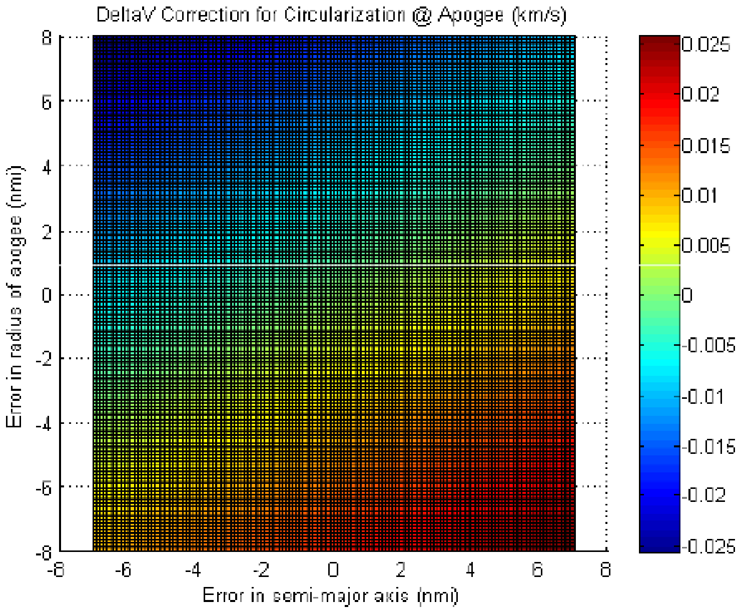

Figure 2.12

Delta-V Parametrization for -11x100nmi Insertion Error

Tsiolkovsky's rocket equation can then be used to estimate the propellant mass available for the orbit correction. Figure 2.13 depicts a surface plot which approximates the mass expenditures, as a function of mass fraction, required to correct for the error at insertion over a range of engine efficiencies. Using this approach, a propellant mass allocation for insertion error from the payload can be mapped back to an in-plane insertion accuracy requirement for the ascent vehicle and specific target orbit.

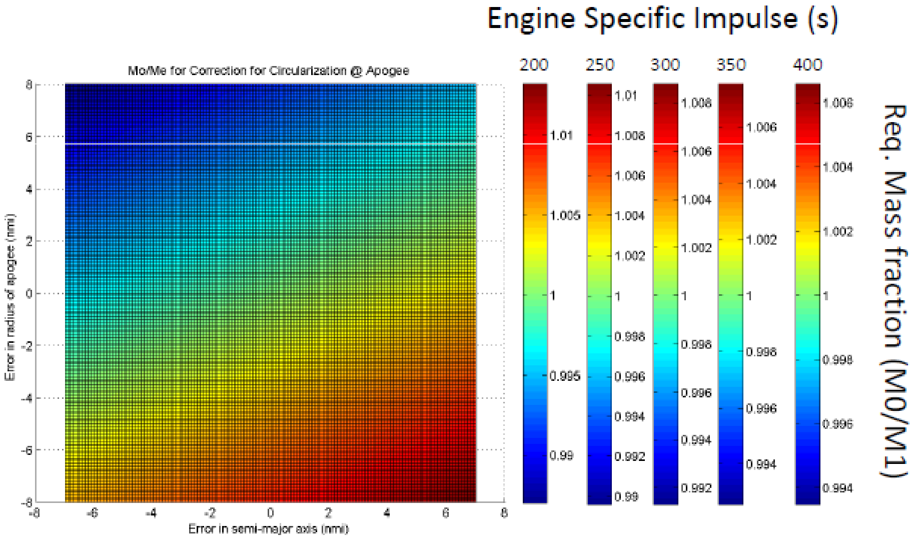

Figure 2.13

Mass Fraction Parametrization for -11x100nmi Insertion Error

A similar plot can be developed for the out-of-plane delta velocity. In order to develop a proper constraint on the insertion accuracy based upon the propellant mass allocated for correction, the variance of the combined delta velocity would need to be computed. Equation (2.9) depicts this relationship. The left side of the equation would be chosen based upon the negotiated propellant allocation. The right side of the equation would have to be evaluated. The relationship is difficult to solve analytically for a number of reasons. Equation (2.8) is non-linear and $wedge$ is not Gaussian. Equation (2.7) is also non-linear and a function of two correlated variables. Numerically determined, the statistical contribution to Δv_{total} from Δv_2 was shown to be much less significant than that of Δv_1. [62]

$$Var\left[\Delta v_{total}(M0/M1)\right] = Var\left[\Delta v_1(a, r_a)\right] + Var\left[\Delta v_2(wedge)\right] \tag{2.9}$$

For both Ares I and SLS a decision was initially made, external to the analysis, to constrain the out-of-plane orbit insertion error such that ΔV_2 did not exceed that of ΔV_1. Conservatism was applied in the form of design margin, based upon engineering judgment, to accommodate the statistical combination of Δv_1 and Δv_2. If a problem arose, then it was to be handled in the requirements iteration leg of the analysis and design cycle.

2.4.1.4 Decomposition of Vehicle Insertion Accuracy

Once defined, the vehicle insertion accuracy can be allocated out to the contributing components. To accomplish this properly, the contributing components must be identified. The 6-DOF simulation Monte Carlo results offer insight into this.

Table 2.1 contains the statistics from a set of Monte Carlo runs in the 6-DOF simulation for a particular Ares I vehicle configuration. The table contains error statistics in osculating orbital elements at payload separation for the insertion target. The elements chosen comprise the in-plane and out-of-plane components of the insertion error. Each element is represented by two entries. The first is the error computed based upon the achieved state versus the target state. The second is computed from the achieved state versus the

Table 2.1

Ares I Insertion Accuracy and Navigation Accuracy

Parameter	99.73% Low (nmi)	99.73% High (nmi)
Error in Perigee	-10.61	9.93
Error in Perigee from Nav State	-8.94	8.97
Error in Apogee	-5.10	6.44
Error in Apogee from Nav State	-3.72	4.56
Error in Semi-Major Axis	-7.75	8.22
Error in Semi-Major Axis from Nav State	-6.34	6.74
Wedge Angle	0.001	0.058
Wedge Angle from Nav State	0.0001	0.0061

reported navigation state. The computed statistics is a 99.73 percentile used to approximate a 3σ result assuming an approximate Gaussian distribution. Given that the vehicle model is dispersed in terms of standard deviations based upon the best estimate of statistical variations in the associated vehicle model uncertainties, it is common to look at the output in terms of the same type of parameters. The physical meaning of the 99.73 percentile, ignoring sampling error and incorrectly captured uncertainties, is that there is a 99.73 percent probability that that vehicle will meet mission for all vehicle possibilities and flight day conditions. Often the results are handicapped by a specific consumer risk or confidence interval. The consumer risk quotient is applied to the results to account for sampling error and incorrectly captured uncertainties. If, on flight day, a number of the epistemic uncertainties are measured to differ from the mean, a decision could be made to swap out components or launch under different conditions. The application of statistics to the vehicle model and Monte Carlo analysis to vehicle performance assessment is explored in great detail by Hanson and Beard.[26] For the insertion error parameters in Table 2.1, the

99.73 high and low percentiles are given indicative of the positive and negative tails of the probability distribution for the respective errors. The table gives insight into how much of the variation at insertion can be attributed to navigation error and how much is attributable to other sources. The navigation engineer will call the non-navigation error guidance error because the error computed from the navigation state is representative of the error known to the Guidance system. Assuming a normal distribution based upon the approximate 3σ statistics, the proportion of the error due to non-navigation related error sources can be computed from the assumed variances. For a specific Ares I vehicle configuration, these ratios are given in Table 2.2.

Table 2.2

Approximate Ares I Insertion Accuracy Non-Navigation Allocation

Parameter	Var(Nav)/Var(Total)	sqrt(Var(Nav)/Var(Total))
Error in Perigee	0.76	0.87
Error in Apogee	0.51	0.72
Error in SMA	0.67	0.82
Wedge Angle	0.01	0.11

Table 2.2, provides the ratios for σ^2 and σ for the in-plane error parameters, perigee altitude, apogee altitude, and semi-major axis, and the out-of-plane error parameter, wedge angle. The naming is counter-intuitive since Nav indicates the error computed from the navigation state and is indicative of the non-navigation error. From the data in the table, the error at insertion due to simulated Navigation system can be approximated to 24% in perigee, 49% in apogee, 33% in semi-major axis, and 99% out-of-plane in terms of

the approximated statistical variances in the error parameters. Similar ratios were used to allocate navigation accuracy requirements from vehicle insertion accuracy requirements. There is one major caveat to this process, it is important to understand that these ratios are specific to the models used and require good estimates of error sources for the primary errors.

To better understand the insertion error in terms of the contributing error sources, correlation data from a Monte Carlo run set can be examined. Table 2.3 shows the major in-plane and out-of-plane insertion error contributors. The data in the table shows that the in-plane error is primarily driven by the ability to shutdown the Upper Stage engine at the correct time, more specifically, by the tail-off transient uncertainty. The accelerometer scale factor error in the vehicle axial direction is a secondary driver. This re-enforces the Monte Carlo statistics from 2.1. The out-of-plane error is driven almost entirely by the initial attitude error, or more specifically, the initial attitude error in azimuth.

The correlations indicate that a sensor error is a contributor to the in-plane insertion error, but for this particular Monte Carlo results set they do not correctly represent the correlations between the sensor errors and the initial attitude for the vehicle. Ares I was to navigate with inertial measurements without aiding, and the initial alignment was to be estimated through gyrocompassing. Gyrocompassing is the process by which the initial attitude is estimated based only on the navigation sensor measurements prior to launch, implying that the initial attitude and the sensor errors will show strong correlation. At the time that these results were produced, the vehicle initial attitude solution was initialized from random draws. This type of initialization assumes the navigation sensor errors and

Table 2.3

Ares I Insertion Error, Top Correlated Dispersions

Apogee Altitude	
US Engine Shutdown Burn Time	0.8
INU Accelerometer Scale Factor, Axial	-0.54
US Engine Tailoff Trigger	-0.18
INU Accelerometer Bias	-0.12

Semi-major Axis	
US Engine Shutdown Burn Time	0.88
INU Accelerometer Scale Factor, Axial	-0.36
US Engine Tailoff Trigger	-0.20

Perigee Altitude	
US Engine Shutdown Burn Time	0.78
INU Accelerometer Scale Factor, Axial	-0.25
INU Initial Attitude Error, Level	-0.17

Wedge Angle	
INU Initial Attitude Error, Azimuth	0.24

the initial attitude are independent which would not be the case if the initial attitude was derived solely from the inertial instruments. While the results give good indication as to where to look for the error, they do not alone tell the entire story. This concept is further explored and the navigation errors are further decomposed in the sensitivity analysis described in Chapter 4.

During the transition between Ares I and SLS developments, the question of how the system insertion accuracy sensitivities would change was posed. SLS, then called Heavy Lift Vehicle (HLV), was to be a significantly larger vehicle with a significantly higher Mass To Orbit (MTO). Where Ares I utilized a single J2-X engine during Upper Stage flight, HLV would carry a much larger stage to orbit outfitted with multiple engines. From previous work with Ares I, the primary error sources were known. Re-examination of the J2-X engine transient showed that the resultant thrust uncertainty appeared to be uniformly distributed. Combining these engines would cause the uncertainty in the tail-off transient thrust to increase and become more normally distributed for engine counts of three and above. With regard to increasing mass, it was reasoned that the in-plane insertion error is a function of vehicle position and velocity error would decrease holding all other variables constant. The second order differential equation, Equation (2.10), depicts the relationship between the position, velocity, thrust, and mass.

$$\ddot{\vec{r}} = -\frac{\mu}{r^3} + \frac{\vec{F}_{Thrust}(t)}{m_{vehicle}(t)} + a_{peturbations} \tag{2.10}$$

From this relationship and Equation (2.3), a simplistic model was developed to approximate the effect of an increase in MTO for a number of HLV vehicle concepts. Combining this model with the conveniently linear impact footprint model, Figure 2.9, allows for the a coarse mapping of in-plane error and footprint displacement against MTO for number of J2-X engines, N_e. The requirements space for a number of vehicle concepts can be shown on a single chart for a specific target orbit, Figure 2.14.[63] The chart assumes tail-off transients uncertainties similar to that of the Ares I Upper Stage Engine per engine and not of the better characterized RS-25D engines.

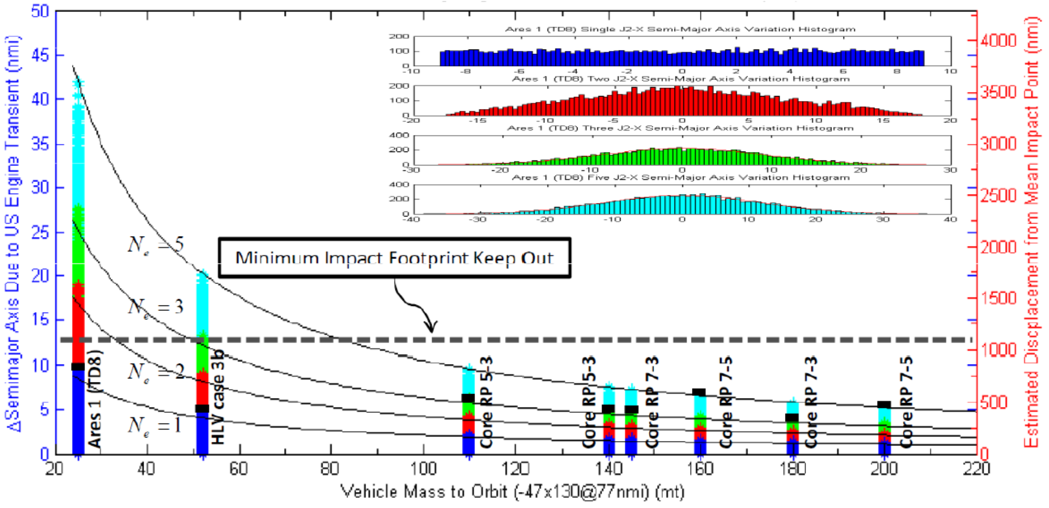

Figure 2.14

HLV Concepts, Estimated Delta SMA and Footprint vs. MTO

SLS will fly to an orbit different than the one analyzed in Figure 2.14, but the expectation was that for a vehicle with four engines to orbit and a significantly increased MTO, the navigation errors would become a more dominant error source for in-plane insertion errors.

Table 2.4 shows the parameter most highly correlated to the insertion error parameters, as determined by a SLS Monte Carlo analysis. At the top of the list is the initial attitude error in level for the in-plane error and initial attitude in azimuth for the out-of-plane errors. As the vehicle evolves to higher MTO configuration, the expectation is that the navigation error will become increasingly dominant in terms of insertion accuracy.

2.4.2 Requirements Analysis and Constraints Summary

In this Chapter, the ground work has been laid for a more detailed look into the Navigation system design. A design process has been roughly defined in Section 2.2. A coarse list of tasks required to design and analyze the launch vehicle Navigation system has been shown. Per step 1 in the list, two example configurations have been given and the mission objectives have been described in some detail. The Ares I mission was to insert the Orion crew module into orbit for rendezvous with the International Space Station (ISS) or for a mission to the moon. In both cases, the Ares I mission ended with the insertion of the crew vehicle into LEO. The interface, from a requirements perspective, was the accuracy by which the Orion spacecraft was inserted. The SLS mission currently consists of two parts. The first is the insertion of the second stage, ICPS, plus the Orion spacecraft as payload, into LEO. The second part of the mission includes the TLI maneuver inserting the Orion spacecraft into a trans-lunar orbit.

In Section 2.3, an analysis cycle has been presented, Figure 2.6, for a launch vehicle which utilizes inertial navigation and gyrocompassing for initial alignment. The process describes the analysis from requirements definition through vehicle analysis, Navigation

Table 2.4

SLS Insertion Error, Top Correlated Dispersions

Apogee Altitude	
Navigation Initial Attitude Error, level	-0.50
Core 3 Engine Thrust Dispersion	0.37
Core 2 Engine Thrust Dispersion	0.35
Core 4 Engine Thrust Dispersion	0.34
Core 1 Engine Thrust Dispersion	0.34
Navigation Unit Accelerometer Scale Factor, axial	-0.33
Navigation Unit Accelerometer Bias, axial	-0.12

Semi-major Axis	
Navigation Initial Attitude Error, level	-0.55
Core 3 Engine Thrust Dispersion	0.36
Core 2 Engine Thrust Dispersion	0.34
Core 4 Engine Thrust Dispersion	0.33
Core 1 Engine Thrust Dispersion	0.32
Navigation Unit Accelerometer Scale Factor, axial	-0.30
Navigation Unit Accelerometer Bias, axial	-0.12

Perigee Altitude	
Navigation Initial Attitude Error, level	-0.8
Core 3 Engine Thrust Dispersion	0.17
Core 2 Engine Thrust Dispersion	0.16
Navigation Unit Accelerometer Misalignment	0.15
Core 4 Engine Thrust Dispersion	0.13

Wedge Angle	
Navigation Initial Attitude Error, Azimuth	0.95
Navigation Unit East Gyro Bias	0.27

system analysis, and hardware specification. Sub-processes, where iteration is either necessary or probable, are indicated. Gates are included for the re-negotiation of vehicle level requirements, internal design, and component level hardware specifications. The diagram naturally fits an inertial navigation scheme but would require little, if any, modification for aided inertial navigation. Some of the Navigation system specifics referred to in the analysis cycle have been left out to this point in order to first provide an entry point into that process. That entry point also defines the metric by which the success of the process is determined and is indicated on the diagram by the orange box titled ”Ascent Target and Accuracy Requirement.”

Section 2.4 describes the insertion accuracy requirement, the parent requirement for navigation accuracy-related requirements. The requirement has been decomposed into natural components, in-plane and out-of-plane error. Vehicle sensitivities to insertion error have been assessed through examination of Monte Carlo data from the 6-DOF vehicle simulation. An approach to sizing the insertion accuracy based upon key sensitivities and governing requirements has been presented. Those key sensitivities were re-entry impact footprint and payload mass margin required for orbit correction. Through examination of Monte Carlo data and dispersion to error correlation data from the 6-DOF vehicle simulation, the primary contributors to insertion error have been identified. An approach to allocating the navigation portion of the error has been presented based on data for an Ares I type mission to LEO with consideration for limiting out-of-plane error for rendezvous with the ISS.

The constraint analysis in Section 2.4 attempts to extend the Ares I required mission accuracy to SLS through the examination of the sensitivities to increased number of engines and MTO. Consideration of the second part of the SLS mission is not included. Figure 2.5 omits a critical point(s) after phase 4, ICPS/Orion separation, on the Orion lunar free-return trajectory. The missing point or points represents the execution of trajectory correction maneuvers by Orion to correct for errors inherited during the TLI maneuver. The analysis required to constrain this mission is much more complex and reserved for detailed analysis in Chapter 4.

To this point, the requirements which govern the Navigation sub-system have been explored in an attempt at preliminary sizing. The allocation of the insertion accuracy to navigation accuracy represents an interface in requirements space to the navigation system. Some assumptions about the Navigation system architecture are required to develop the sensitivities required for the initial navigation error allocation and for defining sensitivities. Prior to detailed trade studies, the starting point for the Ares I navigation hardware was a LN-100 Inertial Measurement Unit (IMU) originally developed by Litton, before purchase by Northrup Grumman. [35] SLS began with the Ares I RINU which was at Preliminary Design Review (PDR) maturity at the time that the program was officially terminated. Using the allocations developed from the system requirements analysis, the definition of the Navigation sub-system itself can begin. Figure 2.15 depicts this interface to the Navigation system in requirements space between the top level and bottom levels of the diagram. The definition of the navigation accuracy leads to the definition of the Navi-

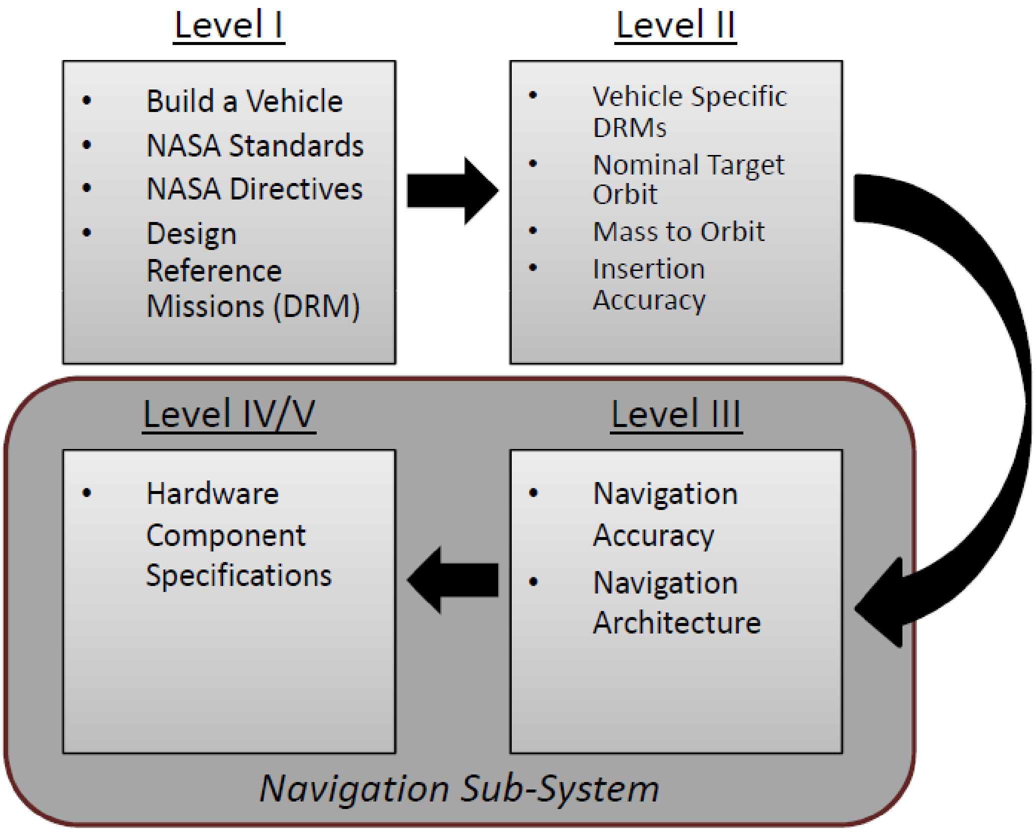
Level I
Build a Vehicle
NASA Standards
NASA Directives
Design Reference Missions (DRM)
Level II
Vehicle Specific DRMs
Nominal Target Orbit
Mass to Orbit
Insertion Accuracy
Level IV/V
Hardware Component Specifications
Level III
Navigation Accuracy
Navigation Architecture
Navigation Sub-System

Figure 2.15

Abridged Requirements Flow-down to Navigation Sub-System gation System architecture. Once the architecture has been defined, required hardware can be identified and specifications can be developed.

2.4.3 Navigation Architecture and Technologies

There is much variation in the implementation of modern Navigation systems. Most are specific to the different measurement data available and the application of the navigating vehicle. Different applications place different constraints on navigation. Some common constraints for navigation design are in cost, required accuracy, mass, observability, power, operational environment, and time of flight. For instance, a navigation system designed for a satellite with star trackers, a low grade IMU, and a GPS receiver may not be well suited for a launch vehicle with a six to ten minute of powered flight from the ground. Likewise, a large gimballed IMU based system designed for a submersible vehicle would be a poor choice for a ground to air missile. Launch vehicle navigation design has to consider flight times measured in minutes, environments that are not benign, and the importance of an accurate knowledge of attitude for vehicle control in a dynamic environment.

Two fundamental and distinctively different navigation principals applicable to launch vehicles are modern implementations of position fixing and dead reckoning. They are distinctively different and yet complimentary from the perspective of inherent error and error growth.

2.4.3.1 Position Fixing

The method of position fixing entails the determination of the observer's position by way of external observations. One of the oldest methods of navigation is by determining the ranges to multiple known landmarks optically and then computing a position from the observed measurements. A classic terrestrial example of position fixing is the determination of a ships position by triangulation with observations in range to known landmarks. If the height of the object is known then the range can be ascertained through some knowledge of geodesy, e.g. Earth curvature. Alternatively, the range measurements does not have to be taken directly, but rather the angular displacement between the observations from the perspective of the observer can be used to determine the relative distances. When plotted on a map, these observations are often called lines of precision.

In lieu of plotting lines of precision on a chart or taking angular measurements based on compass bearings, direct range measurements can be used. Pre-modern maritime range measurements could be taken by use of sextant and the understanding that the perceived height of an object is proportional to the distance from which the object is observed. Equation (2.11) can be used to calculate the position of an observer, u, from range measurements, ρ, within a plane and requires only two observations or landmarks, L. A system of two equations can be developed from the general form.

$$\rho_i = ||\vec{L}_i - \vec{u}|| \tag{2.11}$$

$$\rho_1 = \sqrt{(u_x - [L_1]_x)^2 + (u_y - [L_1]_y)^2}$$

$$\rho_2 = \sqrt{(u_x - [L_2]_x)^2 + (u_y - [L_2]_y)^2}$$

In addition to optics, modern instruments utilize a time of flight concept. That is, a radio wave has a has a time of flight proportional to the distance traveled and a power proportional to the reciprocal of the square of the distance traveled. If the time of flight can be determined then so can the distance traveled, assuming a constant rate. Range measurements of this variety can be used for launch vehicle, aeronautical, and submersible application as well as modern terrestrial applications utilizing radio waves and sound waves, e.g. radar and sonar.

The most relevant modern implementation of position fixing is the use of GNSS. Kaplan covers the mechanics and use of GNSS in great detail. [33] GPS is an example of GNSS. In the case of a GPS, the range measurements are also not taken directly. Satellites within a constellation each broadcast unique signals known as pseudo-random codes (PRC). The PRCs are pseudo-random, because they are random but predictable i.e. determinant. The PRCs are matched against what they are known to be at a particular time and a time of travel is calculated based upon the speed at which the signal travels. Ranges are then calculated based upon the time of traveled referenced to the receiver clock. The GPS satellites maintain extremely accurate time ($\sim 100ns$) that is synchronized between them periodically to minimize relative drift; however, the receiver clock often is not as accurate. Due to this and the dependency of the range measurement on time, a time bias between the receiver clock and satellite clock must also be solved for and the range measurements, known as pseudo ranges, become a function of this delta-time. Since the time offset must also be solved for, the simplest implementation of position fixing with GPS requires 4 observations, or solutions from 4 satellites. The position state is then attained by solving the system of non-linear pseudo-range equations, Equation (2.13). The systems of equations is developed from the pseudo range definition as a function of the satellites position, the receivers position, an expression for the system time offset, and the speed of light, Equation (2.12).

$$\rho_i = \|\vec{s}_i - \vec{u}\| + ct_u \tag{2.12}$$

$$\begin{aligned}
\rho_1 &= \sqrt{(x_1 - x_u)^2 + (y_1 - y_u)^2 + (z_1 - z_u)^2} + ct_u \\
\rho_2 &= \sqrt{(x_2 - x_u)^2 + (y_2 - y_u)^2 + (z_2 - z_u)^2} + ct_u \\
\rho_3 &= \sqrt{(x_3 - x_u)^2 + (y_3 - y_u)^2 + (z_3 - z_u)^2} + ct_u \\
\rho_4 &= \sqrt{(x_4 - x_u)^2 + (y_4 - y_u)^2 + (z_4 - z_u)^2} + ct_u
\end{aligned} \tag{2.13}$$

In principal, the method of position fixing remains the same as it was in early maritime history. This is illustrated in the similarity between the range measurement relationships, Equation (2.11) and (2.12). The GPS paradigm presented in Equation (2.13) assumes otherwise ideal measurements for the pseudo ranges and does not consider measurement error, uncertainties in signal propagation, or geometric dilution of precision. With measurement error taken into account, the point becomes an error ellipse. In practice, GPS receivers generally use more range measurement than the minimum, limited only by the capability of the hardware and the number of satellites in view. The method of solving for the state often includes the estimation of errors sources inherent to GPS. Montenbruck summarizes methods of positioning fixing for navigation in his book along with accuracy metrics for multiple implementations.[46] Table 2.5 summarizes these accuracies.

Table 2.5

Range and Tracking Source Accuracy

Range Source	Approximate Accuracy
Ground Based Angle Tracking	100m to 3km
Ground based Ranging (S-band)	1m to 50m
Relay Satellite Tracking (TDRS)	1m to 10m
GNSS (GPS)	10cm to 1m
Satellite Laser Ranging	1cm to 12cm

2.4.3.2 Dead Reckoning and Inertial Navigation

The other classic navigation method to be discussed in this thesis, in greater detail than position fixing, is dead-reckoning. The formal definition of dead reckoning is the determination of the position of a craft based solely on the record of its direction and distance of its course.[45] For application to launch vehicles, dead reckoning is a process by which initial state, heading, and velocity are used to determine position at some later time. The modern implementation of dead-reckoning in navigation is often referred to as inertial navigation. From Grewel, inertial navigation uses gyroscopes and accelerometers to maintain an estimate of the vehicle position, velocity, and attitude states and attitude rates.[22] Navigation systems which rely only on inertial measurements have been used extensively with regard to launch vehicles. In fact, it is said by some sources that the application to rocket navigation and control was the sole reason for the development of modern inertial navigation systems.[34] It also offers rationale for the strict control of navigation grade inertial measurement hardware by the US Department of State.

Inertial Navigation Systems (INS) employ gyroscopes and accelerometers to measure change in orientation and specific force, or non-gravitational acceleration. The sum of the specific force and the gravitational acceleration is integrated to determine the velocity state which is in turn integrated on the INS computer to calculate the position state. Angular rate measurements from the gyroscopes are used to maintain the sensed acceleration in the correct frame. Inertial navigation systems fit into two basic categories. How the orientation of the platform on which the accelerometers are affixed is maintained defines the INS as either a gimbaled or strapdown system.[22]

For a discussion of gimballed versus strapdown systems, the sensor and navigation frames must be defined. The coordinate frame in which the gyro and accelerometer measurements are taken is referred to as the sensor frame. The acceleration is integrated for the position and velocity states in the navigation frame. In a traditional gimballed platform inertial navigation system, the sensor frame is maintained with respect to the navigation frame physically. Platform fixed resolvers measure the angular displacement of the platform. Torque commands opposite the measurements are developed to null the platform angular rate, effectively maintaining a constant alignment with respect to the navigation frame, physically. The accelerometers are mounted to the platform whose coordinate axes are traditional maintained parallel to the navigation frame coordinate axes and not fixed in orientation to the vehicle. The accelerometer measurements can be integrated directly for the position and velocity states in the navigation, or platform, frame, and the sum of the gyro angular measurements represent the change in vehicle attitude from when the platform reference was fixed.

In a traditional strapdown system, the mechanization is different. In this case, the platform is physically strapped down to the vehicle. Generally, the accelerometers are fixed to the vehicle and the relative alignment of the platform frame to the navigation frame is maintained mathematically. The gyro measurements are continuously integrated to compute the transformation between the navigation frame and the sensor frame. The vehicle fixed accelerometer measurements are transformed into the navigation frame prior to integration. The vehicle attitude is expressed as a function of the sensor frame to navigation frame transformation. The strapdown mechanization is discussed further in Chapter 3.

Gimballed platform inertial navigation systems have been used on many launch vehicles from Saturn V, Shuttle, Minuteman, Peacekeeper, Trident, etc.. They are almost exclusively used in strategic application. The most interesting of the gimballed systems is the Advanced Inertial Reference Sphere (AIRS) developed by the Charles Stark Draper Laboratory and employed on Peacekeeper. The AIRS defies traditional launch vehicle navigation error budgets where the navigation accuracy comprises a large portion of the injection accuracy. It is described as a perfect navigation system but at an extreme cost in dollars, complexity, and schedule.[40] Strapdown inertial navigation systems are flown on modern launch vehicles including Atlas and Delta EELVs, and Orbital Sciences current line of launch vehicles.

Although the category names, gimballed and strapdown, reference the physical implementation of the systems, the discerning feature is algorithmic. Wang discusses a hybrid in which a mechanically gimballed IMU could be configured for thrust following. In such a configuration, the platform would maintain alignment with the vehicle thrust vector. Strapdown navigation algorithms would be used to track the orientation of the thrust vector fixed platform frame to the navigation frame. The advantages and disadvantages of each mechanization is discussed independently in detail by both Savage and Wang.[83][73]

The clear advantage of inertial navigation systems, independent of mechanization, is that they are completely autonomous. There is no dependence upon external sources once initialized. This prohibits the ability to block, jam, or otherwise interfere with an inertial navigation system. Wang points out that strategic systems must be designed for multiple nuclear events where the GPS constellation may be rendered unavailable.

Inertial navigation systems have very high data output rates making them ideal for dynamic environments and they are not slave to line of sight or other environmental concerns associated with position-fixing techniques. They are not subject to concerns of shading, multi-path, loss of lock, or additional environmental uncertainties.

A sometimes cited disadvantage of the use of an inertial navigation system is the requirement of an accurate knowledge of gravity. This con is easily dismissed given modern computational capability and the fidelity of available gravity models. Further, the sensitivity of a reasonable gravity anomaly to the associated state error is particularly weak as compared to other errors sources. This is not to say that gravity anomalies should not be considered, but that the sensitivity of in plane error at insertion for a small to medium sized launch vehicle is dominated by other error sources, e.g. engine shutdown transients, accelerometer scale factors.

2.4.3.3 Aided Inertial Navigation

Unlike gravity model dependence, a definite weakness for inertial navigation and dead reckoning, in general, is the heavy dependence upon an accurate initial state. There are methods by which the system can autonomously estimate its initial attitude through a process known as gyrocompassing, discussed in Chapter 3. Special consideration must be given to the initial state due to the fact that an inertial system without external aiding, regardless of implementation, can at best only produce the change in state from some original reference state. After estimation of an initial state, such a navigation system relies on the quality of the instruments employed and the design of its algorithms, but more so on instrument quality, to maintain the accuracy of the initial state. As a result, the error in the state becomes a function of time which can grow without bound, Figure 2.16.

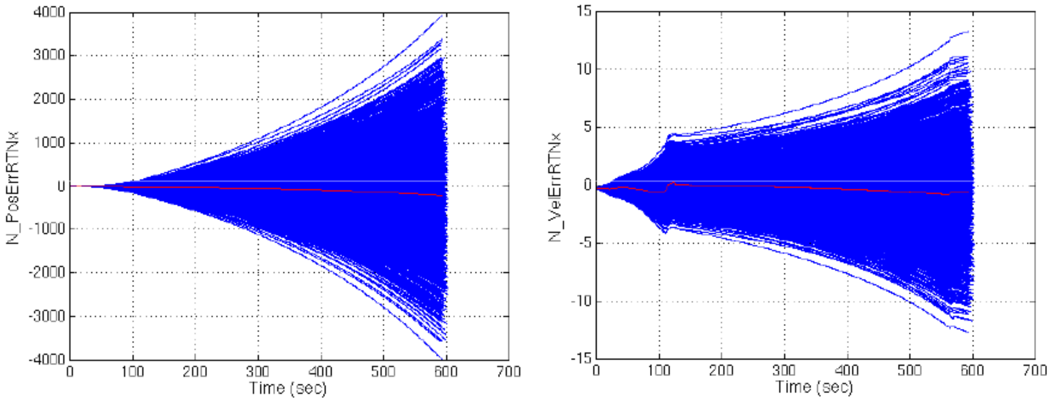

Figure 2.16

Inertial Navigation, Position and Velocity Error Growth in Time

Position fixing in general is the ideal partner for inertial navigation due to the methods being independent and complimentary in terms of strengths and weaknesses. Where the inertial navigation system accuracy is a strong function of initial state and time of flight, position fixing is not. Where position fixing may have difficulty with determination of an adequate attitude and velocity solution, inertial does not. Inertial navigation systems will provide accurate angular rate and acceleration measurements needed for control where position fixing does not directly. An inertial solution can also be available at the sensor sampling rate and can track the vehicle state in between GPS measurement updates. Inertial solutions can also aid GPS with the estimation of errors and by providing for rapid re-acquisition after periods of loss of signal lock. This should allow for a more cost effective system than with an INS alone where a high accuracy solution is required. The major benefit to an integrated navigation system is the decoupling of the overall system accuracy from the initial attitude solution. The combination of the two fullfills the requirement for an inertial navigation system while offering significantly increased accuracy in position and velocity state determination. [33] This is proven in Chapter 4.

CHAPTER 3

NAVIGATION SYSTEM MODEL DEVELOPMENT

3.1 Navigation Model Architecture

Key to any Navigation system design and analysis is the Navigation system model. The model allows for analysis of the Navigation system to be performed and for the emulation of the Navigation system in the vehicle simulation. Figure 3.1 depicts a general software architecture for an INS model from a model based design perspective. The model based design paradigm assumes that all pertinent design details are in some way captured within the model. The model paradigm allows for a common code to be used inside and outside of the vehicle simulation. The components of the model include the input interface, the instrument error model, the navigation software model, the system error model, the output interface, and data files which contain the model configuration. The INS model is wrapped in code that allows for integration into the vehicle simulation model or into a standalone analysis testbed without modification. Not shown in the diagram is the extensive pre- and post-processing libraries associated with analysis in both configurations. The remainder of this Chapter will attempt to define the individual pieces in the model architecture.

At the time of writing, the model based design paradigm has not been completely implemented. The vehicle and analysis code exist separate of one another but are consistent. The analysis code contained in NEAT considers much more than the INS model in terms

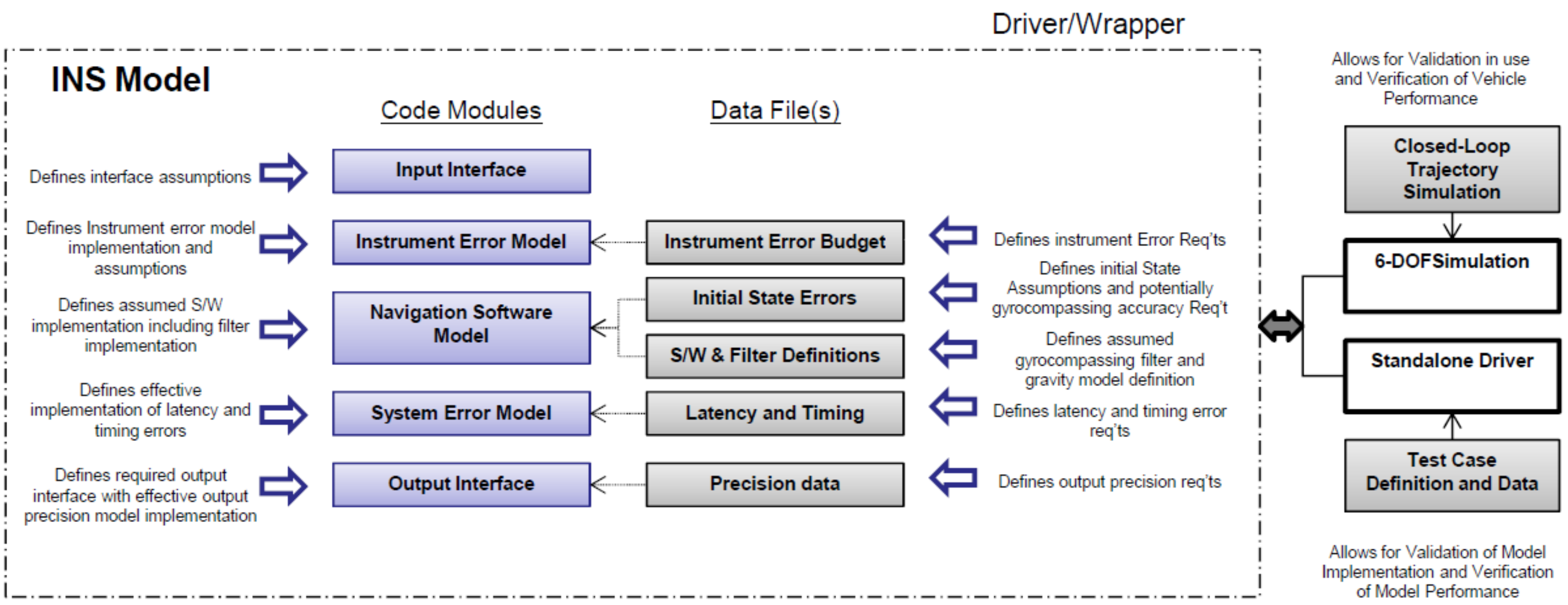
Driver/Wrapper
INS Model
Code Modules
Data File(s)
Defines interface assumptions
Input Interface
Defines Instrument error model implementation and assumptions
Instrument Error Model
Instrument Error Budget
Defines instrument Error Req'ts
Defines initial State Assumptions and potentially gyrocompassing accuracy Req't
Initial State Errors
Defines assumed S/W implementation including filter implementation
Navigation Software Model
S/W & Filter Definitions
Defines assumed gyrocompassing filter and gravity model definition
Defines effective implementation of latency and timing errors
System Error Model
Latency and Timing
Defines latency and timing error req'ts
Defines required output interface with effective output precision model implementation
Output Interface
Precision data
Defines output precision req'ts
Allows for Validation in use and Verification of Vehicle Performance
Closed-Loop Trajectory Simulation
6-DOFSimulation
Standalone Driver
Test Case Definition and Data
Allows for Validation of Model Implementation and Verification of Model Performance

Figure 3.1

INS Model Architecture

of navigation error analysis capability, but it does not include vehicle system level errors that impact the other GN&C sub-systems or vehicle closed loop performance unless required for navigation specific analysis. Transition to the model based approach is expected to reduce overhead associated with cross-validation of the individual implementations and bring additional fidelity into the vehicle simulation for SLS development.

The model diagram in Figure 3.1 offers insight into the construction of the model but does not give detail to the flow of data through the model. Figure 3.2 is a data flow diagram from Ares I Navigation System development.[60] In the diagram, the flow of data, or information contained in the trajectory angular rate and specific force quantities at the input interface, through the model components is more readily seen. Those components consist of the instrument error model, the navigation software, the system error model, and the output interface. The detailed components of this data flow diagram are discussed throughout this chapter. The component discussions are sectioned according to the INS Model architecture diagram.

3.2 The INS Input Interface

Under the INS Model paradigm, the input interface is what the simulation wrapper or standalone driver provide to the INS model and what the INS model does to the data in order to support subsequent model sub-elements.

3.2.1 Trajectory Truth

First, the sensor truth angular rates and accelerations must be calculated for simulation as they would be observed by the inertial navigation system. The truth angular rates and

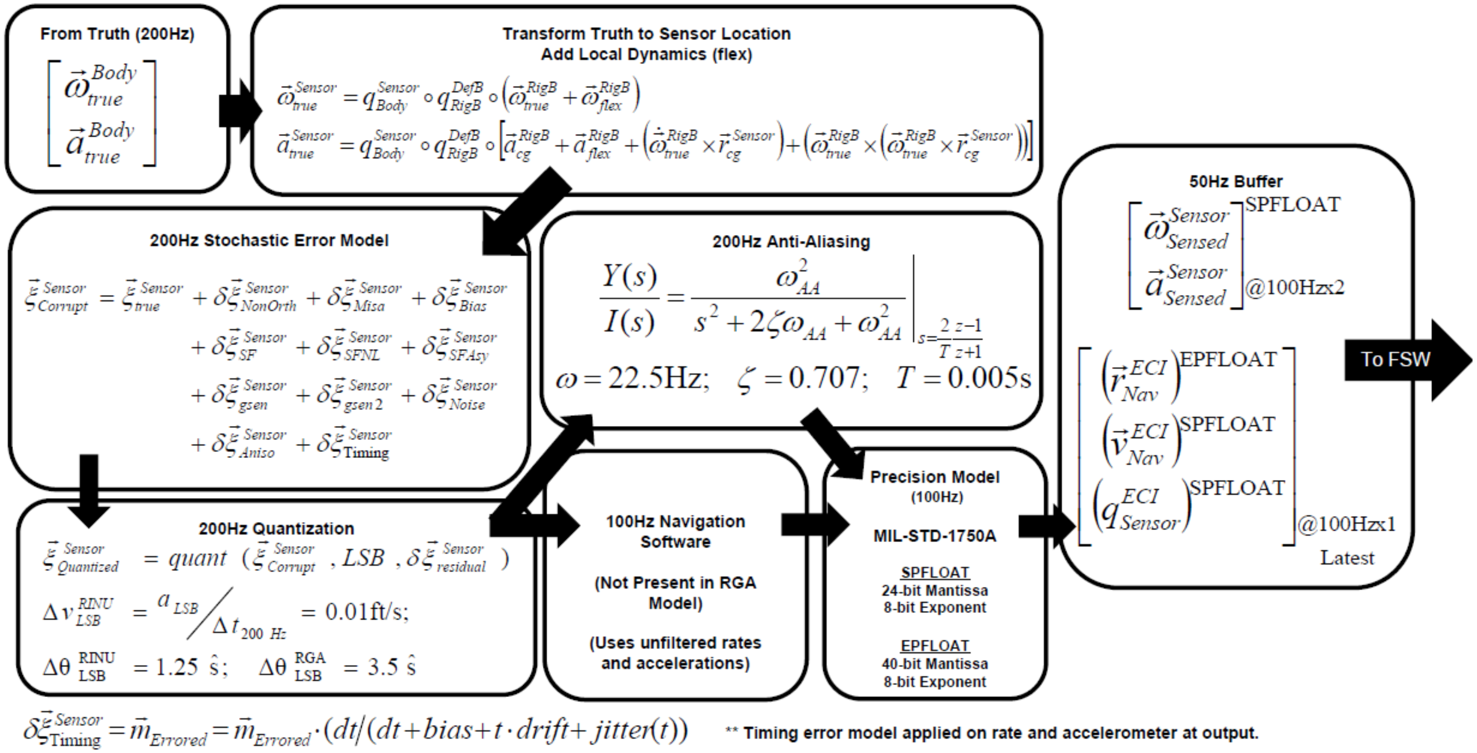
From Truth (200Hz)
$\begin{bmatrix} \vec{\omega}_{true}^{Body} \\ \vec{a}_{true}^{Body} \end{bmatrix}$
Transform Truth to Sensor Location
Add Local Dynamics (flex)
$\vec{\omega}_{true}^{Sensor} = q_{Body}^{Sensor} \circ q_{RigB}^{DefB} \circ \left(\vec{\omega}_{true}^{RigB} + \vec{\omega}_{flex}^{RigB}\right)$
$\vec{a}_{true}^{Sensor} = q_{Body}^{Sensor} \circ q_{RigB}^{DefB} \circ \left[\vec{a}_{cg}^{RigB} + \vec{a}_{flex}^{RigB} + \left(\dot{\vec{\omega}}_{true}^{RigB} \times \vec{r}_{cg}^{Sensor}\right) + \left(\vec{\omega}_{true}^{RigB} \times \left(\vec{\omega}_{true}^{RigB} \times \vec{r}_{cg}^{Sensor}\right)\right)\right]$
200Hz Stochastic Error Model
$\vec{\xi}_{Corrupt}^{Sensor} = \vec{\xi}_{true}^{Sensor} + \delta\vec{\xi}_{NonOrth}^{Sensor} + \delta\vec{\xi}_{Misa}^{Sensor} + \delta\vec{\xi}_{Bias}^{Sensor} + \delta\vec{\xi}_{SF}^{Sensor} + \delta\vec{\xi}_{SFNL}^{Sensor} + \delta\vec{\xi}_{SFAsy}^{Sensor} + \delta\vec{\xi}_{gsen}^{Sensor} + \delta\vec{\xi}_{gsen2}^{Sensor} + \delta\vec{\xi}_{Noise}^{Sensor} + \delta\vec{\xi}_{Aniso}^{Sensor} + \delta\vec{\xi}_{Timing}^{Sensor}$
200Hz Anti-Aliasing
$\frac{Y(s)}{I(s)} = \frac{\omega_{AA}^2}{s^2 + 2\zeta\omega_{AA} + \omega_{AA}^2}\Big|_{s=\frac{2}{T}\frac{z-1}{z+1}}$
$\omega = 22.5\text{Hz}; \quad \zeta = 0.707; \quad T = 0.005\text{s}$
200Hz Quantization
$\vec{\xi}_{Quantized}^{Sensor} = quant\left(\vec{\xi}_{Corrupt}^{Sensor}, LSB, \delta\vec{\xi}_{residual}^{Sensor}\right)$
$\Delta v_{LSB}^{RINU} = a_{LSB} / \Delta t_{200\ Hz} = 0.01\text{ft/s};$
$\Delta\theta_{LSB}^{RINU} = 1.25\ \hat{s}; \quad \Delta\theta_{LSB}^{RGA} = 3.5\ \hat{s}$
100Hz Navigation Software
(Not Present in RGA Model)
(Uses unfiltered rates and accelerations)
Precision Model
(100Hz)
MIL-STD-1750A
SPFLOAT
24-bit Mantissa
8-bit Exponent
EPFLOAT
40-bit Mantissa
8-bit Exponent
50Hz Buffer
$\begin{bmatrix} \vec{\omega}_{Sensed}^{Sensor} \\ \vec{a}_{Sensed}^{Sensor} \end{bmatrix}^{SPFLOAT}$ @100Hzx2
$\begin{bmatrix} \left(\vec{r}_{Nav}^{ECI}\right)^{EPFLOAT} \\ \left(\vec{v}_{Nav}^{ECI}\right)^{SPFLOAT} \\ \left(q_{Sensor}^{ECI}\right)^{SPFLOAT} \end{bmatrix}$ @100Hzx1
Latest
To FSW
$\delta\vec{\xi}_{Timing}^{Sensor} = \vec{m}_{Errored} = \vec{m}_{Errored} \cdot \left(dt / \left(dt + bias + t \cdot drift + jitter(t)\right)\right)$
** Timing error model applied on rate and accelerometer at output.

Figure 3.2

Ares I Sensor Model for Closed-Loop Simulation accelerations, denoted by $\vec{\omega}^{cg}_{Inertial,true}$ and $\vec{a}^{cg}_{true}$, are the true instantaneous angular rate and specific force at the vehicle center of gravity. Note that the specific force measurement is equal to the total acceleration less the influence of gravity. Equations (3.1) and (3.2) describe the transformation between vehicle true angular rates and accelerations at the center of gravity to the true rates and specific force quantities at the sensor location. The sensor acceleration includes centripetal and tangential terms. Coriolis and other terms are omitted for two reasons. The relative size of the other terms makes them negligible. The dependence upon the relative velocity, of the center of gravity and the sensor, requires special considerations for transients in the trajectory to avoid singularities. This is particularly an issue at staging events.

$$\vec{\omega}^{Sensor}_{Inertial,true} = q^{Sensor}_{body} \circ q^{Deformed}_{Rigid} \circ \left(\vec{\omega}^{Rigid}_{Inertial,true} + \vec{\omega}^{Sensor}_{Rigid,Flex} \right) \tag{3.1}$$

$$\begin{aligned} \vec{a}^{Sensor}_{true} = q^{Sensor}_{body} \circ q^{Deformed}_{Rigid} \circ \Bigg[& \vec{a}^{Rigid}_{cg} + \vec{a}^{Rigid}_{flex} + (\dot{\vec{\omega}}^{Sensor}_{true,Rigid} \times \vec{r}^{Sensor}_{cg}) \\ & \ldots + (\vec{\omega}^{Sensor}_{true,Rigid} \times (\vec{\omega}^{Sensor}_{true,Rigid} \times \vec{r}^{Sensor}_{cg}) \Bigg] \end{aligned} \tag{3.2}$$

Equations (3.1) and (3.2) also allow for the inclusion of local angular rate and local acceleration due to flexible body dynamics, $\vec{\omega}^{Sensor}_{Rigid,flex}$ and $\vec{a}^{Rigid}_{flex}$ respectively. Note that if flexible body dynamics are included, the associated transformation between the rigid body frame, in which the acceleration is resolved, and the deformed frame must be maintained. Not including the rigid body to deformed body transformation, $q^{Deformed}_{Rigid}$, can result in a large artificial attitude error.

3.2.2 Sub-Step Size Latency and Sensor Dynamics

One of the problems associated with a discrete simulation is that the equations of motion are only evaluated at discrete time steps. Increasing the simulation frequency can result in a significantly increased computational burden and a delay in producing results. The simulation of sub-step size latencies becomes difficult given that the process of simply holding the data until the next evaluation of the model can introduce substantially larger latencies than intended. If the system were continuous, the latency would be simulated with a delay of size T, Equation (3.3).[14]

$$G_{delay}(s) = e^{-sT} \tag{3.3}$$

The pure delay without attenuation can be approximated in the discrete time domain through the use of a Padé approximation. Equation (3.4) gives the continuous transfer function for a fourth order Padé approximation to the delay. [82]

$$e^{-sT} \approx \frac{1680 - 840sT + 180(sT)^2 - 20(sT)^3 + (sT)^4}{1680 + 840sT + 180(sT)^2 + 20(sT)^3 + (sT)^4} \tag{3.4}$$

In addition to the sub-time step delays, any known sensor dynamics need to be included in the sensor transfer function as part of the input interface code module. It is common for gyros and accelerometers to be isolation mounted to mitigate shock and vibration environments. The isolation also helps with reducing error from coning, sculling, and sensor cross-axis sensitivities. Coning and sculling are kinematics errors in the navigation state resulting from the motion of the instruments while sampling and the principal that angular rate is not cumulative. Vibration does not cause coning and sculling errors, but it can increase the amount of coning and sculling motion and the error due to deficiencies in the coning and sculling compensation algorithms within the inertial navigation equations. These terms are discussed further in the section on Navigation Software. If the isolator natural frequency is of low frequency relative to the GN&C Nyquist frequency, then gain and phase distortion due to the isolator should be modeled for the controller design and in the closed-loop vehicle simulation. The Nyquist frequency is defined as one half the total bandwidth.

Rubber isolators exhibit a natural peak gain at the resonance frequency around the isolator natural frequency. Special attention should be paid to the magnitude of this gain and the relative distance to the Nyquist frequency. It is also important to note that the translational and rotational response of the isolation will differ. The rotational response, applied to the angular rate channel, will be a function of the translational response and mass matrices of the isolated sensor block. It is not uncommon to model mechanical isolation with a second order transfer function. The second order transfer function for a mechanically isolated dynamic system is given in Equation (3.5).[64]

$$TF_{iso}(s) = \frac{2\zeta\omega_n s + \omega_n^2}{s^2 + 2\zeta\omega_n s + \omega_n^2} \tag{3.5}$$

The product of the two systems, from the delay and the mechanical isolator, result in a sixth order transfer function. The transfer function for the delay and the isolation can be analyzed together. The transformation of the continuous s-domain transfer functions into the discrete time z-domain can be accomplished in Python by use of the signals toolbox in the SciPy library or with the Control System Toolbox in Matlab.

3.2.3 High Frequency Environment

Another byproduct of a fixed step-size is that the dynamics are only accurate, at best, below the simulation Nyquist frequency. The dynamics may be inaccurate at far less than the simulation Nyquist depending on the flexible body dynamics model. Some navigation errors are only fully realizable in the presence of high frequency dynamics. Examples would be residual coning and sculling motion and rectification errors in which motion along two axes produces a bias along the third axis as a result of cross-coupling error sensitivities.

For simulation of high frequency dynamics on the input to the model based on a random vibration environment, a colored noise can be added to the input measurements. The colored noise can be derived from a white noise that has been operated on by a shaping filter. For analysis of the RINU anti-aliasing filter performance, a high order Finite Impulse Response (FIR) filter was designed to fit the RINU random vibration environment specification. The FIR filter is effectively a weighted moving average with order, N, defining the window size, Equation (3.6). In the model, the FIR filter is supplied a Gaussian white noise input from a normal random number generator to produce the colored signal. The colored noise is then superpositioned onto the truth measurement.[64]

$$TF_{FIR_N}(z) = \sum_{n=0}^{N} b_n z^{-n} \tag{3.6}$$

3.2.4 Gravity Anomaly

The accelerometers measure specific force and not total acceleration which is what is used for navigation. The two quantities differ by the local acceleration due to gravity. In the inertial navigation algorithm, a model of gravitational acceleration is used to compute the total acceleration. The difference in solution obtained from the gravity model and the true local gravity is termed the gravity anomaly. The gravity anomaly is an error which should be modeled. The gravity anomaly is introduced into the system through the truth model as an error on the specific force measurement to navigation. When the navigation algorithm compensates for the lack of the acceleration due to gravity in the measurement, the error that was introduced becomes an uncompensated error in acceleration.

It is assumed that the gravitational acceleration is well known at launch. The gravity anomaly is implemented as a first order Gauss-Markov process. The Gauss-Markov is correlated through the time constant to the absolute distance traveled from the launch site. The square-root of the variance is chosen to represent the acceleration, in micro-g's, of the estimated error along the flight path for the gravity model implemented in the truth simulation.

3.3 The Instrument Error Model

The basis for the development of the error model is described by the basic error model given in Equation (3.7) and graphically described by Figure 3.3. This general concept is consistent with standards published by the Institute of Electrical and Electronic Engineers (IEEE) for gyro and accelerometer error modeling summarized by Cicci's report on error modeling for different types of instruments.[10] The figure depicts a set of five independent errors. The errors are input dependent and are used to generally describe the output as a function of the input for a given error term.

$$
\begin{aligned}
Output &= Input + Bias + K_{linear} \cdot Input + K_{Other} \cdot f(Input) \\
&+ RandomWalk(t) + Misalignment(Input) + Quantization(Input) + \ldots
\end{aligned}
\tag{3.7}
$$

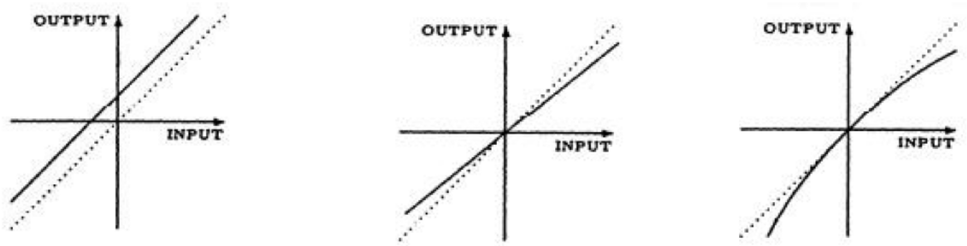

a) Bias *b) Scale Factor* *c) Scale Factor Non-Linearity*

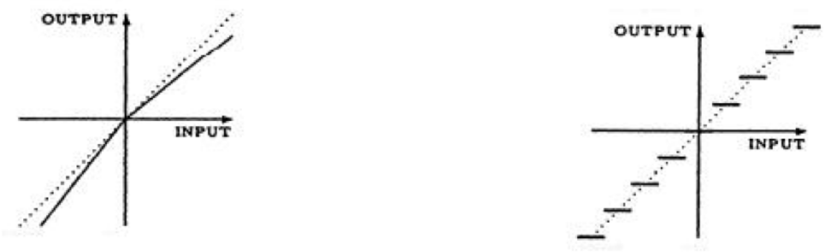

d) Scale Factor Asymmetry *e) Quantization*

Figure 3.3

Basic Error Model Components

The bias and scale factors for a particular instrument can each be specified by a single parameter for the expected error after instrument calibration and measurement compensation. The residual error, or error after compensation from calibration, is usually assumed Gaussian and related with a standard deviation. The quantization error is non-linear. The quantization process is deterministic. Quantization can be specified with a fixed value of measurement unit per count. Due to the diversity in sources and methods in which quantization can be handled, it is treated separate of the other errors.

In Equation (3.7) the scale factor errors have been simplified to three terms, the linear scale factor, scale factor assymetry, and non-linearity. It is not uncommon to see higher order scale factor terms lumped together into one term for scale factor non-linearity in inertial instrument product specification sheets. For a gyro, the specification is often a function of the full scale output. In such a case, the non-linearity model is derived considering the second order scale factor, K_2, only, Equation (3.8).

$$Output - Input = K_2 * Input^2$$

Differentiating, Equation (3.8) gives a linear expression that can be directly described by a scalar given no offset. The slope of this derivative can be described by one point and the slope at that point. Typically this is given as a 1σ value at Full Scale, FS, but any reference is valid. Assuming the definition of the model, and Full Scale Output is given as a reference, the slope of the derivative can be described by Equation (3.8).

$$\frac{d^2Output}{dInput^2} = 2 \cdot K_2 = \frac{\left(\frac{dOutput}{dInput}\right)_{FS}}{Input_{FS}} = Constant \tag{3.8}$$

Symmetry is assumed, i.e. given no offset the error due to non-linearity is zero for zero input and shows maximum deviation for Input equal to Full Scale. Solving for K_2, yields the model for such a specification, Equation (3.9).

$$K_2 = \frac{\left(\frac{dOutput}{dInput}\right)_{FS}}{2 \cdot Input_{FS}} \tag{3.9}$$

The error model assumes the 1-sigma value given for non-linearity to be the first derivative of the input over the output at some reference input value. For example, if the non-linearity is given as 10 parts per million of full scale, where full scale is +/- 100 deg/s, the non-linear scale factor, K_2, would be 10 PPM/(2*100deg/s).

The assumed 1-sigma error due to non-linearity for angular rate measurements can be described as a function of the Input angular rate and the gyro Full Scale. Likewise, the acceleration can be described as a function of the Input acceleration, but for accelerometers, non-linearity is commonly specified per g implying a reference of 1g as opposed to Full Scale. The general equations for error due to non-linearity for a gyro and an accelerometer are shown as Equations (3.10), (3.11), and (3.12).

$$\delta Output_{NonLinearity} = \frac{\sigma_{NonLinearity}}{2 \cdot FS} \cdot Input^2 \tag{3.10}$$

$$\delta \vec{\omega}_{NonLinearity} = \frac{\sigma_{NonLinearity}}{2 \cdot FS} \cdot (\vec{\omega}_{true}^{Sensor})^2 \tag{3.11}$$

$$\delta \vec{a}_{NonLinearity} = \sigma_{NonLinearity} \cdot (\vec{a}_{true}^{Sensor})^2 \tag{3.12}$$

Note that unlike accelerometer non-linearity, little information is available in the literature for non-linearity error for ring laser gyros on specification or cause.[52]

If information regarding higher order scale factor terms is available, they should be modeled. Equation (3.14) and 3.15 provide expressions for scale factor errors up to third order for accelerometers and gyros. Cross-coupling terms have been included in the expression. The squared terms and the cross-coupling terms comprise the g^2 accelerometer and gyro sensitivity.

$$\vec{\delta a}_{K_{Other}} = Diag_{(3\times3)} \begin{bmatrix} a_x^2 \\ a_y^2 \\ a_z^2 \end{bmatrix} \sigma_{K2}^{accelerometer} + Diag_{(3\times3)} \begin{bmatrix} a_x^3 \\ a_y^3 \\ a_z^3 \end{bmatrix} \sigma_{K3}^{accelerometer} \tag{3.13}$$

$$+Diag_{(3\times3)} \begin{bmatrix} a_y a_z \\ a_x a_z \\ a_y a_x \end{bmatrix} \left(\sigma_{K_{ip}}^{accelerometer} + \sigma_{K_{io}}^{accelerometer} + \sigma_{K_{op}}^{accelerometer} \right)$$

For pendulous accelerometers, the cross-coupling term along the accelerometer input axis, K_{ip}, is largely due an error known as vibro-pendulosity. A measurement bias results when a load is put on the pendulum axis and the sensitive axis at the same time. The other cross-coupling terms can be due to a load applied to the hinge axis or the pendulum axis within the accelerometer causing the pendulum axis to not be normal to the output axis.[80] An example of vibration rectification from an LN200 IMU mounted on the robotic lander Warm Gas Test Article (WGTA) is shown in Figure 3.4. Behind the legend, it can barely be seen that the signals show a bias shift after the vibration subsides. This is in addition to the large error during the vibration event which would be integrated into large velocity errors.

For ring laser gyros, little information is available in the literature to support the need for the higher-order scale factors. Savage alludes that some zero-lock mitigation techniques may produce non-linearities in the gyro measurements.[73]

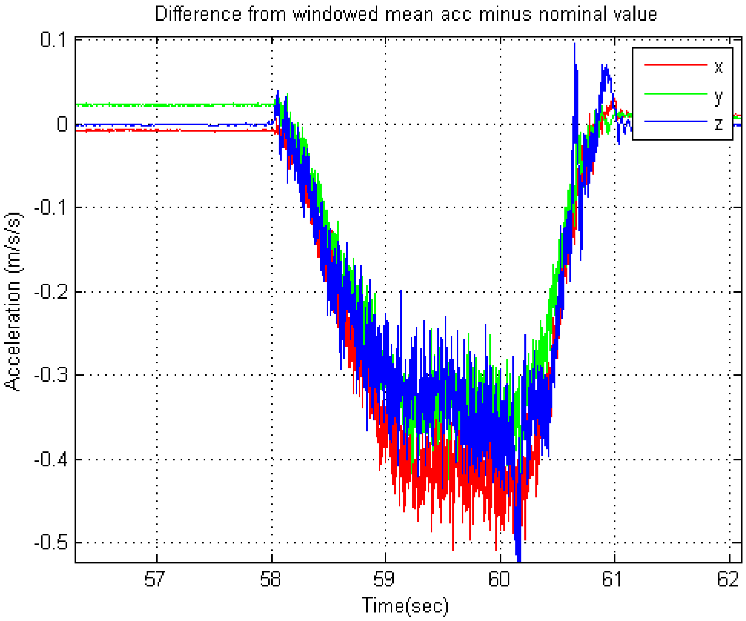

Figure 3.4

Warm Gas Test Bed, Vibration Rectification from IMU

$$\delta\vec{\omega}_{K_{Other}} = Diag_{(3\times3)}\begin{bmatrix}\omega_x^2\\ \omega_y^2\\ \omega_z^2\end{bmatrix}\sigma_{K2}^{gyro} + Diag_{(3\times3)}\begin{bmatrix}\omega_x^3\\ \omega_y^3\\ \omega_z^3\end{bmatrix}\sigma_{K3}^{gyro} \tag{3.14}$$
$$+Diag_{(3\times3)}\begin{bmatrix}\omega_y\omega_z\\ \omega_x\omega_z\\ \omega_y\omega_x\end{bmatrix}\left(\sigma_{K_{ip}}^{gyo} + \sigma_{K_{io}}^{gyro} + \sigma_{K_{op}}^{gyro}\right)$$

The previous Figure 3.3 also depicts a scale factor asymmetry error. Assymetry is the tendency of an instrument to scale differently on either side of a compensated zero input. Although, this is not a commonly specified error for ring laser gyros, it is more common for accelerometers. The mathematical model for scale factor asymmetry error is represented by Equation (3.15)

$$\delta Output_{Assymetry} = \frac{1}{2} \cdot \|Input\| \tag{3.15}$$

The accelerometer equivalent of this error is given by Equation (3.16) and the version for the gyro is given by Equation (3.17).

$$\vec{\delta a}_{K_{Asy}} = \frac{1}{2} Diag_{(3\times3)} \begin{bmatrix} |a_x| \\ |a_y| \\ |a_z| \end{bmatrix} \sigma_{Asy}^{accelerometer} \tag{3.16}$$

$$\vec{\delta\omega}_{K_{Asy}} = \frac{1}{2} Diag_{(3\times3)} \begin{bmatrix} |\omega_x| \\ |\omega_y| \\ |\omega_z| \end{bmatrix} \sigma_{Asy}^{gyro} \tag{3.17}$$

Next, instrument noise is one of the more dominant error terms with regard to its effect on navigation error for an inertial navigation system. According to Gelb, the random walk process is named for an analogy of a man who takes fixed length steps in random directions. For the gyros, this error is commonly termed angular random walk. For the accelerometer term, it will be termed accelerometer random walk or accelerometer white noise for this paper, although velocity random walk would be more accurate terminology. The white noise errors, by definition, are Gaussian. The model is taken from Rogers and Gelb.[68][18]. Figure 3.5 depicts the simulated error due to angular random walk for a compensated gyro. In the plot, the gyro is rotated 360 degrees at a constant rate of 60 degrees per second. The output does not include bias or scale factor errors.

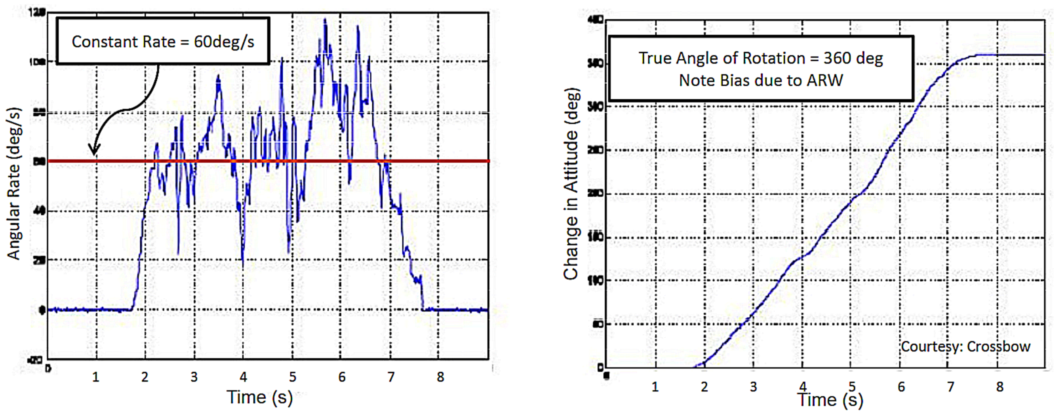

Figure 3.5

Example of Angular Random Walk

Gyro random walk is modeled as a white noise on the angular velocity that in integrated to become a random walk on the attitude. For this reason, Gyro specifications typically include an angular random walk error specification which is directly applicable to angle measurements while accelerometers will specify a white noise. For accelerometers, this white noise is integrated to become a random walk with respect to velocity.[52][76]

Random walk in general can be implemented into a time domain simulation as a time varying bias. From Rogers, if we consider the stochastic differential equation of motion,

$$dx(t) = \mathbf{A}(t)x(t) + d\mu(t)$$

Where $d\mu(t)$ is a Brownian motion process, from particle physics, representing random indepentent increments in time with the properties of zero mean, continuous, and normally distributed. Looking at random walk only, the correlated term $\mathbf{A}(t)$ is zero in the above expression. The state and the random process are uncorrelated. The covariance of the

Brownian, $d\mu(t)$, is defined as the expected value $E[d\mu(t)d\mu(t)^T]$. Given that the process is uncorrelated and normal, the following approximation can be made.[68]

$$E[d\mu(t)d\mu(t)^T] \approx (E[du(t)du(t)^T]dt)^2$$

$$dx(t) = d\mu(t) \approx u(t)\sqrt{dt} = \sigma\bar{u}(t)\sqrt{dt}$$

$$\frac{dx}{dt} = \sigma\bar{u}(t)\frac{1}{\sqrt{dt}}$$

The resultant expression is written as a function of a time dependant Gaussian draw, $\bar{u}(t)$, with unity variance and the error standard deviations so that it can easily be incorporated into a discrete model. Equations (3.18) and (3.19) describe the implementation of the angular random walk error as a function of step size or sampling rate and frequency for both acceleration and delta-angular rate, respectively.

$$\delta a_{RW}(t) = \sigma_{RW}^{accelerometer}\bar{u}(t)\frac{1}{\sqrt{dt}} = \sigma_{RW}^{accelerometer}\bar{u}(t)\sqrt{f} \tag{3.18}$$

$$\delta\theta_{RW}(t) = \sigma_{RW}^{gyro}\bar{u}(t)\sqrt{dt} = \sigma_{RW}^{gyro}\bar{u}(t)\frac{1}{\sqrt{f}} \tag{3.19}$$

Readout noise, or output noise, is another error term that is sometimes specified. The readout noise is applied similarly to the random walk except that the white noise is applied to output measurements, i.e. $\Delta\theta$ and ΔV.

Errors due to instrument misalignments and non-orthogonalities are also included in the general error model. The errors can be split into two major categories: misalignment relative to the sensor reference and misalignments relative to of the vehicle body frame. The difference is subtle but very important. The discerning detail differentiating the two categories is where they occur in the process with regard to the navigation function. For the purposes of this paper, the former are referred to as sensor misalignment errors and the latter as vehicle misalignment errors. The sensor misalignment errors are treated in this section due to their effect on the navigation solution. The vehicle misalignment errors are not integrated and do not contribute a cumulative error with time. This is discussed with more detail in Chapter 4.

The non-othogonality instrument error represents the error due to the misalignment of a single sensor axis with respect to the reference sensor frame. The model is taken from Malay, Galor, and Davis and is described for both accelerometers and gyros by Equations (3.20) and (3.21).[41] Small angles are assumed and the aggregate orthogonal misalignment error is assumed negligible.

$$\delta\vec{a}_{Non-Orthogonality} = \begin{vmatrix} 0 & \sigma_{xz} & -\sigma_{xy} \\ -\sigma_{yz} & 0 & \sigma_{yx} \\ \sigma_{zy} & -\sigma_{zx} & 0 \end{vmatrix} \vec{a}_{true}^{Sensor} \tag{3.20}$$

$$\delta\vec{\omega}_{Non-Orthogonality} = \begin{vmatrix} 0 & \sigma_{xz} & -\sigma_{xy} \\ -\sigma_{yz} & 0 & \sigma_{yx} \\ \sigma_{zy} & -\sigma_{zx} & 0 \end{vmatrix} \vec{\omega}_{true}^{Sensor} \tag{3.21}$$

The σ values represent the standard deviations for a set of six Gaussian angular errors, ϕ_{IJ}, each representing the error along the nominal input axis, denoted by the subscript I, when rotated about nominal axis J.

Given an error specification where misalignments and non-orthogonal misalignments are specified separately and vary in magnitude from the non-orthogonal misalignment, an additional set of models are included. Assuming the sensors are mounted on a mechanically isolated rigid structure, termed iso-block, these orthogonal misalignment models are applied common to the accelerometer and gyro model to account for iso-block misalignment with respect to sensor reference frame. An additional set is implemented for the gyro measurements only to account for gyro independent orthogonal misalignments. A third set is included for the accelerometer measurements only to account for accelerometer misalignments independent of the gyro output frame. The model is implemented for two different specification types using the Euler rotation theorem with small angle approximations, Equation (3.22), and with a direction cosine approximate analogous to the non-orthogonality model, Equation (3.23).

$$\vec{\delta m}_{Misalignment} = \begin{vmatrix} 0 & e_3\theta & -e_2\theta \\ -e_3\theta & 0 & e_1\theta \\ e_2\theta & -e_1\theta & 0 \end{vmatrix} \vec{m}_{true}^{Sensor} = \begin{vmatrix} (e_3 m_y - e_2 m_z)\theta \\ (e_1 m_z - e_3 m_x)\theta \\ (e_2 m_x - e_1 m_y)\theta \end{vmatrix} \tag{3.22}$$

In Equation (3.22), the Euler axis $\hat{e} = [e_1; e_2; e_3]$ is randomly derrived from a series of 3 draws. Particuliar care must be excercised in the development of this unit vector to insure the desired distribution within the 3-dimensional space. Equation (3.23) is a second mislignment option. In the equation, the misalignments are specified in terms of sigmas on three angles. The angle, θ_i, is the product of a random draw and the standard deviation of the angle dispersion, $\bar{u}\sigma_{\theta_i}$. Both models were made available and used for various misalignment specifications.

$$\delta\vec{m}_{Misalignment} = \begin{vmatrix} 0 & \theta_3 & -\theta_2 \\ -\theta_3 & 0 & \theta_1 \\ \theta_2 & -\theta_1 & 0 \end{vmatrix} \vec{m}_{true}^{Sensor} = \begin{vmatrix} \theta_3 m_y - \theta_2 m_z \\ \theta_1 m_z - \theta_3 m_x \\ \theta_2 m_x - \theta_1 m_y \end{vmatrix} \quad (3.23)$$

Other error terms included in the model are aniso-elasticity, sizing effects, and aniso-inertia. Aniso-elesticity is the error generated by the flexure of the sensor under load. Aniso-inertia is an error due to the finite mass and moments of inertia associated with the sensor. Uncompensated size-effect is an error due to the uncertainty of the distance between the individual sensors to the origin of the sensor frame. These errors are instrument specific and less commonly used. Therefore, they are not explained in further detail within this paper.

3.4 Navigation Software

This section will discuss the components of the navigation software. Inertial navigation algorithms are defined for calculating navigated position and velocity from total acceleration and for calculating attitude from angular rate through integration. The equations are formulated for a strapdown INS containing an orthogonal triad of accelerometers and co-aligned gyros. The INS is also assumed to have a precision clock for timing. The continuous inertial navigation solution is first defined followed by considerations for a practical discrete implementation.

This section will also detail the initial alignment process known as gyrocompassing. Gyrocompassing is presented as consisting of two elements. The first is the coarse alignment algorithm. The coarse alignment algorithm is responsible for developing an initial guess at the attitude of the sensor frame with respect to the navigation frame. The second element is the fine alignment algorithm. The fine alignment algorithm is a slower estimation process during which the initial attitude is estimated in the presence of errors and twist and sway dynamics.

Also discussed is a simplistic algorithm for integrating GPS measurements into an inertial navigation system. Chapter 4 will discuss the effect of the integration from a performance point of view. Note that the algorithms presented are of a fidelity for analysis and may or may not be suitable or ideal for implementation in flight software.

3.4.1 Quaternions

A quaternion formulation for attitude is favored due to its simplicity, closed form integration solution, improved accuracy over traditional methods, and for not having to treat singularities associated with euler angles. Although different conventions are used for the closed-loop and open-loop simulations, for the sake of this work the convention used is defined by Equation (3.24). Note that the convention is right handed with the scalar term occupying the first element. It is common to chose either the first or fourth element to represent scalar term of the quaternion. Other conventions exist, and although somewhat arbitrary, the quaternion operation equations may be specific to the convention.

$$q_{a1}^{a2} = \begin{bmatrix} Q_0 & Q_1 & Q_2 & Q_3 \end{bmatrix}^T = Q_0 + \hat{i}Q_1 + \hat{j}Q_2 + \hat{k}Q_3 \tag{3.24}$$

The quantity Q_0 is the scalar term. The transfomation from quaternion to Direction Cosine Matrix is included as Equation (3.25).

$$q_{a1}^{a2} \equiv C_{a1}^{a2} = \begin{vmatrix} Q_0^2 + Q_1^2 - Q_2^2 - Q_3^2 & 2(Q_1Q_2 - Q_0Q_3) & 2(Q_0Q_2 + Q_1Q_3) \\ 2(Q_1Q_2 + Q_0Q_3) & Q_0^2 - Q_1^2 + Q_2^2 - Q_3^2 & 2(Q_2Q_3 - Q_0Q_1) \\ 2(Q_1Q_3 - Q_0Q_2) & 2(Q_0Q_1 + Q_2Q_3) & Q_0^2 - Q_1^2 - Q_2^2 + Q_3^2 \end{vmatrix} \tag{3.25}$$

This form of the conversion does not require that the condition ($Q_0^2 + Q_1^2 + Q_2^2 + Q_3^2 = 1$) be satisfied. Quaternion multiplication and transformations are defined by Equation (3.26), denoted by the "$\circ$" operator, and Equation (3.27).

$$q_{a1}^{a2} \circ \vec{r} = q_{a1}^{a2} \vec{r} q_{a1}^{a2*} = \begin{bmatrix} Q_0 \\ Q_1 \\ Q_2 \\ Q_3 \end{bmatrix} \begin{bmatrix} 0 \\ r_i \\ r_j \\ r_k \end{bmatrix} \begin{bmatrix} Q_0 \\ -Q_1 \\ -Q_2 \\ -Q_3 \end{bmatrix} \tag{3.26}$$

Where q^* is the quaternion conjugate, ($Q_0 - \hat{i}Q_1 - \hat{j}Q_2 - \hat{k}Q_3$). For a quaternion product, the complex representation of the left quaternion can be used to decompose the quaternion into a 4x4 element matrix for multiplication.

$$q_{a1}^{a3} = q_{a2}^{a3} \cdot q_{a1}^{a2} = \begin{vmatrix} Q_0 & Q_1 & Q_2 & Q_3 \\ -Q_2 & Q_0 & -Q_3 & Q_2 \\ -Q_2 & Q_3 & Q_0 & -Q_1 \\ -Q_3 & -Q_2 & Q_1 & Q_0 \end{vmatrix} \cdot q_{a1}^{a3} \tag{3.27}$$

Quaternions are used in combination with direction cosine matrices and Euler angles whenever appropriate or convenient in the inertial navigation equations.

3.4.2 Inertial Navigation

The inertial navigation equations of motion for a strapdown inertial navigation system are described in this section. Unlike a gimballed navigation system, the strapdown system mathematically tracks attitude of the sensor platform with respect to the navigation frame. The sensor frame is denoted as the S frame, the navigation frame is denoted as the N frame and the inertial frame is denoted the I frame. The general differential equation for the change in attitude with respect to time is given by Equation (3.28).

$$\dot{q}_S^N = \frac{1}{2} q_S^N \begin{bmatrix} 0 \\ \\ \vec{\omega}_{I,S}^S \end{bmatrix} - \frac{1}{2} \begin{bmatrix} 0 \\ \\ \vec{\omega}_{I,N}^N \end{bmatrix} q_S^N \tag{3.28}$$

For the purposes of analysis, the navigation equations are implemented in the non-rotating inertial frame. This results in some simplicity in the navigation equations in exchange for some complexity in producing state data in other coordinate frames when needed. The velocity and position differential equations of motion relative to the inertial frame are given by Equations 3.30 and 3.29.

$$\dot{\vec{V}}_I = q_S^I \circ \vec{f}_S + \vec{g}_I \tag{3.29}$$

$$\dot{\vec{R}}_I = \vec{V}_I \tag{3.30}$$

The velocity in the inertial frame is denoted as $\vec{V}_I$ and the inertial position vector is $\vec{R}_I$. In the velocity differential equation, the specific force measurement from the accelerometers, $\vec{f}_S$, are summed with the gravity vector resolved in the inertial frame, $\vec{g}_I$, for the total acceleration.

The implemented gravity model includes J2, J3, and J4 harmonics. The J2, J3, and J4 harmonic gravity terms are not longitudinally dependent and can be directly implemented without transformation. The gravity model is given as Equation (3.31) with terms defined in Equations 3.33, 3.33, and 3.35.[2]

$$\vec{g}_I = \begin{bmatrix} g_x & g_y & g_z \end{bmatrix}^T \tag{3.31}$$

$$\begin{aligned} \vec{g}_x = -\frac{\mu R_x}{|R|^3}\Bigg[1 - J_2\frac{3}{2}\left(\frac{R_e}{|R|}\right)^2 \left(5\frac{R_z^2}{|R|^2} - 1\right) \\ \ldots + J_3\frac{5}{2}\left(\frac{R_e}{|R|}\right)^3 \left(3\frac{R_z}{|R|} - 7\frac{R_z^3}{|R^3|}\right) \\ \ldots - J_4\frac{5}{8}\left(\frac{R_e}{|R|}\right)^4 \left(3 - 42\frac{R_e^2}{|R|^2} + 63\frac{R_z^4}{|R|^4}\right)\Bigg] \end{aligned} \tag{3.32}$$

$$\vec{g}_y = \frac{R_y}{R_x} g_x \tag{3.33}$$

$$\begin{aligned} \vec{g}_z = -\frac{\mu R_z}{|R|^3}\Bigg[1 - J_2\frac{3}{2}\left(\frac{R_e}{|R|}\right)^2 \left(3 - 5\frac{R_z^2}{|R|^2}\right) \\ \ldots + J_3\frac{3}{2}\left(\frac{R_e}{|R|}\right)^3 \left(10\frac{R_z}{|R|} - \frac{35}{3}\frac{R_z^3}{|R^3|} - \frac{|R|}{R_z}\right) \\ \ldots - J_4\frac{5}{8}\left(\frac{R_e}{|R|}\right)^4 \left(15 - 70\frac{R_e^2}{|R|^2} - 63\frac{R_z^4}{|R|^4}\right)\Bigg] \end{aligned} \tag{3.34}$$

The coefficients for the three zonal terms and the radius of the Earth, R_e, are taken from the GGM-02c Grace gravity model.[78]

The quaternion equation, Equation (3.28), is modified for coning compensation. The coning algorithm is derived from Savage.[71] The algorithm is second order and has been modified to accommodate a fixed sampling rate which is equivalent to attitude update rate. The algorithm implemented uses the current and previous $\delta\theta$ measurements to approximate the coning error compensation. For a discussion on coning, see Goodman and Robinson, McKern, or Bortz.[21][43][8] Alternative coning algorithms exist in the literature. The algorithm implemented is discussed as Algorithm B by Ignagni.[29]

$$\alpha = \vec{\Delta\theta}_i = \omega_S \Delta t \tag{3.35}$$

$$\vec{\phi} = \frac{1}{2}\left(\Delta\vec{\theta}_i + \frac{1}{12}\Delta\vec{\theta}_{i-1} \times \Delta\vec{\theta}_i\right) \tag{3.36}$$

$$\Delta q = \begin{bmatrix} \cos\left(|\vec{\phi}|\right) \\ \frac{[\vec{\phi}]_x}{|\vec{\phi}|}\sin\left(|\vec{\phi}|\right) \\ \frac{[\vec{\phi}]_y}{|\vec{\phi}|}\sin\left(|\vec{\phi}|\right) \\ \frac{[\vec{\phi}]_z}{|\vec{\phi}|}\sin\left(|\vec{\phi}|\right) \end{bmatrix} \tag{3.37}$$

Equation (3.35) represents the measurement which is summed at every sampling period over the navigation time step. The delta-attitude vector in Equation (3.36) represents the coning compensation over the last navigation execution cycle. The delta-quaternion in Equation (3.37) is the quaternion representation of the coning compensated change in attitude. In Equation (3.38), the coning compensation is applied to the attitude quaternion when it is integrated. The quaternion integration is performed with compensated delta-theta measurements directly. A delta-quaternion is formulated with the compensated measurements, $\Delta\phi$. The delta-quaternion represents the angular change in attitude over the time interval defined by the navigation execution frequency. The quaternion product of the previous attitude solution and the delta-quaternion for the current iteration comprises the updated attitude quaternion. The quaternion should be periodically normalized. In simulation, this is unnecessarily done at every time step. Performing the normalization at a lower rate would be acceptable.

$$\left[q_S^N\right]_i = \left[q_S^N\right]_{i-1} \circ \begin{bmatrix} \cos\left(|\vec{\phi}|\right) \\ \frac{[\vec{\phi}]_x}{|\vec{\phi}|}\sin\left(|\vec{\phi}|\right) \\ \frac{[\vec{\phi}]_y}{|\vec{\phi}|}\sin\left(|\vec{\phi}|\right) \\ \frac{[\vec{\phi}]_z}{|\vec{\phi}|}\sin\left(|\vec{\phi}|\right) \end{bmatrix} \tag{3.38}$$

For the integration of the velocity and position differential equations, Equations 3.29 and 3.30, the trapezoidal integration method is used with sufficient accuracy. Equation (3.39) gives the general equation for the second order trapezoidal integration method.

$$\vec{x}_{t+\Delta t} = \vec{x}_t + \frac{\Delta t}{2}\left(\dot{\vec{x}}_t + \dot{\vec{x}}_{t+\Delta t}\right) \tag{3.39}$$

Sculling compensation was not applied in the velocity integration algorithm. Sculling compensation can be implemented in the integration of the accelerometer measurements, similar to the implementation of coning compensation.[69] Previous analysis showed a lack of improvement in the solution within the context of the analysis so it has been omitted here.

3.4.3 Gyrocompassing, Coarse Alignment

The gyrocompassing process consists of two algorithms. The first is a coarse alignment algorithm. The coarse alignment algorithm is a deterministic algorithm for computing the initial attitude. If there were no noise on the sensor measurements or from the dynamics, the coarse alignment algorithm would alone be sufficient for determining the initial alignment of the INS. Unfortunately, the sensor measurements do contain noise and the vehicle will twist and sway on the pad. To reduce some of the noise on the measurement, the delta velocity measurements and delta attitude, or delta θ, measurements are summed over a user defined period of time, Equations 3.40 and 3.41. The measurements are inherently relative to the sensor frame. Assuming a fixed sampling rate, the variable N is the number of samples, i, corresponding to the time allocated to coarse alignment.

$$(\delta\vec{V}_s)_{sum} = \sum_{i=1}^{N} \Delta\vec{V}_s(t_i) \tag{3.40}$$

$$(\delta\vec{\theta}_s)_{sum} = \sum_{i=1}^{N} \Delta\vec{\theta}_s(t_i) \tag{3.41}$$

First, the direction along the gravity vector, $\hat{z}$, is determined from the accelerometer measurement in Equation (3.42). On the ground, the accelerometers should measure 1g in the up direction due to Earth's gravity.

$$\hat{z} = -\frac{(\delta V_s)_{sum}}{|(\delta V_s)_{sum}|} \tag{3.42}$$

The Northward direction is then computed, Equation (3.43), from the down direction and the summed $\Delta\theta$ measurements.

$$\hat{y} = \frac{\hat{z} \times (\delta\vec{\theta}_s)_{sum}}{|(\delta\vec{\theta}_s)_{sum}|} \tag{3.43}$$

The Eastward direction completes the right handed orthogonal triad, Equation (3.44). The computed unit vectors are the basis for the North, East, Down (NED) local-level coordinate frame. The transformation from the NED frame to the Sensor frame is then defined from the computed unit vectors, Equation (3.45)

$$\hat{x} = \hat{y} \times \hat{z} \tag{3.44}$$

$$C^{S}_{NED} = \begin{bmatrix} \hat{x} & \hat{y} & \hat{z} \end{bmatrix} \tag{3.45}$$

If the fine alignment algorithm is defined relative to the NED frame, then this is the initial alignment attitude update. To relate the new frame to the Earth Center, Earth Fixed (ECEF) frame, the latitude and longitude are computed with Equations 3.46, 3.47, and 3.48. Prior to alignment, the position vector, R_{ECI} is erroneous but represents the navigator knowledge of position. R_m is the mean equatorial radius of the Earth, ϵ is the eccentricity of the Earth, and R_p is the polar radius of the Earth.

$$\Theta = \tan^{-1}\left(\frac{[R_{ECI}]_z R_m}{\sqrt{[R_{ECI}]_x^2 + [R_{ECI}]_y^2} R_p}\right) \tag{3.46}$$

$$\lambda = \tan^{-1}\left(\frac{[R_{ECI}]_z + \epsilon^2 R_p \sin^3(\Theta)}{\sqrt{[R_{ECI}]_x^2 + [R_{ECI}]_y^2} - \epsilon^2 R_m \cos^3(\Theta)}\right) \tag{3.47}$$

$$L = \tan^{-1}\left(\frac{[R_{ECI}]_y}{[R_{ECI}]_x}\right) \tag{3.48}$$

The ECEF frame to NED frame transformation is then computed.

$$C^{NED}_{ECEF} = \begin{bmatrix} -\sin\lambda\cos L & -\sin\lambda\sin L & \cos\lambda \\ -\sin L & \cos L & 0 \\ -\cos\lambda\cos L & -\cos\lambda\sin L & -sin\lambda \end{bmatrix} \tag{3.49}$$

The transformation from the sensor frame to ECEF frame is computed with Equation (3.50). If the fine alignment algorithm is defined in the ECEF frame, then this is the initial alignment attitude update.

$$C^{ECEF}_{S} = C^{ECEF}_{NED} C^{NED}_{S} \tag{3.50}$$

If the fine alignment algorithm is defined in the ECI frame, then the navigators current knowledge of attitude can be used to approximate the ECEF frame to ECI frame transformation, Equation (3.51)

$$C_{ECEF}^{ECI} = C_S^{ECI}(C_S^{ECEF})^T \tag{3.51}$$

The attitude update is made by taking the quaternion version of the direction cosine matrix and applying it to the current navigated attitude. Equation (3.52) assumes that the navigation frame is the ECI frame. The navigated velocity solution is updated by the expression in Equation (3.53). The position is assumed to be a parameter loaded into the navigator. The position should be reset to this value after the velocity update and before the transition to inertial navigation after the fine alignment algorithm.

$$q_{ECI}^{S} = q^{update} \circ q_{ECI}^{S} \tag{3.52}$$

$$\vec{V}_N = \vec{V}_N + \Omega_E \times \vec{R}_{ECI} - \vec{V}_N \tag{3.53}$$

If the residual error is not within the fine alignment filter expectation, then either adjust the length of time that the coarse alignment algorithm runs or adjust the expectation of the filter by modifying the initial covariance.

3.4.4 Gyrocompassing, Fine Alignment

The fine alignment filter is an extended Kalman filter which takes zero velocity updates. That means that the filter measurement is consistent with the knowledge that the vehicle is not moving. In a local level frame, this corresponds to a zero velocity. The Kalman filter is covered extensively in literature.[18][32][12] The Kalman filter equations consist of the error covariance propagation, Equation (3.54), the Kalman gain equation, Equation (3.55), the error covariance update equation, Equation (3.56), and the state estimate update, Equation (3.57).

$$P^- = \Phi P^+ \Phi^T + Q(t)\Delta t \tag{3.54}$$

$$K = PH^T(HP^-H^T + R)^{-1} \tag{3.55}$$

$$P^+ = (I - KH)P^- \tag{3.56}$$

$$\hat{x} = K(y - h(x)) \tag{3.57}$$

In the Kalman filter equations, P is the error state covariance, K is the Kalman gain, Δt is the time between measurements, R is the measurement noise, H is the observation matrix and, t is the time since the start of the filter. The filter used for analysis is a simple six state filter consisting of the error in navigated velocity and the error in attitude, defined by Equation (3.58).

$$x = \begin{bmatrix} \vec{V}_{Nav} \\ \vec{\Theta}_{Nav} \end{bmatrix} \tag{3.58}$$

The state transition matrix, Φ, is recomputed at every time step from the state dynamics matrix, F, Equation (3.59). It is assumed that $\dot{x} = f(x)$. The quantity $\vec{a}_S$ is the specific force measurement expressed in the sensor frame. The state transition matrix is computed from F by Taylor series expansion. The formulation is given in Equation (3.60)

$$F = \frac{\partial f(x)}{\partial x} = \begin{bmatrix} 0 & \Delta t[\times(T_S^{Nav}\vec{a}_S)] \\ 0 & 0 \end{bmatrix} \tag{3.59}$$

$$\Phi = (I + F\Delta t + \frac{1}{2}F^2\Delta t + \frac{1}{6}F^3\Delta t^2) \tag{3.60}$$

The process noise covariance, Q, is chosen to represent the accelerometer random walk and the gravity anomaly in velocity. The attitude portion of Q is chosen to represent the gyro random walk, gyro bias, and a small quantization noise. The process noise covariance is a function of the time since the start of the filter to accommodate the gyro bias component. The measurement noise is chosen consistent with the expected twist and sway environment.

In Equation (3.57), the measurement y is the zero velocity measurement. In Equation (3.61) the measurement is defined as a function of the measurement matrix and Equation (3.62) defines the zero velocity measurement, y, for the ECI frame.

$$y = Hx = \begin{bmatrix} 1 & 0 & 0 & 0 & 0 & 0 \\ 0 & 1 & 0 & 0 & 0 & 0 \\ 0 & 0 & 1 & 0 & 0 & 0 \end{bmatrix} x \tag{3.61}$$

$$y = \Omega_E \times T_{ECEF}^{ECI} R_0 \tag{3.62}$$

The initial position, R_0, is supplied as part of the navigation system initialization. In the state estimate equation, Equation (3.57), $h(x)$ is the navigated velocity. The velocity error estimate is summed with the navigated velocity as part of the update. The attitude is developed into a quaternion. The updated attitude is the quaternion product of the attitude update and the navigated attitude. It is consistent with the coarse alignment update, Equation (3.52). The filter nominally produces updates at 1Hz.

3.4.5 GPS Aiding

The GPS aiding filter is an extended Kalman filter with the same general implementation as the gyrocompassing filter. For taking GPS measurements, the state has been expanded to include position, Equation (3.63). The F matrix is given by Equation (3.64).

$$x = \begin{bmatrix} \vec{P}_{Nav} \\ \vec{V}_{Nav} \\ \vec{\Theta}_{Nav} \end{bmatrix} \tag{3.63}$$

$$F = \begin{bmatrix} 0 & I & 0 \\ \frac{\partial G}{\partial \vec{P}_{Nav}} & 0 & \Delta t[\times(T_S^{Nav} A_S)] \\ 0 & 0 & 0 \end{bmatrix} \tag{3.64}$$

The initial covariance is chose to be consistent with the expectation for the errors in the GPS position and velocity. The attitude component is chosen to be consistent the attitude errors after gyrocompassing. The process noise for the attitude component is chosen in the same way as for the gyrocompassing filter. The measurement noise is sized according to the GPS error. The filter nominally produces an update at 1Hz. The ability to start and stop filter updates at anytime is configurable.

3.5 The System Error Model and Output Interface

The system error model consists of the non-sensor errors plus the processing required to emulate the function of the INS. This section discusses quantization error, system precision, timing errors, output measurement filtering, latency, data buffering, and the output state definition.

3.5.1 Quantization

The error terms covered to this point comprise the stochastic error model; however, there are other sources of error which must also be included in the model. The first is a process denoted quantization and has been at times included in both the stochastic error model and the electronics and hardware error model. Quantization is not well treated in the reviewed literature. The quantization model affects the corrupted measurement and was originally meant to model the electronic error due to analog to digital conversion; however, since ring laser gyros are inherently digital, the model definition was expanded to include the sampling process associated with the ring laser gyro measurement. The physical phenomena may differ slightly between the accelerometer and gyro, but the mathematical representation covers both. The quantization model implementation is identical for accelerometers and gyros. For quantization, measurements are converted from their respective units to least significant bits (LSBs). Truncation occurs. The delta thetas and delta velocities are then converted back into their respective units from LSBs. The residual is held over for the next iteration. Savage states that "‘Although generally not considered a major contributor to system inaccuracy, inertial sensor quantization error, if not properly modeled, can lead to erroneously large estimates of its impact on inertial navigation system performance.’" [72] Maintaining the residual is the key component for the modeling of both the accelerometers with anolog output sampled at extremely high rates and the gyros with the digital fringe counting process associated with ring laser gyros. The model for an arbitrary measurement, m, is summarized by the logic in Equation (3.65).

$$\xi = \mathbf{floor}\left(\frac{m_i^{Input}}{ScaleFactor} + residual_{i-1}\right) \cdot ScaleFactor$$

$$m_i^{Output} = \begin{cases} \xi; & \text{if } \left|\frac{\xi}{ScaleFactor}\right| \leq \epsilon; \\ 0; & \text{if } \left|\frac{\xi}{ScaleFactor}\right| > \epsilon. \end{cases} \tag{3.65}$$

$$residual_i = \frac{m_i^{Output} - m_i^{Input}}{ScaleFactor} + residual_{i-1}$$

For the logic outlined in Equation (3.65), the $ScaleFactor$ is the least significant bit, count, or quanta in engineering units and ϵ represents a gating threshold, e.g. maximum number of bits or number of counts. Given the specification, this model could also be configured to saturate once the threshold, ϵ, had been exceeded such that the measurement would be equal to $(\epsilon \cdot ScaleFactor)$ as opposed to zero. Both cases represent situations to avoid.

In addition to the model presented by Equation (3.65), the process can be modeled as a uniform noise on the sensor output if a linear model is needed. For error linear state dynamics modeling, the process can be approximated as a white noise with variance $(q^2/12)$, where q is a single count in engineering units. [72].

Another point of concern for quantization is how it is specified and the possibility of modeling the error incorrectly due to frequency dependence on the specification. Take an example of a ring laser gyro with a quantization specification of 1.0 deg/s. Since a ring laser gyro does not inherently measure angular rate but rather angular displacement the specification with respect to angular rate is ambiguous. In order to properly model this error, the sampling rate at which the measurement is quantized must also be known in order to properly model the error. If the specification of 1.0 deg/s is inherently sampled at 1kHz, the effective quantization on the delta angle would be 0.001 deg. Incorrectly modeling the quantization at 50Hz would result in a quantization on the delta angle of 0.02 degrees. For the same reason, properly downsampling the measurement can act to reduce the effective quantization error on the angular rate.

3.5.2 System Precision

Another model component, possibly somewhat unique to Ares and SLS due to the avionics architecture, was introduced to simulate a precision limiting process between the INS and the flight computer. The heritage INS was designed to be an all-in-one INS plus flight computer. On the heritage program, the GN&C and Mission Manager code is executed on computational assets within the INS. The external interfaces were designed for telemetry from the box. For Ares, this interface was modified for data transfer to the flight computer which executes guidance, control, mission manager, and limited navigation functions. As a result, the precision of the external interface was originally limited to what was previously used for telemetry as opposed to what would be used for flight software. Further constraining the output was an older floating point data type specification which differs from the common IEEE-754 specification. In an effort to accurately simulate the interfaces and identify necessary changes that needed to be made, a model was introduced to simulate the precision limiting process. This model, termed the precision model, was added to simulate the unique truncation to the content of the navigation state message and instrument messages which occurred in transforming between the different data types from different standards. The truncation is simulated by the described algorithm.

The size of the mantissa of the simulated data type is defined numerically such that the variable A_m is equal to the minimum number that could be stored in the mantissa and the variable B_m is set to the maximum value. In a similar manner, the range for the exponent is defined by the variables A_e and B_e;

$$A_m = -\frac{1}{2}\left(2^{N_{mantissa}}\right) - 1$$
$$B_m = \frac{1}{2}\left(2^{N_{mantissa}}\right)$$

A two's compliment system is assumed. The mantissa is either positive or negative based on the value of the most significant bit. Sometimes this bit is designated separately as a sign bit although the behavior can be different for a two's compliment system. The most significant bit is the mechanism which splits the range of numbers that can be represented as positive and negative numbers versus only indicating a negative directly with a sign bit. The major implication of the system is with respect to truncation. This is particularly important for large numbers such as a position state vector referenced to the center of the Earth. For a two's compliment, the numbers will always be truncated towards negative infinity, while with a true sign bit the truncation may occur towards zero.

In simulation, simulated truncation occurs by determining the corresponding exponent and mantissa for a number based on the data type specification. The decomposition is performed iteratively by shifting the number by 2 until the number fills the mantissa or until the exponent exceeds the specified maximum. The algorithm requires separate logic for different number ranges termed Normal and Sub-Normal, defined by the inequalities in Equation (3.66) for an input f.

$$\begin{aligned} \mathrm{Normal:} \quad \mathrm{if} \quad (f > B_m) \quad || \quad (f < A_m) \\ \mathrm{Sub-Normal:} \quad \mathrm{if} \quad (A_m \leq f \leq B_m) \end{aligned} \tag{3.66}$$

For a Normal ranged number, the number is iteratively shifted to the right by dividing by 2 while Normal and while the exponent has not reached maximum. The exponent is incremented for each shift. For a Sub-Normal number, the number is shifted left by multiplying by 2 until no longer Sub-Normal or the exponent has reached minimum. The exponent is decremented for each iteration. The mantissa is then computed by truncating the absolute value of the new number at zero. The result containing the error is then computed by applying the sign to the mantissa and shifting iteratively by the signed exponent.

The data types that were available are described by the MIL-STD-1750a specification. The Ares I flight computer used an IEEE 754 standard. By using the bit values in Figure 3.6, the available floating point data types were simulated.[81]

This model ensures appropriate truncation at the bit level and is preferred over a more traditional model which truncates at a decimal place or for a constant multiple of some specified value. Preference is given due to the large variation in the states used from the INS and the reality that the least significant bit represents a different value dependent upon the size of the number being represented, through the exponent. In most cases, such a specific truncation model is not required, but due to the unexpected limitation in precision it became important to ensure that adequate precision was available in rate measurements

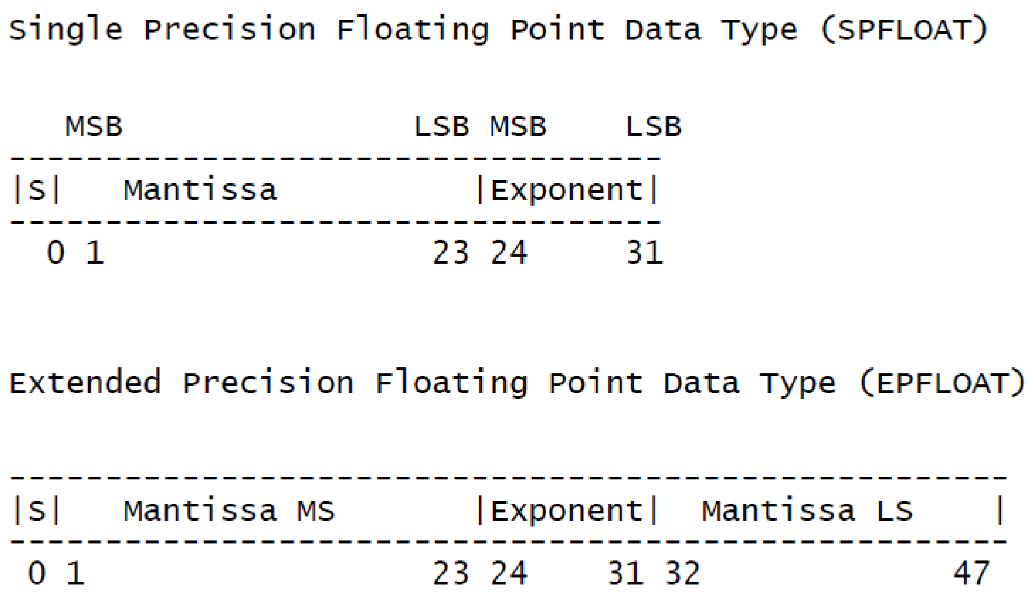

```
Single Precision Floating Point Data Type (SPFLOAT)

   MSB               LSB MSB   LSB
----------------------------------
|S|   Mantissa        |Exponent|
----------------------------------
  0 1                0 23 24     31

Extended Precision Floating Point Data Type (EPFLOAT)

----------------------------------------------------
|S|   Mantissa MS     |Exponent|  Mantissa LS     |
----------------------------------------------------
 0 1                 23 24    31 32            47
```

Figure 3.6

MIL-STD-1750a Floating Point Data Type Definition

such that transients were not unexpectedly introduced into the controller. This is especially critical for position at lift off for tower clearance maneuvers, and for position as compared to the discretization of the Chi tables for the first stage open-loop guidance algorithm. The result of studying the effect of the model led to a change in requirements for the precision given to the position state and avoided the expense associated with changing more of the heritage INS flight software than necessary.

In a C++ programming environment, this model could be extended to a method for a numeric class. This would allow for the effect of the numeric precision to be seen on the navigation algorithms as opposed to only on the output interface. This type of implementation would validate the assumption that numbers represented with 40 bit mantissas contribute negligible error to the navigation solution.

3.5.3 Time Errors

Another source of error included in the general error model but included as electronic error is a source related to the ability to keep accurate time. The instruments are referenced to a clock with a fixed frequency for sampling, the measurements are time stamped, and the measurements are integrated for a navigation state. Deviations in the time reference at any point will introduce a time dependent error. The following model, Equation (3.67), was introduced to model such errors for an arbitrary input, m_{Input}.

$$\vec{m}_{Output}(t) = \vec{m}_{Input}(t) \cdot \frac{dt}{dt + \tau_{bias} + t \cdot \tau_{drift} + \tau_{jitter}(t)} \tag{3.67}$$

This model affects an accelerometer measurement or gyro measurement by adding an error to the signal in a manner consistent with the error in time. The timing model contains a bias term, τ_{bias}, a first order term, τ_{drift}, and a time variant random component, $\tau_{jitter}(t)$. The implementation of the random component is modeled as a uniform noise scaled for a specified range. Equation (3.67) represents a convenient way to model timing errors as it allows for the discrete simulation of error due to timing without the limitation of the simulation step size. Depending upon the analysis being preformed, this model is implemented prior to the inertial navigation algorithms and on only the output rates without corrupting the time used to produce the measurements that are input to the inertial navigation algorithms. The reason for implementing the model after integration was due to a unique situation for Ares in which the INS was required to synchronize its time stamps to the time broadcast message across a MIL-STD-1553 bus for time stamping. The time message, originating with the flight computer, contained a clock with a higher drift and jitter than what would traditionally be used for navigation. The INS, on the other hand, contained a very accurate time source. Further error in the form of latency and jitter was introduced by the MIL-STD-1553 bus. Instead of using the synchronized time source for measurement scaling and navigation, the more accurate INS time source was used. The use of the less accurate synchronized time reference was limited to time stamps only. The errors introduced in the INS measurements, post integration, were modeled for subsequent use by the Guidance and Controls subsystems.

3.5.4 Anti-Aliasing

A component of the model which must be included in the closed-loop simulation is the frequency domain component. Transfer function logic is included outside of the input interface to allow for any filtering that is done within the INS. In addition to the dynamics on the front end of the sensor model, anti-aliasing filters were modeled as specified for the accelerometer and angular rate output used by the controller. This affect is not important in terms of assessing navigation performance, but properly capturing it is important for the integrated simulation.

Two implementations are included for implementation of a discrete filter within the INS data flow. The first is a simple discrete transfer model in which discrete filter coefficients can be specified up to fourth order. The second implementation is for a second order low pass filter derived as a function of the parameter for the continuous version of the filter. For Ares, this implementation was used to implement an anti-aliasing filter which was specified for implementation within the INS due to data rate limitations on the flight computer. The Ares anti-aliasing filter was a second order low-pass filter. The purpose of the filter was to remove any high frequency content within the gyro and accelerometer measurement channels which could potentially alias down to a frequency within the controller bandwidth. If aliasing occurred, it is possible that the vehicle would react to a perceived disturbance which did not exist. To avoid this, filtering of the measurement signals is performed at a high rate to remove spectral content above the controllers Nyquist frequency.

In simulation, the filter is implemented with an analytically derived digital second order low-pass filter. The continuous form of the filter is shown in Equation (3.68) as a function of the filter break frequency, ω and the filter damping constant, ζ.

$$\frac{Y(s)}{I(s)} = \frac{\omega^2}{s^2 + 2\zeta\omega + \omega^2} \tag{3.68}$$

Using mathematical tools in Python or Matlab, discrete transfer function coefficients could easily be generated for a specific analog filter design. The first implementation provided the capability to implement the anti-aliasing filter in this way. To simplify the process of changing the filter for analysis an analytical expression for the discrete representation was derived as a function of ω, ζ, and the sampling constant, T using the Tustin, or bilinear transform, described by Equation (3.69). As long as a higher order filter was not needed, this proved to be the most convenient approach.

$$TF_D(z) = TF_A(s)\Big|_{s=\frac{2}{T}\frac{z-1}{z+1}} = TF_A\left(\frac{2}{T}\frac{z-1}{z+1}\right) \tag{3.69}$$

The resultant analytical solution for the discrete second order low-pass filter is described by Equation (3.70). The input, y_i, represents the filter error for the current discrete time step, i, and the output, $\bar{y}_i$, represents the correction for discrete time step i.

$$\bar{y}_i = \frac{T^2\left[\omega_b^2(y_i + 2y_{i-1} + y_{i-2}) - (2\omega_b^2 - 8T^2)\bar{y}_{i-1} - \left(\frac{4}{T^2} - \frac{4\zeta\omega_b}{T} + \omega_b^2\right)\bar{y}_{i-2}\right]}{4(1 - \zeta\omega_b T)} \tag{3.70}$$

For Ares I, the controller executed at a 50Hz rate. It was important to protect the band below the associated Nyquist frequency of 25Hz while still preserving maximum bandwidth for controls design flexibility. For the current SLS design, the filter has been increased in order to a 4th order implementation to achieve adequate attenuation at the Nyquist frequency with minimal impact on phase.

The Control system is the user of the filtered rates. The filter is implemented after the navigation algorithms have executed. Filtering prior to navigation introduces error into the navigation solution.

3.5.5 Step Size Delays and Output Interface

The output for the INS model consists of the navigated position, velocity, and the sensor-to-navigation attitude quaternion. Filtered angular rate and specific force measurements as a function of the output frequency are produced in terms of integrated delta attitude angles and delta velocity relative to the sensor frame. Navigation quality delta attitude angles and delta velocity are also provided. These measurements are representative of the angular rate and specific force used in the inertial navigation algorithm. The measurements used in the inertial navigation algorithms will have been compensated for coning, sculling, temperature effects and size effects. The data is time stamped relative to the center of the sampling period over which the measurements were taken. A data quality indicator is provided to supply insight into the health of the INS to the flight computer model. The data is placed into an output structure for access by the flight computer model.

In cases where the measurement data is produced at a rate greater than the flight computer sampling rate, the data is buffered such that the flight computer can access all of the data since the last sample. The output interface model allows for latencies to be applied to the data individually. It is not uncommon to have low latency data used by flight controls versus a higher latency associated with the output of the navigation state. The model accomodates this by buffering the data in a holding structure which operates as a queue to the output structure. The latencies implemented in this module are limited to multiples of the INS model execution frequency.

CHAPTER 4

NAVIGATION SYSTEM SENSITIVITIES AND ANALYSIS

4.1 Monte Carlo Analysis and Sampling Error

There are predominantly two categories of methods for analyzing insertion accuracy error known to the author. The methods are covariance analysis and Monte Carlo analysis. The first category is covariance analysis or a variant thereof. For traditional covariance analysis, the state dynamics are linearized about a reference trajectory and an error covariance matrix is propagated to approximate the error covariance at some time later. There are many variants of covariance analysis which range in complexity. In the comparison of tools using Monte Carlo analysis and covariance analysis to approximate navigation error statistics, differences of 0.2% to 30% have been observed between these methods.[6][5][7][51][54][53] Further, real biases in the errors estimates due to non-linearities associated with the trajectory or the error models are not well represented in covariance analysis results. In the interest of getting to the the most reliable result quickly, the author of this paper switched to the second category of analysis, the Monte Carlo method, to estimate navigation errors. However, the development of a good non-linear covariance analysis tool is of great interest to the author.

In general, Monte Carlo analysis is defined as representing the solution of a problem as a parameter of a hypothetical population and using a random sequence of numbers to construct a sample of the population, from which statistical estimates of the parameter can be obtained. [23] Formulating the navigation system equations in terms of a function of random variables leads to an expression in terms of random variables ξ_n, χ_n, and ζ_n, Equation (4.1).

$$X = \begin{bmatrix} \Phi = f\left(\xi_1, \xi_2, \ldots, \xi_n\right) \\ V = g\left(f\left(\xi_1, \xi_2, \ldots, \xi_n\right), \chi_1, \chi_2, \ldots, \chi_n\right) \\ P = h\left(g\left(f\left(\xi_1, \xi_2, \ldots, \xi_n\right), \chi_1, \chi_2, \ldots, \chi_n\right), \zeta_1, \ldots, \zeta_n\right) \end{bmatrix} \tag{4.1}$$

For covariance analysis, the state expressions would need to be decomposed and expressed in terms of the error. The error dynamics, $(\dot{X} - \dot{X}^{Ref})$, would be linearized about the reference trajectory and expressed in terms of variational equations. Higher order terms would be truncated. By contrast, the ability to solve the problem by Monte Carlo does not depend on the stochastic nature of the system being studied, but only on our ability to formulate the problem in such a way that random numbers may be used to obtain the solution. [30] No approximation of the dynamics is required in Monte Carlo analysis.

In Monte Carlo analysis, an understanding of the statistical nature of the system may not be required, but an understanding of the statistics associated with the input parameters is important for proper dispersion. Further, an understanding of the output statistics is important for reporting purposes. The following histograms are of the output state from an arbitrary navigation error Monte Carlo analysis. For the analysis, 10,000 runs were made in an effort to understand the output statistics and assess sampling error. Figure 4.1 is a histogram for the three components of the position state at orbit insertion. Figure 4.2 and Figure 4.3 similarly show the velocity and attitude state distributions. In the histograms, bins containing solutions are plotted. The x-axis is the position error associated with a particular bin and the y-axis indicates the number of solutions. Note the recovery of the mean error in the distributions.

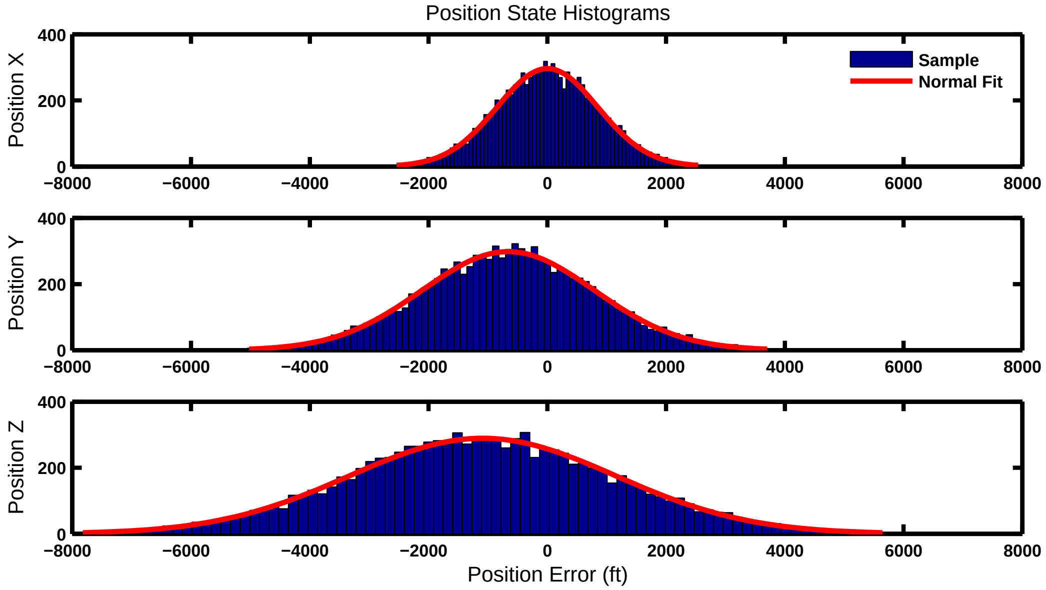

Figure 4.1

Large Sample Monte Carlo Histogram, Position

In each plot, the distribution has been fitted to a normal distribution, indicated by the red line, to visually assess the distribution of the output parameters. Understanding the probability density of the output allows for the proper reporting of the error statistics and the development of a model for determining the number of Monte Carlo runs required to minimize sampling error for accurate reporting of the error statistics. Hanson and Beard point out that, for a Monte Carlo analysis in general, there is no way to develop an apriori estimate for how many samples are required to generate an answer to a desired precision.

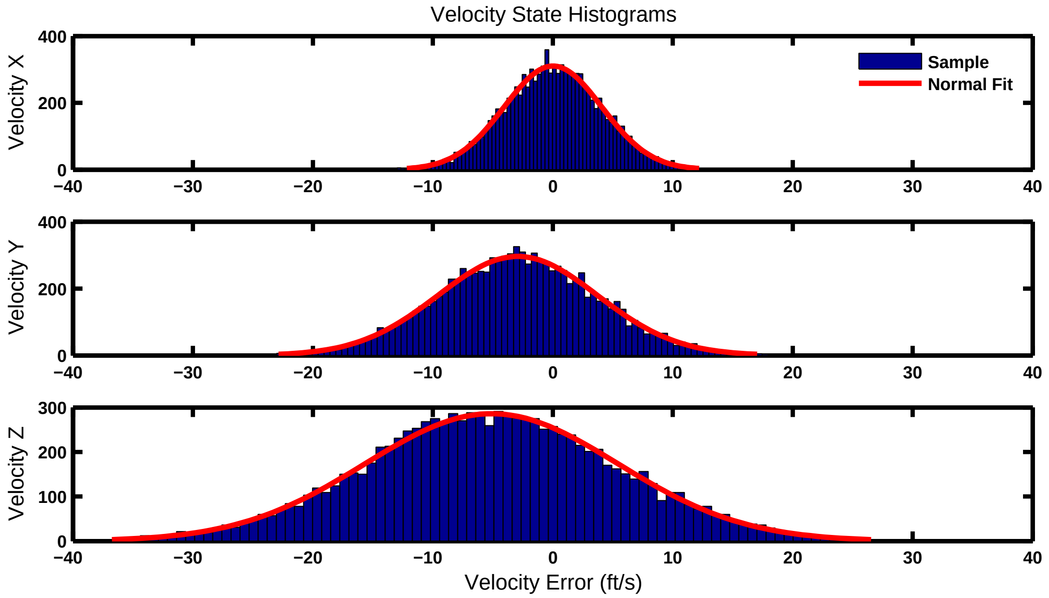

Figure 4.2

Large Sample Monte Carlo Histogram, Velocity

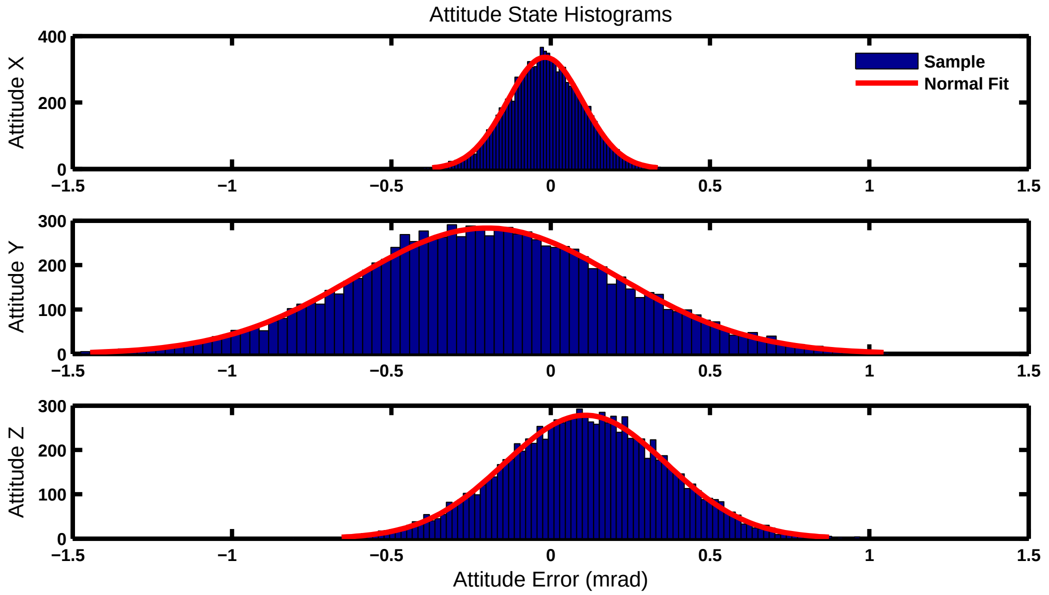

Figure 4.3

Large Sample Monte Carlo Histogram, Attitude

Instead, they advocates running the simulation, compute the statistics, and then scale by the standard error by $1/\sqrt{N}$ to develop a model for bounding the error in the assessment of the statistics.[25]

Alternatively, Montgomery and Runger give an expression for bounding the mean by the standard error, Equation (4.2).[47] The expression can be re-formulated in terms of the point estimator $\hat{p}$, Equation (4.3). Drawing from binomial statistics, the probability p can be view as the probability of failure of a hypothesis. In this case, the hypothesis could be that that a sample is not more than three standard deviations away from the mean. The probability of failure then becomes number of failures, k, over the sample population size, n. For a normal distribution, this probability would correspond to a number of runs required for estimating the error, E, in the population mean value, Equation (4.4). The percentile point for the consumer risk quotient, α, is $z_{\alpha/2}$, and n is the number of samples. Rearranging Equation (4.4) for the error term, E, results in the equation for the standard error for a normal distribution.

$$\bar{x} - z_{\alpha/2}\frac{\sigma}{n} \leq \mu \leq \bar{x} + z_{\alpha/2}\frac{\sigma}{n} \tag{4.2}$$

$$\hat{p} - z_{\alpha/2}\frac{\hat{p}(1-\hat{p})}{n} \leq p \leq \hat{p} + z_{\alpha/2}\frac{\hat{p}(1-\hat{p})}{n} \tag{4.3}$$

$$n = \left(\frac{z_{\alpha/2}\sigma}{E}\right)^2 = \left(\frac{z_{\alpha/2}}{E}\right)^2 \hat{p}(1-\hat{p}) \tag{4.4}$$

For empirical evidence of whether the assertion made by Hanson and Beard applies and to assess the effectiveness of the error estimator presented by Montgomery and Runger, the results of the large Monte Carlo simulation were analyzed. The mean and standard deviation of the sample population was incrementally computed for n samples across the

10,000 run sample population resulting in 10,000 estimates of the population mean and standard deviation. Each subsequent estimate included one additional sample from 1 to 10,000. The estimates were then recomputed for 100 randomly permutated 10,000 run sample populations resulting in 100 estimates of the population mean and standard deviation each of the original estimates considering n samples for size n of 1 to 10,000 sample. At first, an attempt was made to build a model from the standard error similar to the expression in Equation (4.4). Fitting the data required that the standard error be multiplied by a large factor similar to that described by Hanson and Beard or requires knowledge of the standard deviation. An alternate method was needed.

Of more importance than capturing the mean of the error is capturing the standard deviation of the error so the failure probability becomes a function of the standard deviation. The standard deviation represents the uncertainty in the result. For navigation, the uncertainty describes the possible error in the state due to uncompensated sensor errors. Three times the standard deviation, 3σ, is a common design parameter. For the 100 randomly permutated sample populations, estimates of the standard deviation were computed in the method described. Figure 4.4 depicts the percent error for the position error standard deviation estimates. The percent error is respective of the best estimate available, the standard deviation computed over the entire 10,000 run sample population. The standard deviation estimates for the velocity error and attitude error are shown in Figure 4.5 and Figure 4.6, respectively. The black lines represent the 90% and 99% estimates. The red lines represent the predicted error for a confidence interval of 90% and 99%.

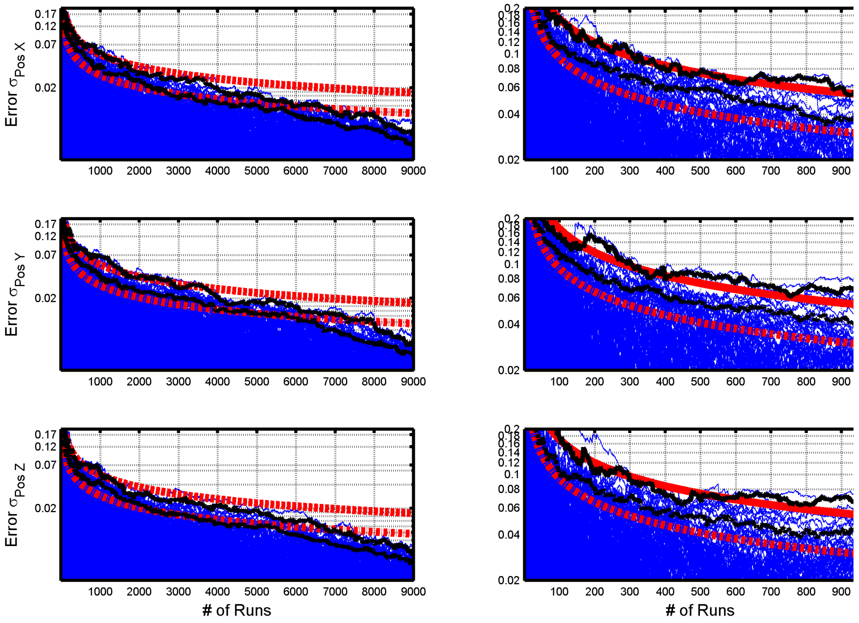

Figure 4.4

Large Sample Monte Carlo with 100 Permutations σ_{error} for Position

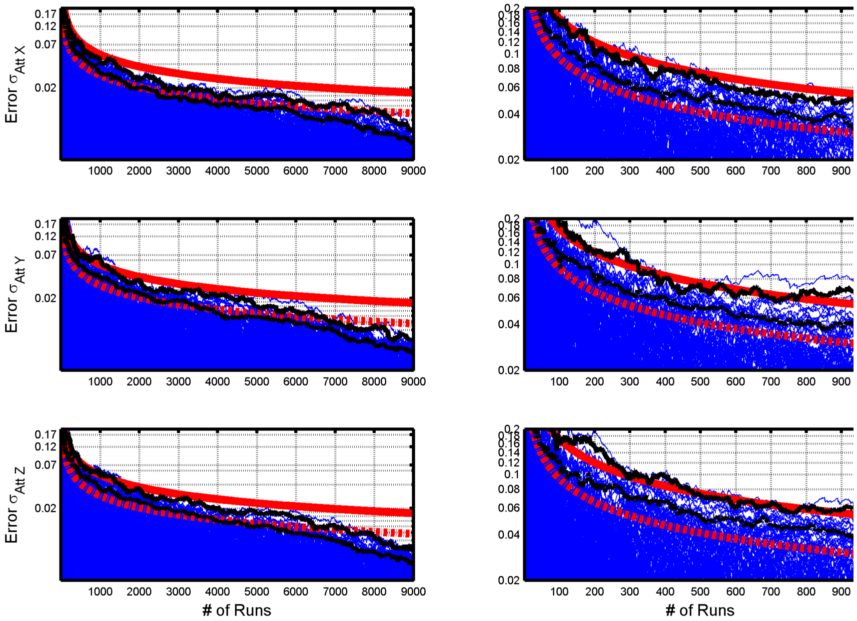

Figure 4.5

Large Sample Monte Carlo with 100 Permutations σ_{error} for Velocity

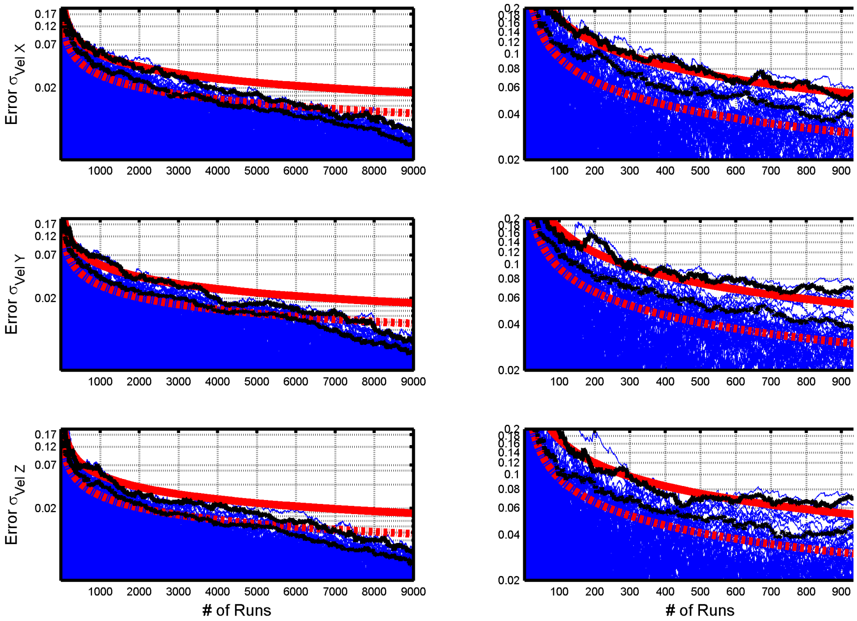

Figure 4.6

Large Sample Monte Carlo with 100 Permutations, σ_{error} for Attitude

On the second attempt to develop a model for the prediction of sampling error, the predicted error was derived from the Chi-Squared, χ^2, distribution for a given confidence interval and numbers of degrees of freedom. The χ^2 is a common distribution used for variances of a normal distribution. Since the output has been shown to be approximately normal, the χ^2 distribution should yield a reasonable estimate for the error. Also, since the variance of the data is being fit to a distribution and not the data, the standard deviation is not needed to estimate the error ratio, E/n, for a particular number of runs. From Montgomery and Runger, if s^2 is the sample variance from a random sample of n observations from a normal distribution with unknown variance, then a $100(1-\alpha)\%$ confidence interval on σ^2 is given by Equation (4.5).

$$\frac{(n-1)s^2}{\chi_{\alpha/2,n-1}} \leq \sigma^2 \leq \frac{(n-1)s^2}{\chi_{1-\alpha/2,n-1}} \tag{4.5}$$

To derive the expression for the error as a function of number of Monte Carlo runs, the error expression for, E, is developed, and an expression for the maximum error estimate as a function of n can then be found for a specific confidence interval, Equation (4.6). The red lines in Figures 4.4, 4.5, and 4.6 represent the standard deviation error model based upon the χ^2 distribution for a confidence interval of 90% and 99%.

$$E = \frac{s}{\sigma} - 1 = \frac{\chi^2_{1-\alpha/2,n-1}}{(n-1)} - 1 \tag{4.6}$$

The model under predicts the empirical error estimates slightly for $n \leq 2000$ but not by more than 2% with respect to the standard deviation. Over 1000 runs, the χ^2 based model bounds the error in the standard deviation well. The results show that for 500 runs, approximately 7.5% error is possible. The error can be reduced to approximately 5% with 1000 runs and 1% with 6800 runs.

4.2 Navigation Error Sensitivity Study

This section explores the sensitivities associated with a Navigation system. The accuracy of a navigation system is a function of the error sources that go into the system. The error sources for an inertial navigation system are different than those of an inertial navigation system which is aided by GPS measurements. Similarly, they will differ by alignment technique. A system which is aligned by a method independent of the inertial sensors will see the initial attitude errors as independent error sources. By contrast, a system which is aligned through gyrocompassing will show the sensitivity to the initial attitude error in the instruments errors. In this section, the different alignment and analysis methods will be examined independently. First, sensitivities will be developed for insertion error assuming no correlation between the initial attitude and the instrument errors. The presented error sensitivities will corroborate the correlation data from the vehicle 6-DOF simulation presented in Chapter 2. Alignment error sensitivities will be produced and finally, sensitivities will be developed for insertion error which include the alignment process and attitude error to instrument error correlations, with and without aiding.

4.2.1 Insertion Error Sensitivity Analysis with Uncorrelated Alignment Errors

A Monte Carlo based sensitivity analysis was performed over an Ares I trajectory with a RINU-like inertial instrument error budget. The trajectory is for an Ares I light/fast vehicle configuration from an early design cycle. The trajectory was simulated for an Ares

I lunar mission with due East launch to an insertion altitude of 71 nautical miles. The target orbit had apogee altitude of 100 nautical miles and perigee altitude of -11 nautical miles. The trajectory specific force, Figure 4.7, and angular rates, Figure 4.8, are shown. The error sources chosen for the sensitivity study are shown in Table 4.1

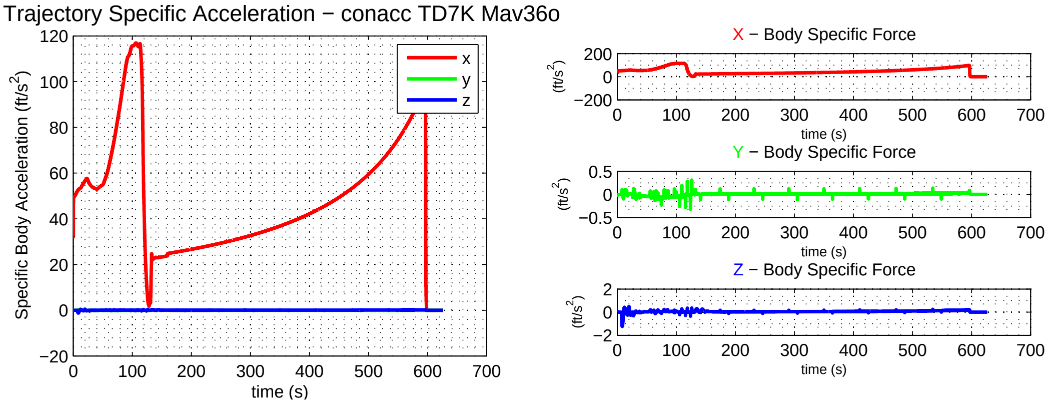

Figure 4.7

Ares I Based Trajectory Specific Force

Instrument error sources which can be approximated by other error sources, such as gyro bias instability, were not included in the sensitivity study. Also, error sources with specific dependencies on the operating environment, such as even order scale factor terms, aniso-elasticity, and cross-coupling terms were not included. Coning error and sculling error are also not included as study of those error sources would comprise an independent study of their own. The terms excluded are not error sources typically found in a product brochure, or sales ’slick’, from an inertial instrument hardware vendor. The purpose of this analysis is for the understanding of the major drivers for insertion accuracy in terms of the

Table 4.1

Insertion Error Sensitivities Error Sources

Instrument Error Source	Parameter Name	Applied Axis (Body)
Initial Velocity Error	InitialVelocityError_1	All
Initial Position Error	InitialPositionError_1	All
Initial Attitude Error	InitialYawError_1	about X
	InitialPitchError_1	about Y
	InitialRollError_1	about Z
Accelerometer Scale Factor	AccScaleFactorError_1	X
	AccScaleFactorError_2	Y
	AccScaleFactorError_3	Z
Accelerometer Bias	AccBiasError_1	X
	AccBiasError_2	Y
	AccBiasError_3	Z
Accelerometer Non-Linearity	AccScaleFactorNonLinError_1	All
Accelerometer Output Noise	AccOutputNoise_1	All, $f(t)$
Accelerometer Quantization	AccQuant_1	All, $f(t, \Delta V)$
Accelerometer Non-Orthogonality	AccMisaError_1	X about Y
	AccMisaError_2	Z about Z
	AccMisaError_3	Y about X
	AccMisaError_4	Y about Z
	AccMisaError_5	Z about X
	AccMisaError_6	Z about Y
Velocity Random Walk	AccRandomWalkError_1	All, $f(t)$
Gyro Scale Factor	GyroScaleFactorError_1	X
	GyroScaleFactorError_2	Y
	GyroScaleFactorError_3	Z
Gyro Bias	GyroBiasError_1	X
	GyroBiasError_2	Y
	GyroBiasError_3	Z
Gyro Non-Linearity	GyroScaleFactorNonLinError_1	All
Gyro Output Noise	GyroOutputNoise_1	All, $f(t)$
Gyro Quantization	GyroQuant_1	All, $f(t, \Delta\theta)$
Gyro Non-Orthogonality	GyroMisaError_1	X about Y
	GyroMisaError_2	X about Z
	GyroMisaError_3	Y about X
	GyroMisaError_4	Y about Z
	GyroMisaError_5	Z about X
	GyroMisaError_6	Z about Y
Gyro Angular Random Walk	GyroRandomWalkError_1	All, $f(t)$

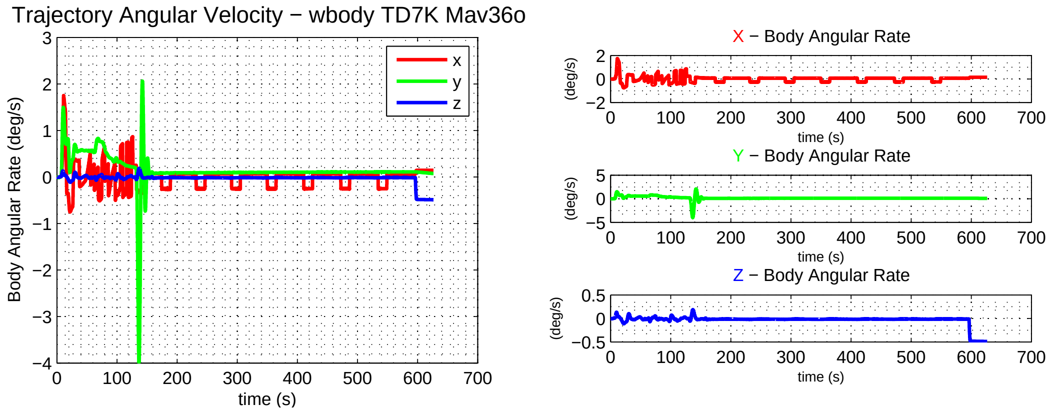

Figure 4.8

Ares I Based Trajectory Angular Rate

Navigation system and to provide insight into where, during operation, the majority of the navigation error originates for inertial navigation.

The salient assumption of the analysis in this section is that the initial attitude was applied as a Gaussian random draw from a set of statistics captured from gyrocompassing the instrument for a RINU-like error budget. In simulating the initial alignment in this manner, the assumption is made that the initial alignment is statistically independent of the inertial instrument uncompensated error statistics. This is a very common way of simulating the initial alignment, whether or not it is correct. In covariance analysis, applying the initial attitude in this way is analogous to diagonalizing the attitude portion of the initial error covariance matrix. The simulated alignment error uncertainties are contained in Table 4.2

In simulation, the full error budget plus the initial alignment errors were dispersed at the beginning of the reference trajectory. The trajectory was then navigated with the dispersed error sources. The final state at orbit insertion was captured and statistics were computed

Table 4.2

Monte Carlo Analysis with Uncorrelated Alignment Error, Alignment Dispersion

Initial Attitude Error		1σ Dispersion
Body Roll	ϕ	97.9 arcsec
Body Pitch	θ	12.9 arcsec
Body Yaw	ψ	13.2 arcsec

over the sample population. The Monte Carlo consisted of 500 dispersed runs. The result of the fully dispersed run are contained in Table 4.3.

After the full run, the trajectory was then rerun for each error source. In total, the sensitivity analysis consists of approximately 18500 dispersed runs, or 11,655,000 seconds of simulated flight. For these runs, only the error source being examined was dispersed. This allows for the determination of the statistical contribution of each error source to the whole. This method assumes linearity and that the error sources are not correlated. These assumptions can be shown to be reasonable for the purpose of assessing system sensitivities by taking the root sum square of the individual errors and comparing the result to the statistical result of the fully dispersed set. For the case where the initial alignment error is treated as an independent error source, there is no appreciable difference in the statistics.

This method of computing error sensitivities is analogous to the method of computing sensitivities from Consider Covariance analysis discussed by Tapley, Shultz, and Born.[79] Consider Covariance analysis is a covariance analysis method in which additional parameters, Consider parameters, are appended to the state, Equation (4.7). The Consider co-

Table 4.3

Monte Carlo Analysis with Uncorrelated Alignment Error, Monte Carlo Result

State Variable		Orbit Insertion Error (1σ)
Position (ECI, TOD)	X	1019.6 ft
	Y	17897.2 ft
	Z	2836.8 ft
Velocity (ECI, TOD)	X	3.50 ft/s
	Y	6.09 ft/s
	Z	9.91 ft/s
Attitude (ECI, TOD)	X	21.5 arcsec
	Y	86.7 arcsec
	Z	49.0 arcsec

variance is defined from the state expectation, Equation (4.8), and includes the Consider parameter covariance and state to Consider parameter covariance terms. The sensitivity matrix, S_{xc}, is defined as the partial derivative of the state with respect to the Consider parameters and can be solved for directly from the augmented covariance matrix, Equation (4.9). Unlike covariance analysis, the covariance matrix, in this analysis, is not propagated directly. Rather the P_{xc} portion of the covariance matrix is determined through Monte Carlo analysis where P_{cc} is a diagonal matrix containing the variances of the instrument errors being simulated. The resultant sensitivity matrix, S_{xc}, represents the sensitivity of the portion of the state estimate, $\hat{x}$, to the Consider parameter part of the augmented state, $\hat{c} = c$.

$$X = \begin{bmatrix} x \\ \\ c \end{bmatrix} \tag{4.7}$$

$$P = E\left(\begin{bmatrix}\hat{x}_c - x \\ \bar{c} - c\end{bmatrix}\begin{bmatrix}(\hat{x}_c - x)^T & (\bar{c} - c)^T\end{bmatrix}\right) = \begin{bmatrix}P_{xx} & P_{xc} \\ P_{cx} & \bar{P}_{cc}\end{bmatrix} \tag{4.8}$$

$$S_{xc} = \frac{\partial \hat{x}_c}{\partial \hat{c}} = P_{xc}\bar{P}_{cc}^{-1} \tag{4.9}$$

Figure 4.9 is a bar plot depicting the sensitivity of the insertion position state to the simulated error sources. Figures 4.10 and 4.11 depict the error sensitivities for the velocity and attitude error state at insertion. The error sensitivities have been normalized with respect to the 1σ insertion error from the statistical combination of the insertion error from the individual Monte Carlo sets.

From the sensitivity plots it is easily observed that the dominant error source to the insertion error is the initial attitude. The errors are respective of the Earth Centered Inertial (ECI) frame, with the z-axis normal to the equatorial plane. The greatest sensitivity is shown to be to the initial roll error. The initial roll error is essentially the initial heading error, or error in initial azimuth. The error in initial pitch and yaw are the leveling errors and represent an uncertainty in the down direction, or direction of the measured gravity vector. The scale factor errors show sensitivity in the direction of thrust. In this case, it appears that the vehicle is primarily thrusting in the direction of the ECI x-axis. For this instrument error budget, there is a particularly strong sensitivity to the accelerometer non-linearity. This is not always the case and depends on the accelerometer non-linearity specification. In attitude the error is again driven by the initial attitude error with no contribution from

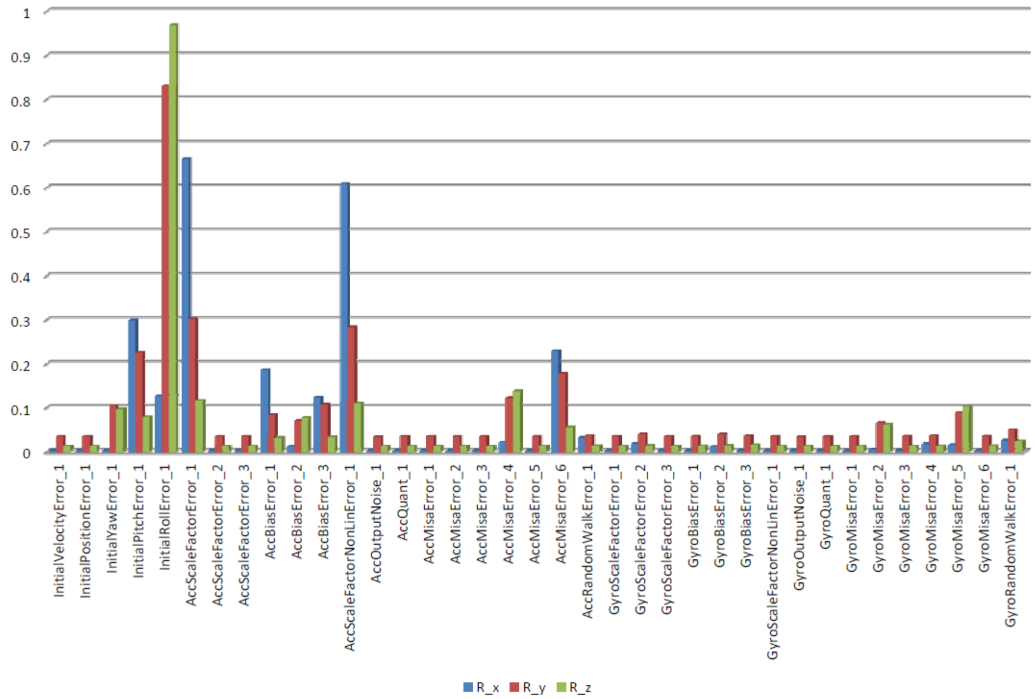

Figure 4.9

Insertion Error Sensitivities with Uncorrelated Alignment Errors, Position (ECI)

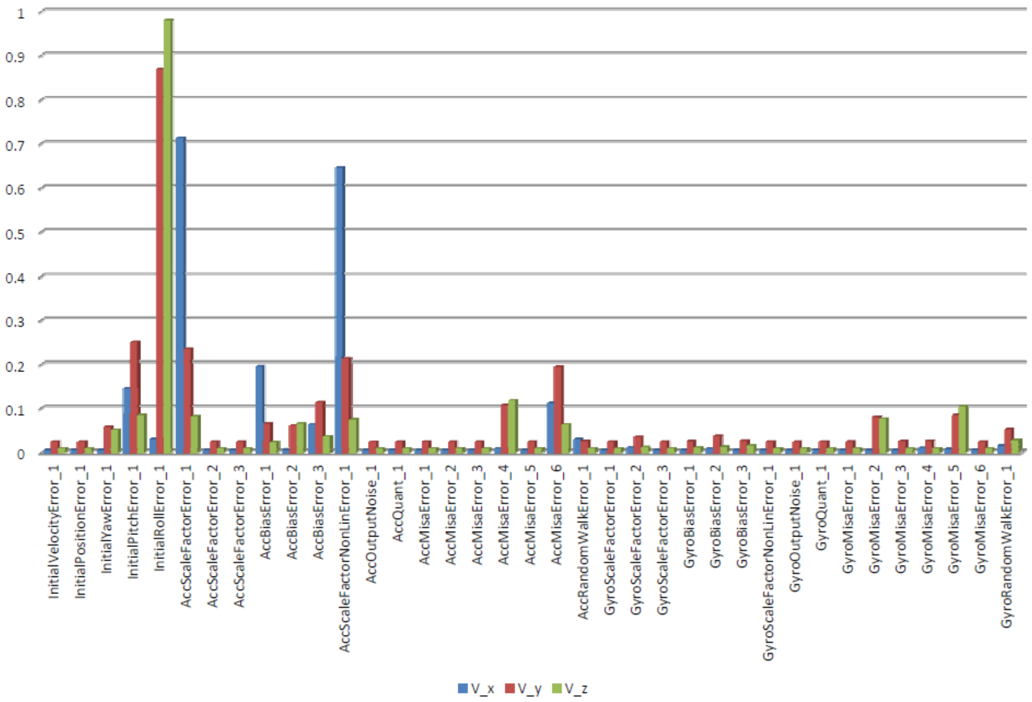

Figure 4.10

Insertion Error Sensitivities with Uncorrelated Alignment Errors, Velocity (ECI)

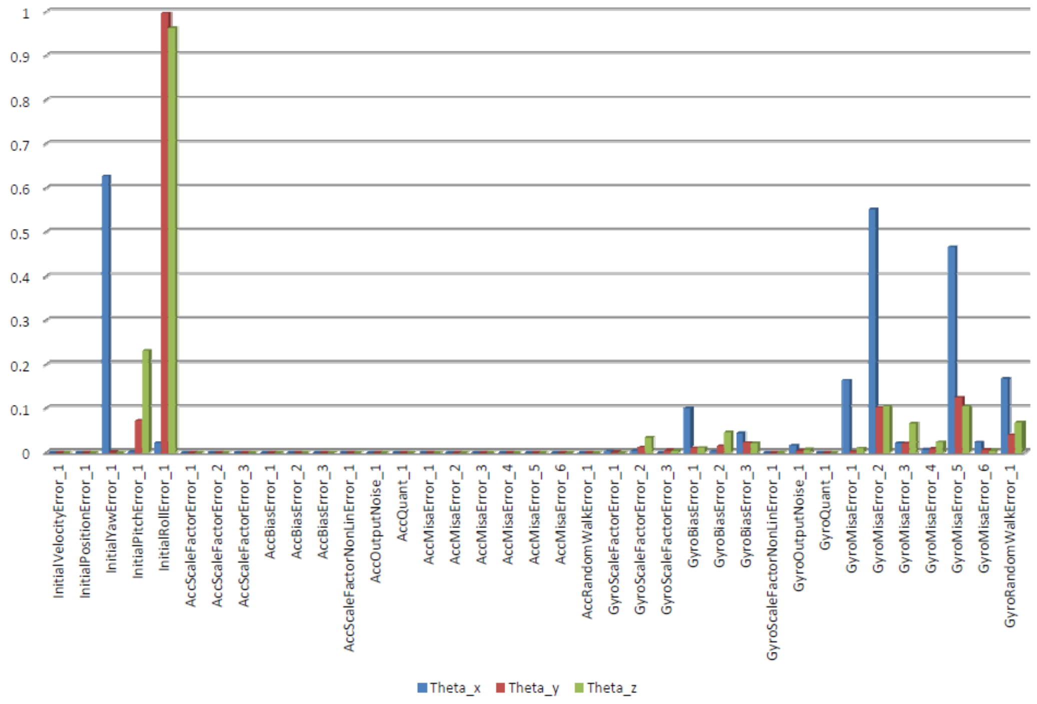

Figure 4.11

Insertion Error Sensitivities with Uncorrelated Alignment Errors, Attitude (ECI) accelerometer error sources, shown in Figure 4.11. For the uncorrelated attitude error sensitivity result, the dominant gyro errors appear to be gyro non-orthogonality/misalignment with the noise term, gyro random walk, and the bias showing only modest sensitivity.

4.2.2 Alignment Error Sensitivities

This analysis looks at the initial alignment sensitivities to the inertial instrument error sources for an initial alignment developed through gyrocompassing. This study uses the same instrument error budget as was used in the previous section on insertion error sensitivities with uncorrelated initial alignment errors. This section focuses on those initial alignment to instrument error correlations. A benign pre-launch trajectory was used with constant angular rate input to the gyro model and constant specific force input to the accelerometer model. The truth position remains stationary relative to the Earth. The gyrocompassing algorithm used is the 6-state Kalman filter, described in Chapter 3. The filter uses zero velocity measurements and the filter state consists of velocity and attitude errors. The filter was quickly tuned for the instrument error budget.

The analysis method is similar to the method used in the uncorrelated attitude error sensitivity study. A 500-run Monte Carlo set was run for the full error budget. The analysis was then repeated for each error source. For each run, a coarse alignment algorithm, described in Chapter 3, was run for two minutes to initialize the fine alignment filter. The fine alignment filter was then run for 18 minutes for a total pre-launch trajectory of 20 minutes in duration. Given a benign pre-launch environment, a 20 minutes gyrocompassing time has been observed to be adequate for convergence. The pre-launch environment is stated to be benign, this means that there is no pad twist and sway motion added to the input angular rates and specific force. This study is focused on assessing the initial alignment error sensitivities to the instrument error sources, but a detailed analysis of gyrocompassing must include the effect of twist and sway.

The total alignment error is shown in Table 4.4. The position and velocity states are not considered in this analysis because they would typically be reset at or prior to launch and would not typically affect the navigation accuracy during ascent. Table 4.4 shows the initial alignment error statistics from the fully dispersed Monte Carlo set and the error statistic obtained from a statistical combination of the Monte Carlo sets for the individual error sources. The values are different due to system non-linearities or uncaptured error sources.

Table 4.4

Monte Carlo Analysis, Initial Attitude Error from Gyrocompassing

Initial Attitude Error		Full (1σ)	RSS (1σ)
Body Roll	ϕ	97.9 arcsec	90.0 arcsec
Body Pitch	θ	12.9 arcsec	12.9 arcsec
Body Yaw	ψ	13.2 arcsec	13.1 srcsec

Figure 4.12 contains the individual error, normalized by the total error, and depicts the initial alignment error, derived through gyrocompassing, to inertial instrument error sensitivities. In this figure, the initial alignment error is relative to the vehicle body frame. The body x and y directions define the level plane and errors in the x and y direction are

denoted errors in level. Initial attitude error about the body roll axis, the x axis, represent the error in initial azimuth and are referred to as initial heading error. Figure 4.12 show the initial error in level is most sensitive to accelerometer errors, specifically the accelerometer bias and misalignment. This is an intuitive result since the gravity vector is used in leveling. The initial heading error shows little sensitivity to accelerometer error sources. The dominant error sources in initial heading error are the gyro bias and the gyro noise term, gyro angular random walk. This also follows intuitively, given that the North direction is defined based upon the cross-product of the gravity vector and the measurement of the measured Earth rotation vector. In that relationship, the gravity vector is significantly easier to observe.

Typically, the effective East gyro bias is considered the dominant error in gyrocompassing. The results in this study show that, for the error budget used, gyro random walk is almost equal to the gyro bias in contribution to the alignment error developed from gyrocompassing. With longer gyrocompassing time and better filter tuning, it is possible to reduce the error contribution due to the noise term, gyro angular walk. Doing so would, in turn, reduce the total initial alignment error and the sensitivity to angular random walk instrument error source. This process is not without limits. The ability for a filter to estimate the initial azimuth error is physically limited by observability of the Earth rotation rate. The analytical limit is described by Equation (4.10) as a function of the two dominant error contributors. The equation assumes all other contributors to be negligible. The theoretical 1σ initial heading error, σ_α, is given as a function of the 1σ gyro bias error, $\sigma_{gyrobias}$, the mean square of the angular rate noise from the gyro angular random walk, q_{ARW}, the

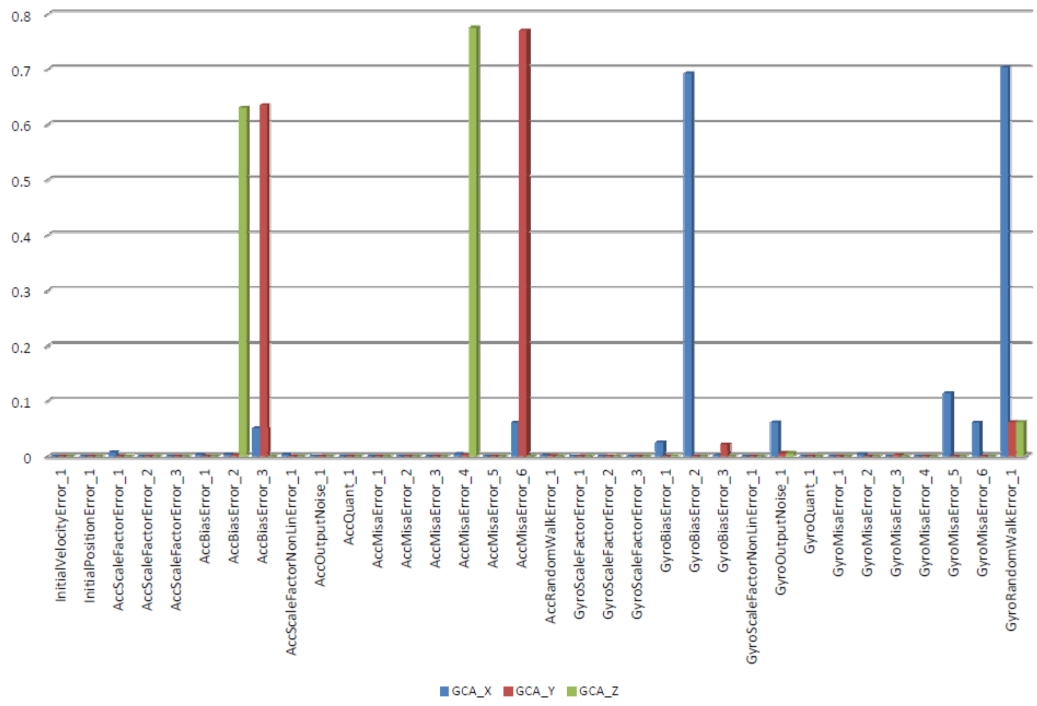

Figure 4.12

Monte Carlo Analysis, Initial Alignment Sensitivities from Gyrocompassing (Body) rotational rate of the Earth, Ω_{Earth}, the latitude, ϕ, and the time since the filter was started, Δt.

$$(\sigma_\alpha)_{limit} = \lim_{\Delta t \to \infty} \left(\frac{\sqrt{([\sigma_{gyrobias}]_{East}\, \Delta t)^2 + q_{ARW} \Delta t}}{\Omega_{Earth} \Delta t \cos\phi} \right) \tag{4.10}$$

4.2.3 Insertion Error Sensitivity Analysis with Correlated Alignment Errors

The analysis presented in this section brings together the sensitivity analysis performed with uncorrelated initial alignment and the initial alignment to instrument error sources sensitivity study. The results are also tied back to assertions made in Chapter 2 about vehicle insertion error sensitivities. The analysis was performed similarly to the insertion error with uncorrelated initial alignment sensitivity study. A Monte Carlo set of 500 was run with the same error budget and trajectory as in the previous analysis. For each run, the initial alignment was developed through 20 minutes of gyrocompassing prior to the ascent trajectory. The 500 runs were then repeated for each error source to determine the sensitivities of insertion error to the individual inertial instrument error sources.

Table 4.5

Monte Carlo Analysis with Correlated Alignment Error, Alignment from Gyrocompassing

Initial Attitude Error		1σ Dispersion
Body Roll	ϕ	97.9 arcsec
Body Pitch	θ	12.9 arcsec
Body Yaw	ψ	13.2 arcsec

Table 4.5 contains the initial alignment result. The initial alignment numbers for the study with uncorrelated initial alignment errors were chosen to match this result. Table 4.6 contains the insertion state errors for the fully dispersed run. The RSS column contains the statistical combination of the individual error contributors. The simulation is non-linear, but the method of assessing sensitivities assumes linearity and also makes the assumption that the error sources are uncorrelated, i.e. that is that P_{xc} and P_{cx} in Equation (4.8) are diagonal. The Difference column contains the percent difference between the two assessments of the results and is an indicator of how well the assumptions hold for assessing sensitivities in this way.

Table 4.6

Monte Carlo Analysis with Correlated Alignment Error, Monte Carlo Result

Insertion State Error		Full (1σ)	RSS (1σ)	Difference
Position (ECI, TOD)	X	959.67 ft	950.15 ft	1.0%
	Y	1684.3 ft	1608.8 ft	4.5%
	Z	2755.5 ft	2531.3 ft	8.1%
Velocity (ECI, TOD)	X	3.47 ft/s	3.44 ft/s	0.8%
	Y	5.70 ft/s	5.32 ft/s	6.7%
	Z	9.68 ft/s	8.87 ft/s	8.4%
Attitude (ECI, TOD)	X	20.8 arcsec	21.0 arcsec	0.85%
	Y	84.7 arcsec	77.6 arcsec	8.4%
	Z	50.0 arcsec	45.1 arcsec	9.6%

Figures 4.13, 4.14, and 4.15 depict the normalized sensitivities to the inertial instrument errors for insertion position, velocity, and attitude error states. Within the sensitivities, the alignment error is decomposed into instrument errors making it possible to see

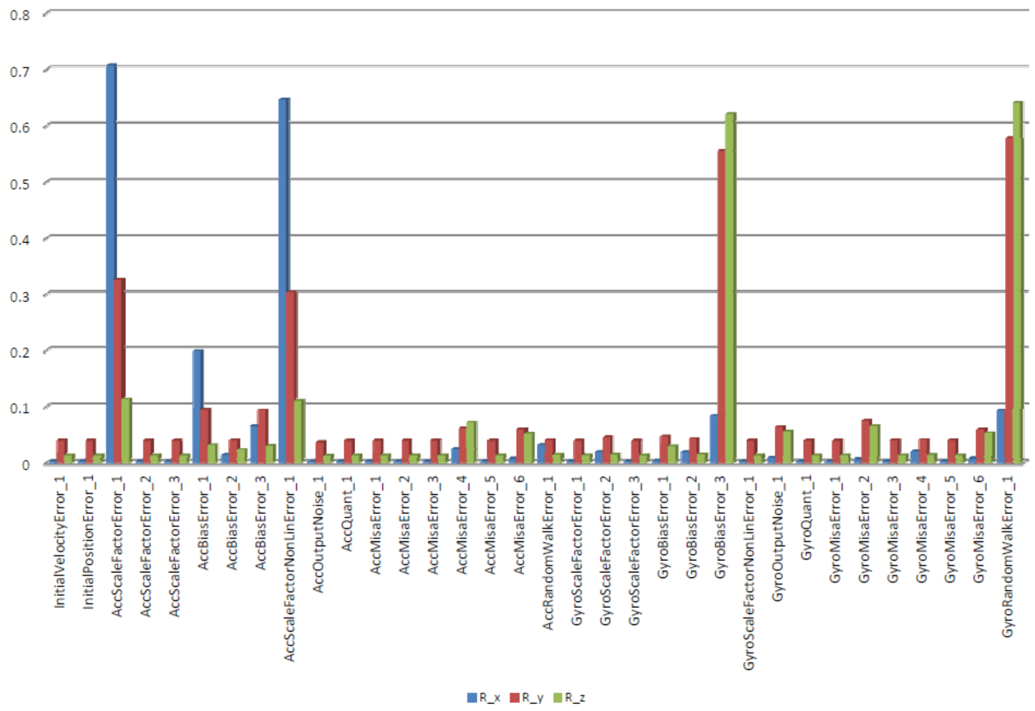

Figure 4.13

Insertion Error Sensitivities with Correlated Alignment Errors, Position (ECI)

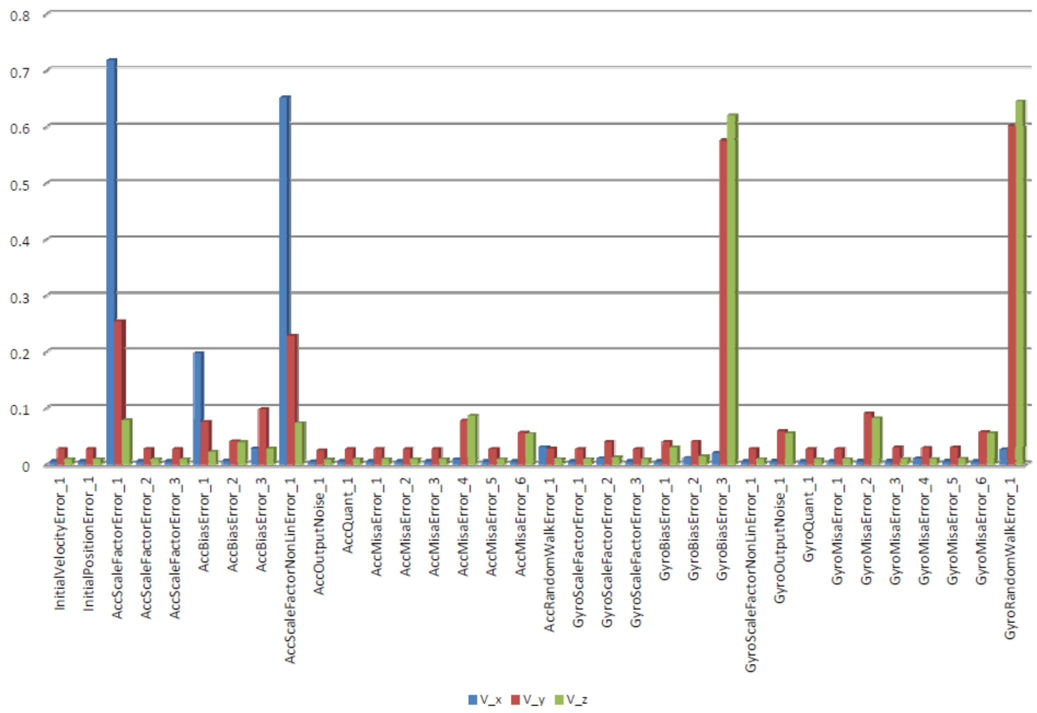

Figure 4.14

Insertion Error Sensitivities with Correlated Alignment Errors, Velocity (ECI)

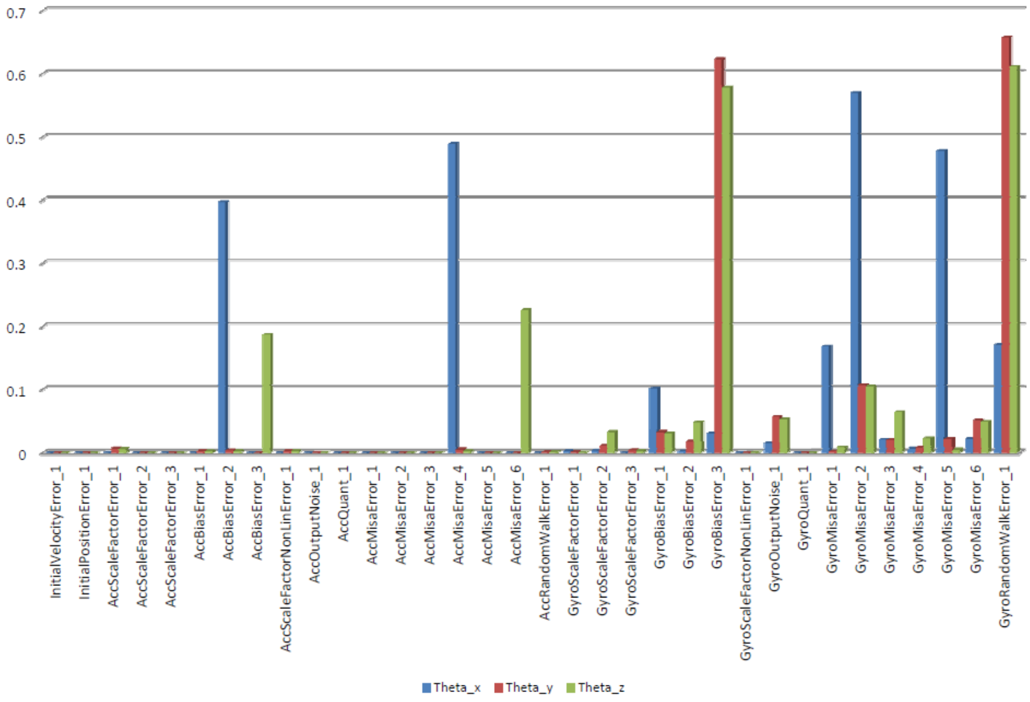

Figure 4.15

Insertion Error Sensitivities with Correlated Alignment Errors, Attitude (ECI) the true sensitivities of the inertial navigation system state errors. If only the uncorrelated sensitivity result was entertained, an incorrect assumption would likely be drawn that the contribution of the total insertion error from the gyro bias is small. This is obviously not the case. The dominant errors in the ECI position error and velocity error at insertion for the trajectory and error budget analyzed are gyro bias, gyro random walk, accelerometer bias, the accelerometer misalignment, and gyro misalignment. The error sensitivities are consistent with what would be expected in that most of the error is owed to the initial alignment process. The attitude sensitivities differ from the alignment sensitivities mostly due to the difference in the coordinate frame. For position and velocity insertion state error, the sensitivities along the ECI y and z axes share sensitivities with the alignment and leveling process. The position and velocity insertion state errors in the ECI x coordinate direction show large sensitivity to the accelerometer scale factors. Intuitively, the accelerometer scale factors should show a high sensitivity in the ECI coordinate direction that aligns with the majority of the vehicle thrust. Figure 4.16 illustrates the ECI velocity state for the reference trajectory. From observation, the majority of the thrust in the trajectory simulated is along the ECI x coordinate.

In addition to the Cartesian insertion state errors, the Keplerian elements were also computed for this analysis with sensitivities to inertial instrument errors. Figure 4.17 depicts the sensitivities of the minimal set of Keplerian elements discussed in Chapter 2. The bar plot confirms that the error sensitivities of in-plane and out-of-plane insertion error, parameterized as Keplerian elements, are distinct in terms of the error sources from which they are developed. The in-plane error, defined by the errors in radius of apogee and

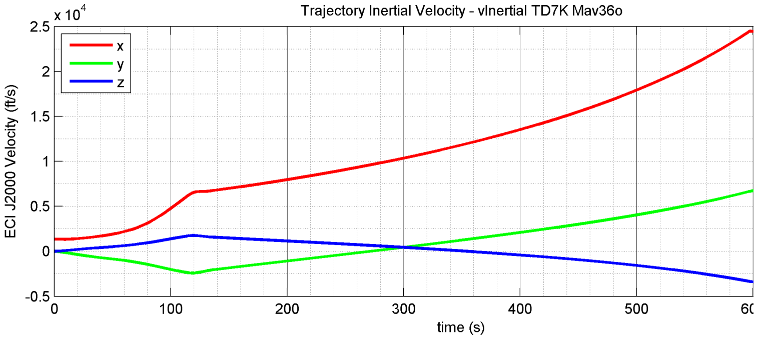

Figure 4.16

Ares I Based Trajectory, ECI Velocity

semi-major axis, is developed primarily from accelerometer errors confirming their sensitivity to in-plane error sources, e.g. errors in acceleration due to vehicle thrust or expected thrust due to errors in the acceleration measurement. The out-of-plane errors are defined by wedge angle or inclination, i, and right ascension of the ascending node, denoted as Ω or RAAN. The out-of-plane orbit insertion errors show sensitivity to accelerometer bias, accelerometer misalignment, gyro bias, angular random walk, and gyro misalignment. This set of errors is in common with the initial alignment error sensitivities implying that the out-of-plane error is mostly developed prior to launch during the initial alignment process. Interestingly, the error in inclination shows sensitivity to error sources related to leveling error in addition to azimuth error while Ω shows sensitivity only to error sources associated with initial azimuth error. Wedge angle appears to be primarily developed from gyro bias uncertainty and gyro angular random walk. Considering the relationship discussed in Chapter 2, this would indicate an increased sensitivity to errors in Ω and a strong dependence on initial heading error.

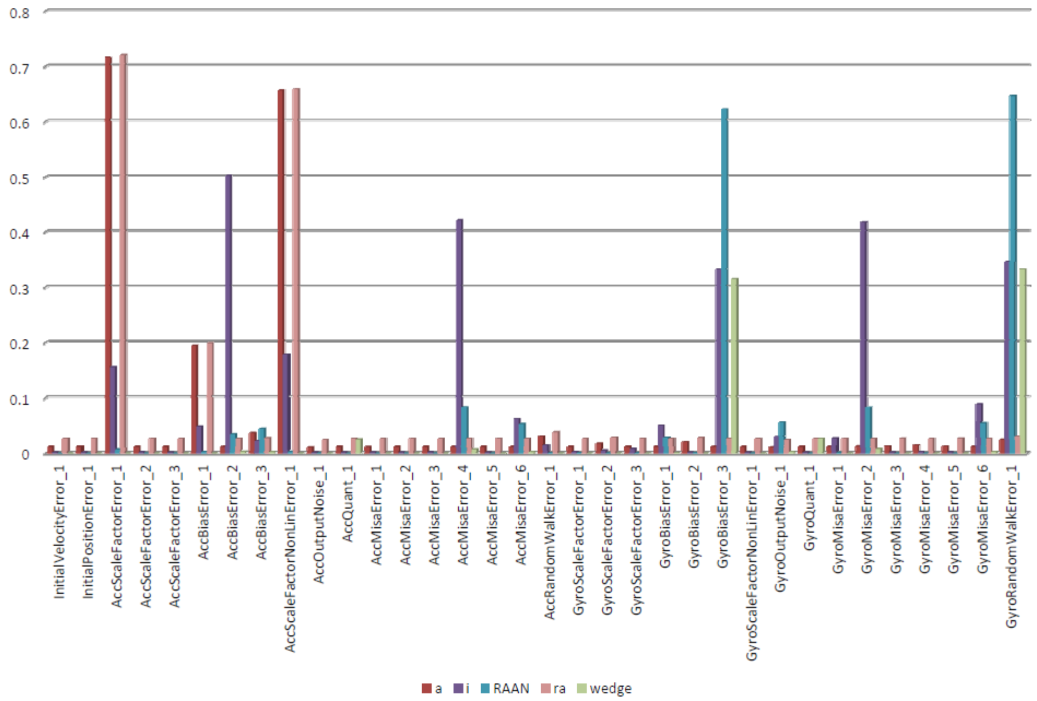

Figure 4.17

Insertion Error Sensitivities with Uncorrelated Alignment Errors, Orbital Elements

Table 4.7

Insertion Accuracy Error Analysis, Correlated Vs. Uncorrelated Initial Attitude Errors

Insertion State Error		(1σ) Result with Initial Attitude from		% Difference in σ^2
		Gyrocompassing	Independant Draw	
Position (ECI, TOD)	X	959.67 ft	1019.6 ft	13%
	Y	1684.3 ft	1797.2 ft	14%
	Z	2755.5 ft	2836.8 ft	6.0%
Velocity (ECI, TOD)	X	3.47 ft/s	3.50 ft/s	1.7%
	Y	5.70 ft/s	6.09 ft/s	14%
	Z	9.68 ft/s	9.91 ft/s	4.8%
Attitude (ECI, TOD)	X	20.8 arcsec	21.5 arcsec	6.6%
	Y	84.7 arcsec	86.7 arcsec	4.8%
	Z	50.0 arcsec	49.0 arcsec	3.7%

Having looked at analyses with correlated and uncorrelated alignment errors, respectively, allows a brief comparison of the two methods for assessing inertial navigation sensitivities. Table 4.7 contains the results from the two analyses. In the analyses, all analysis parameters were kept constant except for the inclusion of the gyrocompassing process for determining the initial alignment. The results differ indicating that the approximation of the initial alignment as an independent error not only conceals the true system sensitivities but also introduces error into the solution resulting in an over prediction of the error in most cases for this analysis. The differences in the error variance are not insignificant. The simulation was seeded such that the errors over both 500 run Monte Carlos were common. Unfortunately, given that that random draws made for the analysis were applied to different parameters, the result cannot be considered conclusive given the possibility of sampling error in estimating the standard deviations over 500 runs. However, it can be stated that the the comparison indicates that a proper error analysis for an inertial navigation system includes simulation of the initial alignment process.

4.2.4 Insertion Error Sensitivity Analysis with GPS Aiding

This study looks at the sensitivity of insertion error to inertial instrument errors with GPS aiding. A conclusion which should be drawn from the sensitivity analysis with correlated alignment errors and the initial alignment error sensitivity is that the insertion state error for the inertial solution is very dependent upon the pre-launch alignment and the inertial instrument errors during pre-launch alignment. This is primarily due to the fact that for an inertial system, the error in the system is monotonically increasing from the time the gyrocompassing filter ceases to update the solution and the initial alignment is determined. This is due to the continuous integration of inertial instrument and initial state error and the lack of available information from which to estimate and correct during inertial navigation. The inclusion of aiding offers a different paradigm. The inertial navigation system is receiving information throughout flight which can be used to estimate and correct for state and/or instrument errors. In a way, this closes the loop for inertial navigation and allows a feedback mechanism with respect to the integrated instrument error.

Table 4.8

Monte Carlo Analysis with GPS Aiding, GPS Errors

GPS Horizontal Position Measurement Error (1σ)	33.5 ft
GPS Vertical Position Measurement Error (1σ)	42.0 ft
GPS Velocity Measurement Error (1σ)	0.0200 ft/s

For this analysis, the same configuration was used as was used for the sensitivity analysis with correlated initial alignment errors, with one exception. The same Ares I trajectory variant was simulated with angular rates and trajectory specific force input illustrated in figures 4.8 and 4.7. The instrument error budget was held constant between the analyses. The primary discerning feature for this analysis was that, in addition to the instrument error model and inertial alignment algorithms, a simplistic GPS error model was added and a navigation state filter that takes in position and velocity measurements from the GPS error model was employed to estimate and correct state errors during ascent. The filter is a

Kalman filter with position, velocity, and attitude states. The GPS errors used are contained in Table 4.8

Table 4.9

Monte Carlo Analysis with GPS Aiding, Monte Carlo Result

Insertion State Error		Full (1σ)
Position (ECI, TOD)	X	≤ 5 ft
	Y	≤ 5 ft
	Z	≤ 5 ft
Velocity (ECI, TOD)	X	≤ 0.1 ft/s
	Y	≤ 0.1 ft/s
	Z	≤ 0.1 ft/s
Attitude (ECI, TOD)	X	20.6 arcsec
	Y	83.2 arcsec
	Z	48.6 arcsec

The insertion state errors were determined through Monte Carlo analysis. A set of 500 runs was made with all errors enabled. The analysis was then repeated for each error source individually to develop the sensitivities. The result of the fully dispersed run is shown in Table 4.9. Note the greatly reduced size of the errors in position and velocity in comparison to the unaided result, Table 4.6. Figures 4.18 and 4.19 depict the sensitivity of the insertion state errors to the inertial instrument errors. As with the previous sensitivities analyses, the sensitivities have been normalized with respect to the insertion state error from the fully dispersed run. The position and velocity state error sensitivity plot, Figure 4.18, is interesting because it clearly shows negligible sensitivity to the inertial instrument errors in position and velocity. The GPS measurement error was put on the plot for context and is not a product of an individual Monte Carlo.

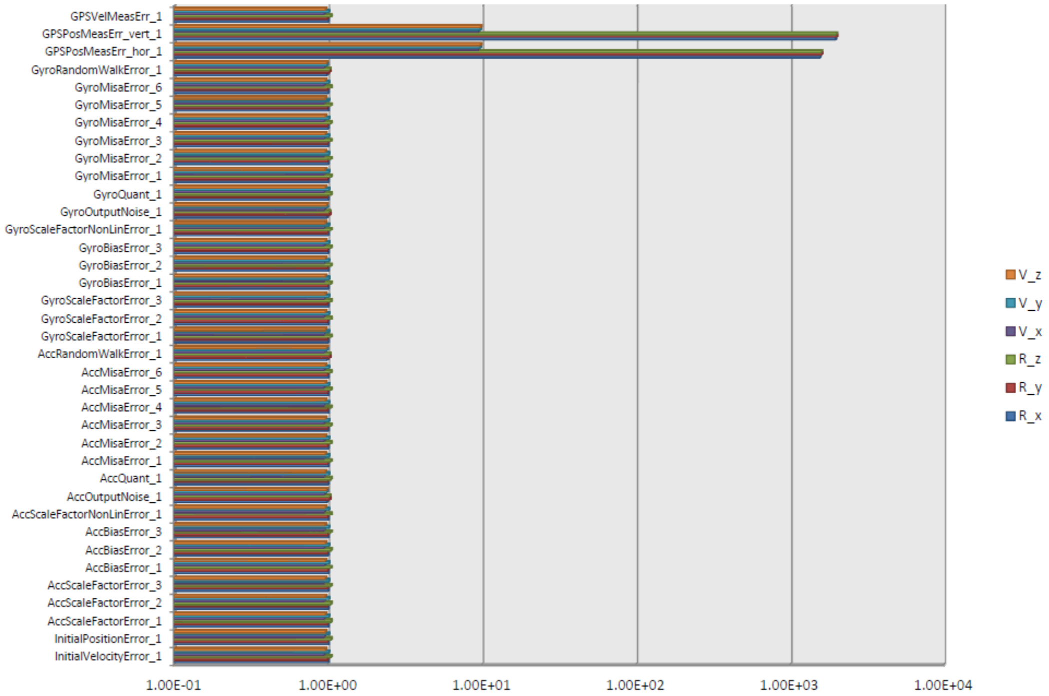

Figure 4.18

Insertion Error Sensitivities with GPS Aiding, Position and Velocity (ECI)

The 9-state Kalman filter is capable of correcting the inertial state to well below the accuracy of the GPS measurement accuracy, given the simplistic GPS error model and high quality inertial instrument error budget. The attitude insertion error states sensitivity results are very similar to those shown in the unaided analysis, Figure 4.15. The insertion attitude state errors, Table 4.9, show a slight, but not significant, reduction in error from the result of the unaided analysis, Table 4.6. This implies that the Kalman filter with GPS

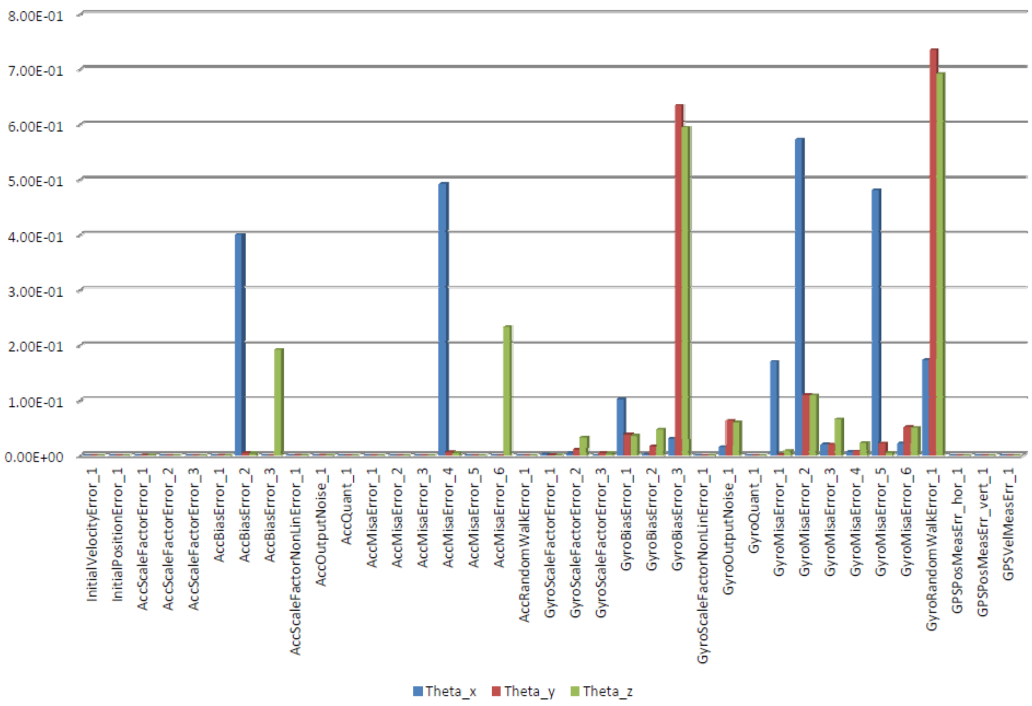

Figure 4.19

Insertion Error Sensitivities with GPS Aiding, Attitude (ECI) measurements is not very capable of reducing errors in attitude through ascent flight. More importantly, the combined result of the sensitivity analysis indicates that the Kalman filter with GPS measurements effectively decouples the position and velocity state errors from the initial attitude error. This is a significant result because it implies that, for a GPS aided inertial navigation system, the quality of the overall navigation solution is not dominated by the quality of the gyros allowing for inertial hardware which is much less costly for a better-than-inertial position and velocity solution. In such a system, the gyro quality could be sized more for what is needed for controls or for pointing as opposed to what is required for overall system performance. The inclusion of GPS aiding offers a different paradigm for launch vehicle Navigation system accuracy.

4.3 Effect of Non-Sensor Misalignment

This section focuses on misalignment errors which are not necessarily inertial sensor errors. These effects have not been previously included in sensor sensitivity studies in full, but are important from a vehicle, integration, and inertial hardware specification point of view. They also provide insight into what is needed by the Controls subsystem for ascent flight in terms of attitude state accuracy. Controlling physical misalignment and misalignment errors in the output frame require some specification on the inertial navigation hardware used. The first study in this section looks at the physical misalignment of the inertial navigation sensor frame to the vehicle body frame used by the Controls subsystem. The second looks at how the navigation state, used by the Guidance subsystem, can be corrupted by improper initialization or specification of the output frame, assuming the output frame is an inertial frame.

4.3.1 Ares I Physical Mounting Misalignment Sensitivity Study

The study described in this section was conducted to describe the effect of RINU mounting misalignment uncertainty on Ares I vehicle performance.[61] The study was conducted using MAVERIC for an Ares I vehicle configuration and focuses on the misalignment of the inertial measurements, angular rate and specific force, from the Ares I INS. The purpose of the study is to gain an understanding of the sensitivity of physical misalignment of the inertial sensors and the sensitivity of the Controls sub-system to biases on the attitude state. Previously, a study was conducted by Odette in which he concluded that the physical misalignment of the strapdown INS would result in very large plane errors at insertion.[50] Dukeman wrote a short white paper in response to the analysis which stated that the primary effect of the physical misalignment would be in angle of attack causing increased vehicle loading during flight. [49]. A third study was published in the Ares I GN&C System Design Document (SDD).[19] In this study a misalignment error was applied to the angular rate measurement only by way of Equation (4.11). The attitude angles ϕ, θ, and ψ were perturbed by a misalignment error. The S frame indicates the sensor frame and the B frame is the body frame.

$$\begin{bmatrix} p \\ q \\ r \end{bmatrix}^S = \begin{bmatrix} 1 & 0 & 0 \\ 0 & \cos\phi & \sin\phi \\ 0 & -\sin\phi & \cos\phi \end{bmatrix} \begin{bmatrix} \cos\theta & 0 & -\sin\theta \\ 0 & 1 & 0 \\ \sin\theta & 0 & \cos\theta \end{bmatrix} \begin{bmatrix} \cos\psi & \sin\psi & 0 \\ -\sin\psi & \cos\psi & 0 \\ 0 & 0 & 1 \end{bmatrix} \begin{bmatrix} p \\ q \\ r \end{bmatrix}^B \tag{4.11}$$

The analysis documentation that was in the GN&C SDD did not describe where the misalignment was applied with respect to the computation of the navigation state. From the analysis results and the lack of mention of the propagation of the inertial to body attitude quaternion, it was assumed that the misalignment was applied prior to the propagation of the navigation state. This assumption was later confirmed by the author. The results from this study incorrectly suggested that a smaller wedge angle could be achieved by incorrectly aligning the RINU and the Rate Gyro Assemblies (RGA). The analysis assumed perfect sensors other than the misalignment. The recommendation made was for a 0.1degrees 3σ RINU and 0.5 degrees 3σ RGA misalignment. Wedge angle, over load indicators, was the driver for the recommendation. This was consistent with Odette's reasoning, but Odette made a recommendation for constraining the sensor misalignment to less than 0.07 degrees 3σ in pitch and 0.04 degrees 3σ.

Dukeman's paper, Analysis of Ares I Sensitivity to Sensor-to-Body Axes Uncertainty was conducted in MAVERIC. Nominal runs were made in which the Inertial-to-Body attitude quaternion was misaligned by a fixed rotation in pitch and yaw. The misalignment was applied after the propagation of the navigation solution. The measurement rates were not misaligned. Results from this analysis paint a slightly different picture than the previous two. The conclusion stated that the physical misalignment of the RINU with respect to the vehicle body frame would have very little effect on overall vehicle performance. Slightly higher values of wedge angle at insertions, propellant consumption, and structural loading were observed. Dukeman concluded that misalignment of up to 1 degree in pitch and yaw would not drastically impact performance in the presence of other dispersions.

4.3.1.1 Analysis Methods

The assumed methods of the previous 3 analyses are described mathematically in brief. For the analysis described in the GN&C SDD, the sensors were assumed perfect except for the misalignment. The nominal transformation between the Body and Sensor frames was assumed identity. The misalignment, Equation (4.12) was applied in the construction of the true sensor measurements prior to the propagation of the navigation solution. The S' Frame is the misaligned sensor frame.

$$\left[C_S^{S'}\right] = \begin{bmatrix} 1 & 0 & 0 \\ 0 & \cos\delta\phi & \sin\delta\phi \\ 0 & -\sin\delta\phi & \cos\delta\phi \end{bmatrix} \begin{bmatrix} \cos\delta\theta & 0 & -\sin\delta\theta \\ 0 & 1 & 0 \\ \sin\delta\theta & 0 & \cos\delta\theta \end{bmatrix} \begin{bmatrix} \cos\delta\psi & \sin\delta\psi & 0 \\ -\sin\delta\psi & \cos\delta\psi & 0 \\ 0 & 0 & 1 \end{bmatrix} \tag{4.12}$$

$$\omega^{S'} = \left[C_S^{S'}\right]\left[C_B^S\right]\left[\omega^B\right]_{True} \tag{4.13}$$

$$a^{S'} = a^S = \left[C_B^S\right]\left(a^B + \left[\omega^B\right]_{True} \times \left(\left[\omega^B\right]_{True} \times \vec{r}_B^S\right)\right) \tag{4.14}$$

The navigation differential equations are given as Equation (4.15), (4.16), and (4.17) with respect to the Inertial Frame, I.

$$\dot{q}_S^I = \frac{1}{2} q_S^I \begin{bmatrix} \vec{\omega}^S \\ 0 \end{bmatrix} \tag{4.15}$$

$$\dot{\vec{V}}^I = q_S^I \circ a^S + g^I \tag{4.16}$$

$$\dot{\vec{P}}^I = \dot{\vec{V}}^I \tag{4.17}$$

The result of the integration of $\omega^{S'}$ is a corrupt navigation state, misaligned inertial to body attitude quaternion, and misaligned sensor measurement. In the error equations, Equation (4.18), (4.19), and (4.20), the quaternion $q_S^{S'}$ is the quaternion form of the direction cosines matrix $[C_S^{S'}]$. The position and velocity states are not in error because the misalignment errors were not applied to the accelerometer measurement and there is no significant error coming from the error in attitude due to the incremental error in angular rate.

$$q_I^B = q_I^S \circ q_S^B \circ \delta q_S^B \tag{4.18}$$

$$\vec{\omega}^{S'} = \vec{\omega}^S + \delta\vec{\omega}^S = \left[C_S^{S'}\right] \left[C_B^S\right] \left[\omega^B\right]_{True} \tag{4.19}$$

$$\vec{a}^S = \left[\delta C_S^B\right] \left[C_S^B\right] \left[\vec{\omega}^S\right]_{True} \tag{4.20}$$

The quantity δq_S^B is the incremental attitude error due to the perturbed rates in Equation (4.18). The quantity $\left[\delta C_S^B\right]$ is the direction cosine matrix formulation of this rotation error.

In the second study conducted by Odette, a similar method was used to simulate the INS misalignment. The result was an error in the initial sensor to inertial frame alignment. The primary difference from the analysis in the GN&C SDD is that Odette chose to induce an error in the initial attitude solution and the acceleration measurements in addition to the angular rates. Equation (4.21), (4.22), and (4.23) describe the resultant error on the attitude, angular rates, and acceleration.

$$q_I^B = q_I^N \circ q_N^B = q_I^S \circ q_S^B \circ q_S^{S'} \tag{4.21}$$

$$\vec{\omega}^{S} = \left[C_{S}^{S'}\right]\left[C_{B}^{S}\right]\left[\omega^{B}\right]_{True} \tag{4.22}$$

$$\vec{a}^{S} = \left[C_{S}^{S'}\right]\left[C_{S}^{B}\right]\left[\vec{\omega}^{S}\right]_{True} \tag{4.23}$$

With the error in the attitude, Equation (4.21), the effect on position and velocity would be significant for reasonable mounting misalignment specifications due to the relationship described in Equation (4.16) and subsequently in Equation (4.17). This error is akin to an an initial alignment error resulting from estimation error in gyrocompassing and is more representative of an inertial frame to navigation frame misalignment.

Dukeman, in his paper, agreed with this rational. He chose to better represent the system by adding error to the angular rates and acceleration measurements after the navigation solution had been propagated. The inertial navigation process remained free of corruption from the misalignment. Equation (4.24) describes the navigation frame to sensor frame misalignment. Equation (4.25) describes the misaligned body frame used in the computation of the body angular rates and accelerations for use by the Controls and Guidance sub-systems.

$$q_{I}^{B} = q_{I}^{N} \circ q_{N}^{B} = q_{I}^{S} \tag{4.24}$$

$$q_{S}^{B} = (q_{S}^{S'})^{-1} \circ q_{S}^{B} \tag{4.25}$$

Dukeman's method and reasoning were chosen as the proper method of simulating the physical misalignment of the inertial hardware. Upon completion and verification of the code changes in MAVERIC, a coarse parameter study was conducted to better understand the design space and the effect of the sensor to body misalignment on vehicle performance. From the previous analyses reviewed, wedge angle and the load indicator, $Q\alpha_{Total}$, were identified as the performance parameters in which the misalignment error would most likely manifest. The load indicator, $Q\alpha_{Total}$, is the product of the dynamic pressure and the combination of the aerodynamic angles α and β, angle of attack and side slip angle. These parameters, among others, were chosen to weigh the effect of the sensor to body misalignment. It is important to note that the analysis was conducted with a vehicle that did not include load-relief or anti-drift logic in the controller. These algorithms are designed specifically to remove biases in the steering commands with respect to the relative wind. It is likely that this mounting misalignment would appear like a steering command bias to the controller.

4.3.1.2 Misalignment Coarse Parameter Study

The coarse parameter study was the first of a series of three analyses conducted to assess the impact of the sensor to body misalignment. The analyses consisted of a coarse parameter study, a fine parameter study, and a Monte Carlo analysis. The analyses were run in MAVERIC with an additional misalignment model. For the parameter studies, a nominal Ares I vehicle was used in a Light/Fast configuration on an ISS trajectory with February mean-monthly wind dispersions. This case was chosen because the trajectory was known to exhibit higher values of $Q\alpha_{Total}$ and because it was used by Dukeman in his analysis.

For the coarse analysis, the sensor was misaligned with respect to the vehicle body in pitch, yaw, and roll. The trajectory was run without dispersions with a mean sensor to body misalignment applied. Values of misalignment in pitch, yaw, and roll were varied for subsequent runs. Misalignment errors in yaw and pitch were varied from -4 degrees to 4 degrees in 1 degree increments and -1 degree to 1 degree in 1 degree increments for roll resulting in a total of 243 cases in the coarse parameter study.

Figures 4.20, 4.21, 4.22, and 4.23 shows the results of the coarse parameter study for 0 degrees roll misalignment. It was found that the errors due to misalignment in roll showed negligible impact compared to the error due to misalignment in pitch and yaw.

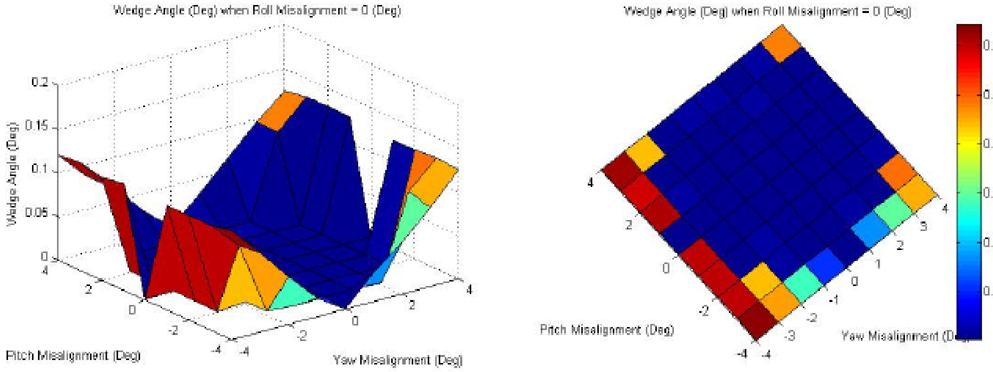

Figure 4.20

Misalignment Coarse Parameter Study: Wedge Angle

The wedge angle is relatively mild within an approximately 3.5 degree radius of the nominal origin. The radius represents a linear combination of pitch and yaw misalignment. It is speculated that the drastic peaks in the outer edge of the parameter study are due to transient events, e.g. the vehicle reaches the target semi-major axis before it is able to correct for the misalignment, the vehicle reaches minimum propellant prior to insertion, etc. Similar to wedge angle, little effect was seen within the interior of the remaining propellant figures.

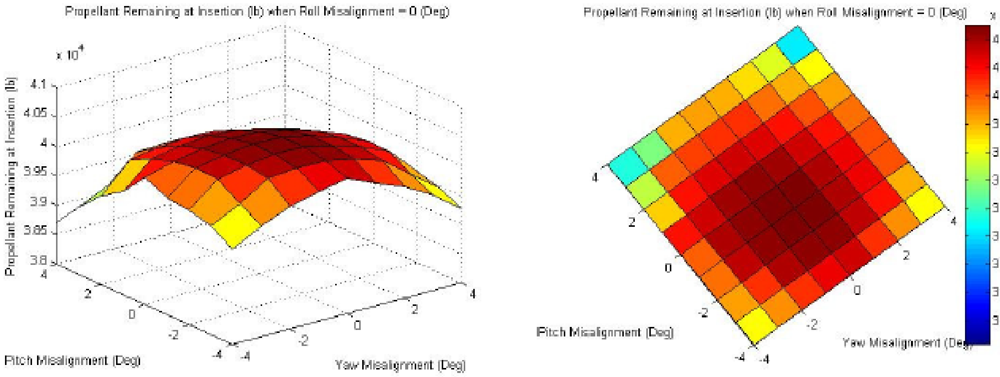

Figure 4.21

Misalignment Coarse Parameter Study: Propellant Remaining

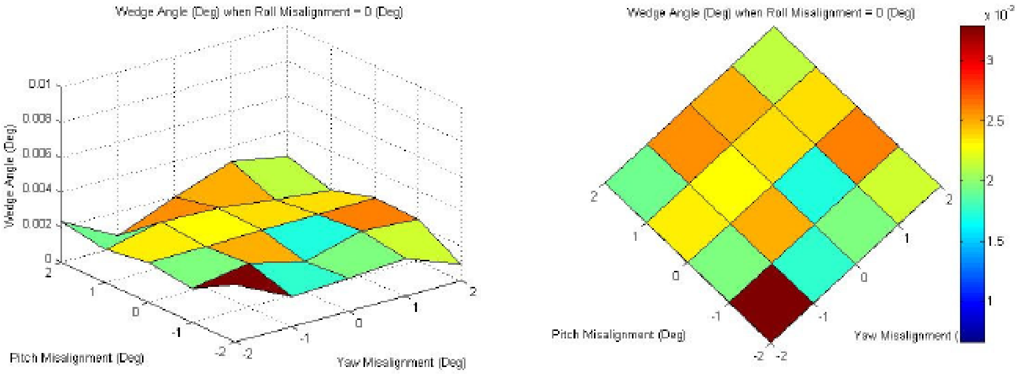

Figure 4.22

Misalignment Coarse Parameter Study: Wedge Angle Close-Up

Figure 4.22 depicts the wedge angle for pitch and yaw misalignment between -2 and 2 degrees. The effect of the misalignment on wedge angle is relatively mild as compared to the contribution of the initial navigation alignment errors. This directly contradicts the results of the first two analyses reviewed.

From the coarse parameter study, it was determined that the sensor to body misalignment primarily manifest as increased $Q\alpha_{Total}$. The load indicator became the primary measure of merit for subsequent analyses.

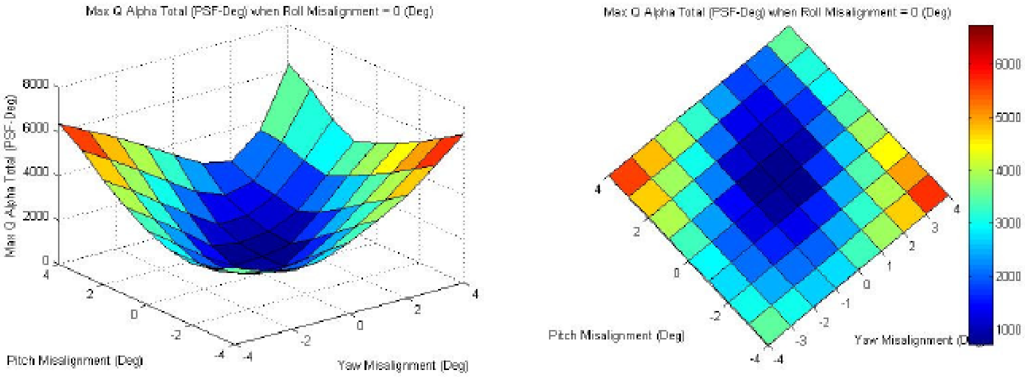

Figure 4.23

Misalignment Coarse Parameter Study: $Q\alpha_{Total}$

4.3.1.3 Misalignment Fine Parameter Study

For the fine analysis, the sensor was misaligned with respect to the vehicle body in pitch, yaw, and roll. The study was conducted similarly to the coarse parameter study, but with a smaller range and a finer grid. The study focused on pitch and yaw because the Coarse Misalignment study showed a lack of sensitivity in roll. Misalignment in yaw and pitch was varied from -2 degrees to 2 degrees in 0.2 degree increments and -1 degree to 1 degree in 1 degree increments for roll resulting in a total of 1323 cases in the fine parameter study. For brevity, only $Q\alpha_{Total}$ for the cases when roll misalignment is 0 degrees is presented in Figure 4.24 and 4.25.

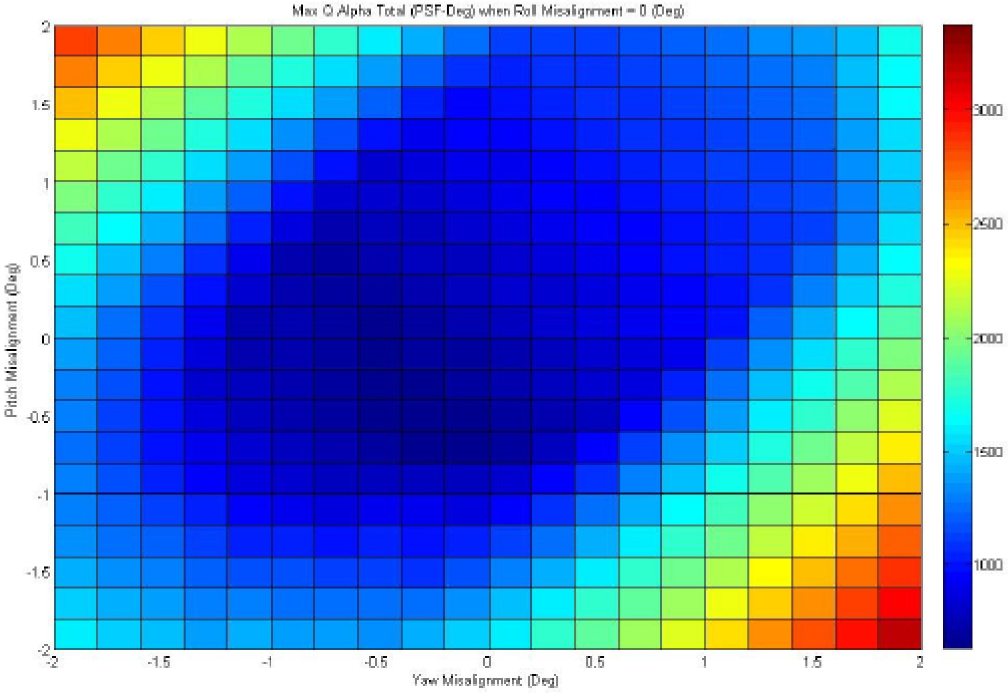

Figure 4.24

Misalignment Fine Parameter Study: $Q\alpha_{Total}$

A design criteria of 200 PSF-Deg increase in $Q\alpha_{Total}$ due to sensor to body misalignment was set as an upper bound for vehicle performance. This constraint was determined from predicted vehicle loading and structural design considerations. Figure 4.24 was re-produced emphasizing the acceptable increase in the scale and legend; the result is shown as Figure 4.25.

In Figure 4.25, a marker has been placed at the origin representing $Q\alpha_{Total}$ with no sensor to body misalignment. The circle was drawn about the origin as a guide for the following dispersion analysis. The radius of the circle represents a 3-sigma dispersion on the sensor to body misalignment of approximately 0.8 degrees in combined pitch and yaw.

Following the fine parameter study, a dispersion analysis was run in MAVERIC, with the misalignment model, to determine the effect of the 0.8 degree (3-sigma) uncertainty on vehicle performance in the presence of all other dispersed parameters. A set of 2000 dispersed cases were run for this study. The sensor to body misalignment was specified as 3 Euler angles each normally dispersed about 0.0 degrees with a 0.2667 degree standard deviation (0.8 degrees 3-sigma). Figure 4.26 shows time histories at the end of the trajectory from the Monte Carlo analysis. Table 4.10 describes the actual statistics for the implemented misalignment in terms of mean and standard deviation for the simulated runs.

Table 4.10

Misalignment Dispersion Analysis Statistics

Statistic	Body X (Deg)	Body Y (Deg)	Body Z (Deg)
Mean Sensor to Body Misalignment	-0.002557	-0.007680	0.003797
1σ Sensor to Body Misalignment	0.266497	0.261825	0.266120
3σ Sensor to Body Misalignment	0.799492	0.785476	0.798359

	Total Angle (Deg)
Mean Pitch and Yaw Misalignment Radius	0.330042
1σ Pitch and Yaw Misalignment Radius	0.174537
1σ Pitch and Yaw Misalignment Radius	0.523612
Mean + 3σ Pitch and Yaw Misalignment Radius	0.853654

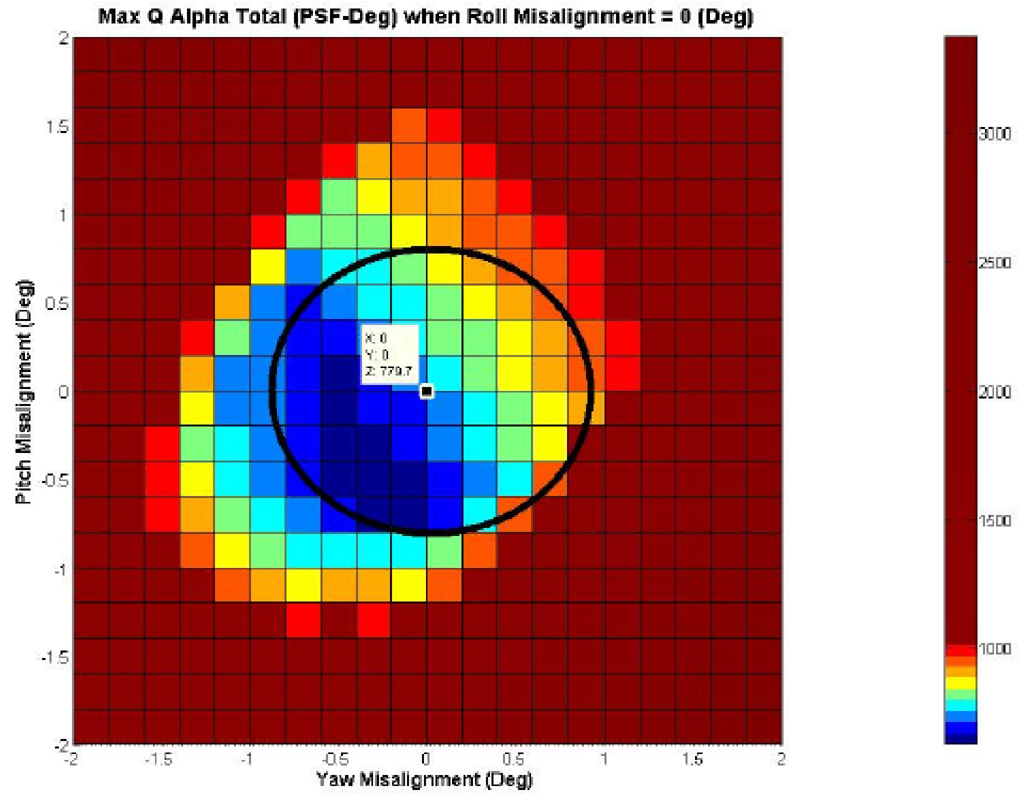

Figure 4.25

Misalignment Fine Parameter Study: $Q\alpha_{Total}$ Limit

For the magnitude of misalignment simulated in the Monte Carlo analysis, the effect of the sensor to body misalignment as seen on wedge angle and propellant remaining is small. The effect on the load indicator can be seen in Figure 4.27. An additional data set was plotted in Figure 4.27 representing a nominal run with a sensor to body misalignment equal to the 1σ values used in the dispersion analysis. The nominal with 1σ sensor to body misalignment was included in the figure to illustrate the difference in the effect on $Q\alpha_{Total}$ seen in the nominal runs of the parameter studies and that of the dispersed runs of the Monte Carlo analysis. Figure 4.28 is a similar plot of $Q\alpha_{Total}$ from an unmodified simulation and has been included for reference and comparison. There is little difference between the plots.

4.3.1.4 Ares I Misalignment Study Conclusion

The results from the dispersion analysis were somewhat unexpected. It was expected that the 0.8 degree 3σ sensor to body misalignment would increase the value of the load indicator at maximum dynamic pressure by more than 1 PSF-degrees from the unmodified dispersed set. It was reasoned that the load indicator is dominated by other dispersions. The statistical combination of the sensor to body misalignment and the other larger error sources results in much less impact than originally anticipated or predicted by the previous analyses. Note the difference in the Mean + 3σ line and the Nominal + 3σ line in Figure 4.27. The Mean + 3σ represents the three sigma result of the dispersion analysis, while the Nominal + 3σ line represents the effect of the sensor to body misalignment only.

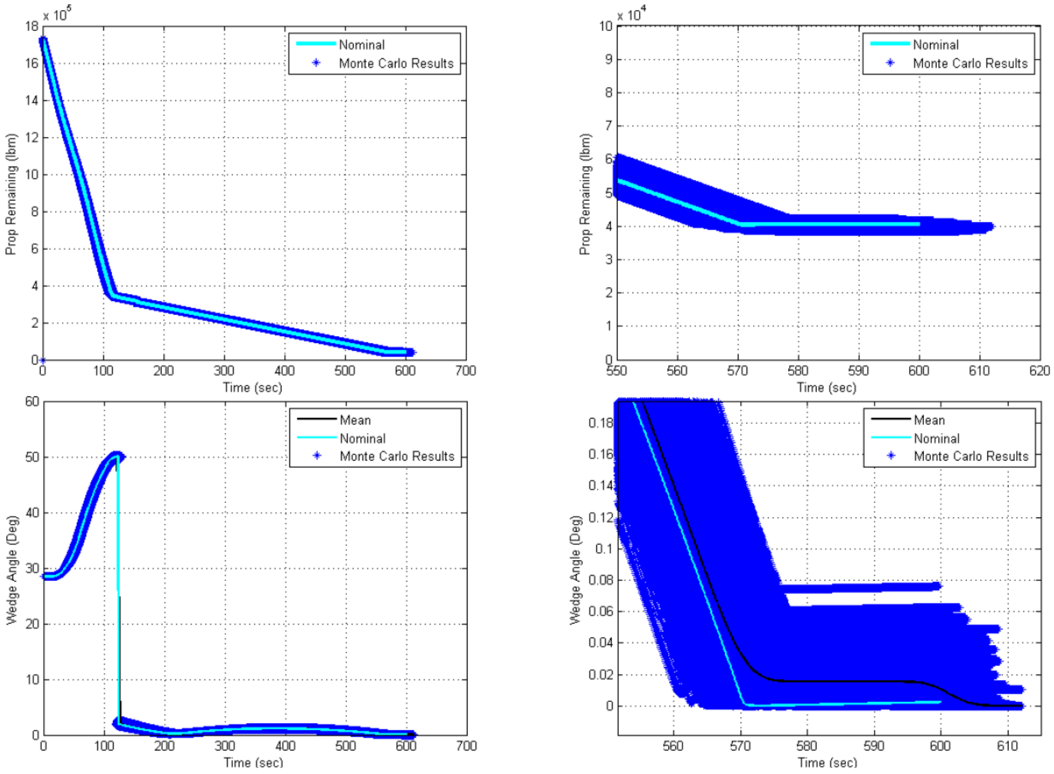

Figure 4.26

Misalignment Dispersion Analysis

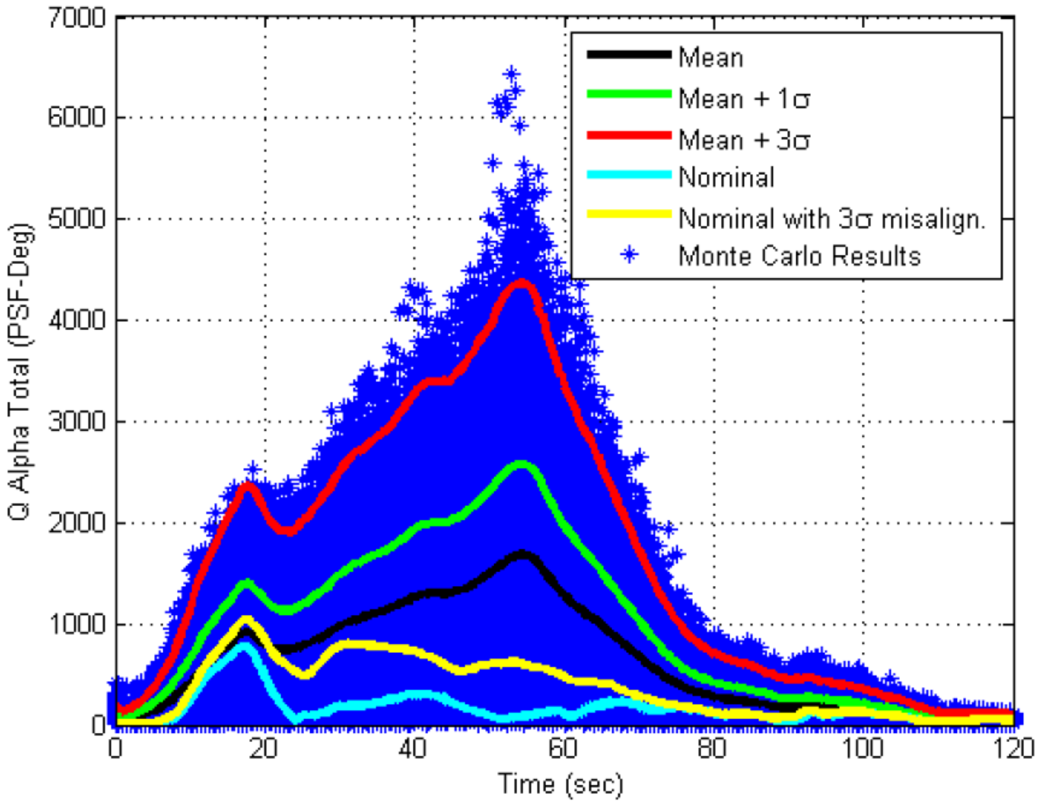

Figure 4.27

Misalignment Dispersion Analysis: $Q\alpha_{Total}$

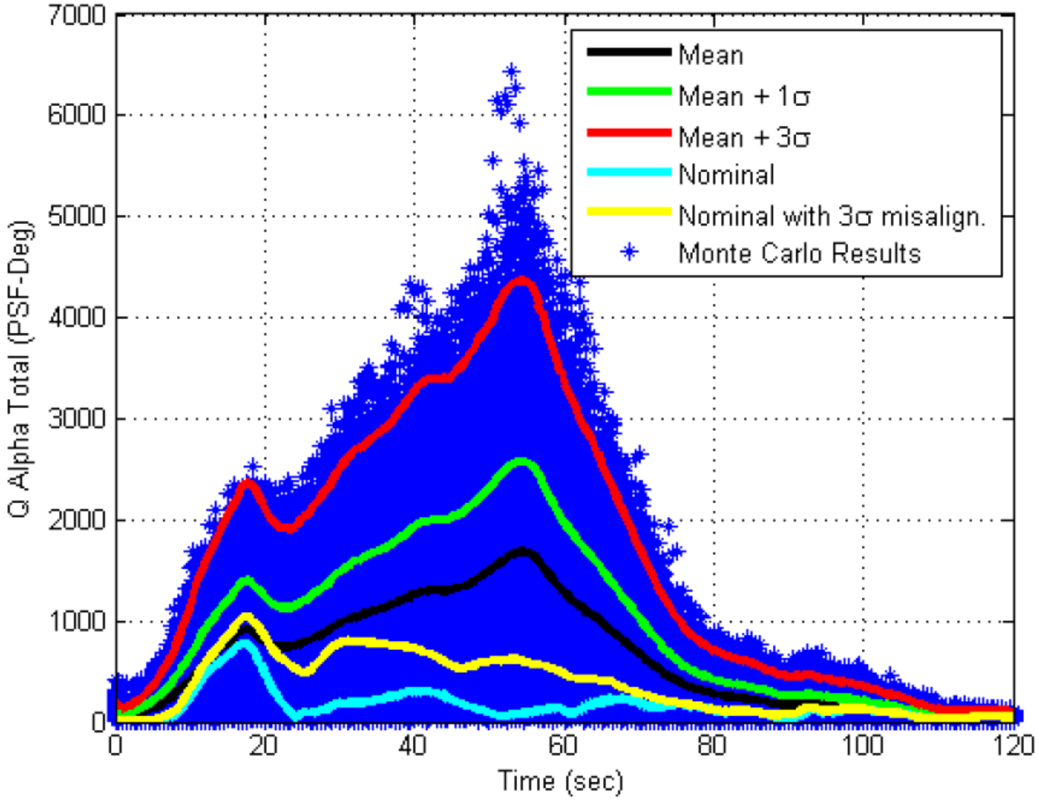

Figure 4.28

Unmodified Dispersion Analysis: $Q\alpha_{Total}$

The dispersed winds are the primary driver of the load indicator. In the correlation matrix associated with the simulation without the misalignments, the primary contributing dispersion to the load indicator is listed as none. This is due to wind dispersions not being included in the correlation analysis. This reveals that the flight day uncertainties do not greatly affect the maximum load indicator. The parameter $Q\alpha_{Total}$ is driven by wind dispersions.

From the Monte Carlo analysis, it can be concluded that a sensor to body misalignment of 0.8 degrees (3σ) in roll, pitch, and yaw is tolerable with near negligible impact on loading and wedge angle within the context of the analysis. It is possible that larger sensor to body misalignment could be shown, with analysis, to behave similarly with near negligible impact on loading and wedge angle.

4.3.2 SLS Misalignment Study

At the beginning of SLS development, Ares I misalignment requirements were carried over into preliminary SLS design. Working from the results and conclusions made during the Ares I misalignment study, a new study was initiated for an SLS vehicle. The Ares I experience showed that a parameter study would likely be inadequate. A new analysis methodology was developed. The approach would only consider dispersed trajectories with wind dispersions. A large Monte Carlo set was set up in which large, uniformly distributed dispersions on sensor misalignment errors would be used. The expectation was that large dispersions over a large number of statistically varied runs would yield insight into the sensitivity of specific vehicle parameters to sensor misalignment over the range of misalignment. The initial plan called for a 10,000 run Monte Carlo set. A five degree uniformly distributed misalignment dispersion was applied to the sensors, Figure 4.29. One major design difference between the controller used in the Ares I analysis and the controller used in this SLS analysis is the incorporation of load relief and anti-drift logic. The purpose of these algorithms is to remove, or trim the vehicle for, slowly varying biases in the attitude error due to winds in an effort to reduce $Q\alpha_{Total}$. It was thought that the sensor misalignment could manifest as such a bias to the controller although this was not conclusively determined to be the case.

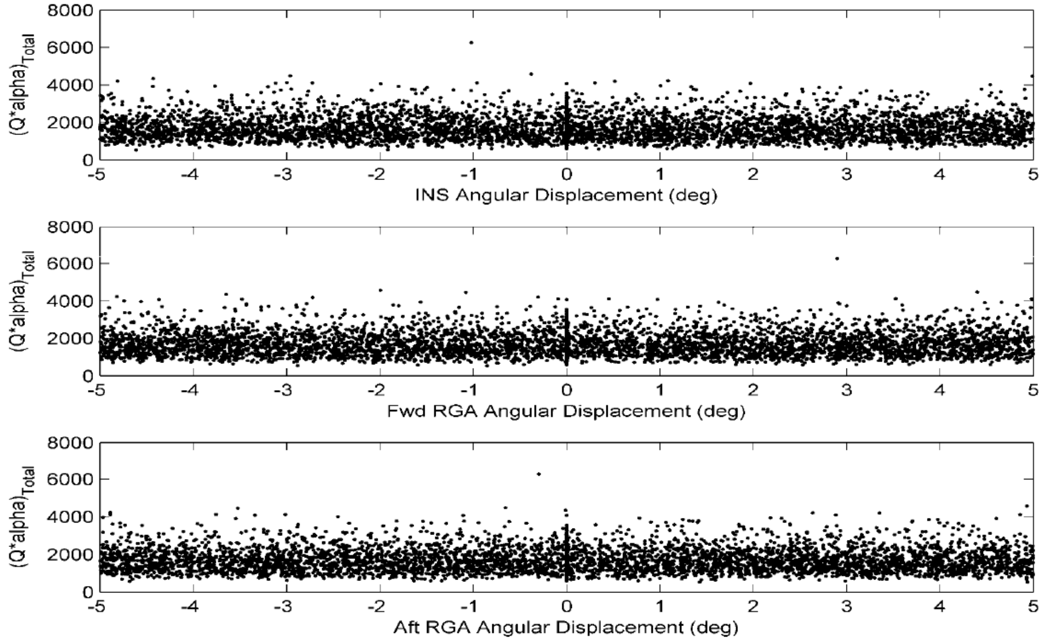

Figure 4.29

SLS Misalignment Study: Sensor Misalignment Dispersions

If the misalignment was uniformly distributed, this would yield statistically significant sub-sets of 1000 runs for each degree of misalignment. All non-sensor misalignment errors were removed in an effort to accurately control and account for the misalignment dispersions applied without having to consider the statistical combination of misalignment in vehicle stacking and actuators. A consequence of reconfiguring the dispersions with lumped misalignment dispersions was that effects driven by interactions between multiple misalignment sources, if they existed, would not be captured. Due to the size of the data sets being analyzed and given the results from the Ares I study, a smaller set of parameters was chosen for examination. The list consisted of vehicle load indicators, engine gimbal angles, controller attitude errors, and controller rate errors. It was understood that this method does not alone represent a complete misalignment study. The object was to identify sensitivities and possibly identify a bound for allowable attitude error for effective control to be used in the allocation of misalignment to individual contributors.

The primary parameter of interest was the load indicator, $Q\alpha_{Total}$. As with Ares I, the angular measurements from each sensor are blended in front of the controller to better approximate the rigid body angular rates in the presence of flexible body dynamics.[31] The expectation was that an apparent trend would emerge with respect to misalignment when the maximum $Q\alpha_{Total}$ values were plotted against the effective misalignment, considering rate blending. The scatter plot of maximum load indicators per run over First Stage (FS) flight is shown in Figure 4.30.

Figure 4.30 did not depict the expected result. Something similar to a uniformly distributed mass of points may have indicated a dominant correlation to the uniformly dis-

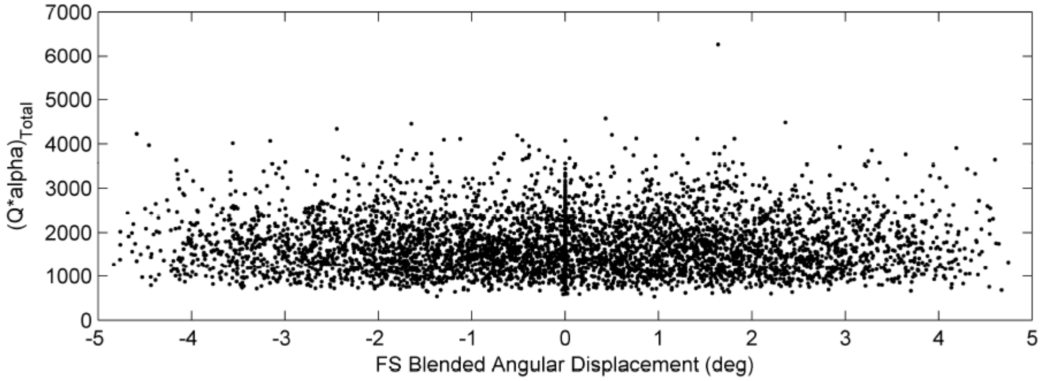

Figure 4.30

SLS Misalignment Study: $Q\alpha_{Total}$ versus Blended Misalignment, Scatter

tributed misalignment errors even though the blending would have softened the distribution to appear more normal. A bucket in the middle of the data may have indicated a strong sensitivity or threshold and could have been used to base a bound for allowable total misalignment. The scatter plot, Figure 4.30, did not show either of these expected characteristics. The seemingly normal distribution of points and the grouping of points at zero was concluded to be an artifact of the statistical combination of the misalignment errors due to the blending.

In an effort to identify the impact of the misalignment on the dispersed trajectories, time history carpet plots were developed for a Monte Carlo case without the misalignment dispersions to compare to the set with the misalignment applied for comparison. Figure 4.31 shows two carpet plots for $Q\alpha_{Total}$ each containing time histories from Monte Carlo runs which differ only in the applied misalignment dispersions. The plot from the simulation with the misalignments is on the right side of Figure 4.31. Only the first 2000 runs are

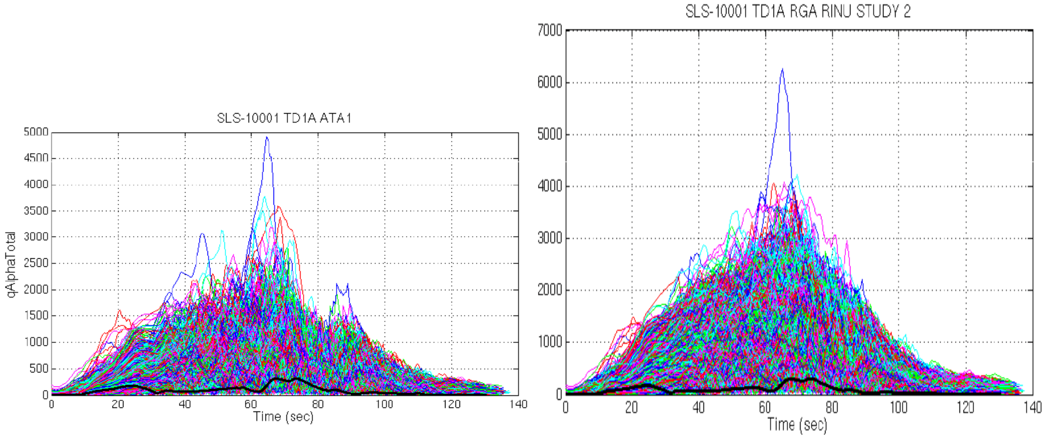

Figure 4.31

SLS Misalignment Study: $Q\alpha_{Total}$ Time Histories Comparison, Carpet

plotted, but the effect of the misalignment dispersion can be seen easily. Excluding the major outlier, the maximums over the sample populations did not increase greatly at the maximum point of dynamic pressure, around 68 seconds into ascent flight. This would indicate that the wind dispersions remains the primary driver of the maximum $Q\alpha_{Total}$. The effect of the misalignment is certainly seen over the rest of the trajectory around the maximums in increased values of $Q\alpha_{Total}$. For the most part, the runs only marginally violated the design limit. For such a large dispersion in misalignment this would indicate that a significant amount of vehicle design margin exists with respect to physical misalignment between the navigation sensors and the actuators, represented as misalignment to vehicle body in the study.

4.3.2.1 Misalignment Summary and Applicability to Aided Inertial Navigation

Contrary to the original assertion during early Ares I development, there is negligible impact to insertion accuracy from physical misalignment. This statement relies on the application of the navigation equations without inclusion of the physical misalignment. For example, as long as the inertial measurements are integrated in the sensor frame or the navigation frame without transfer through a frame with physical misalignment error then the misalignment error will not impact the navigation solution for a system that acquired an initial attitude state through gyrocompassing. This was the case for Ares I and remains the case for SLS. If the initial attitude state is determined by external means, e.g. transfer of an optical alignment, then reason would dictate that the transfer of the alignment be as direct as possible, in terms of number of intermediate transfers, as to exclude relatively large misalignment error from the initial attitude state. For an aided inertial navigation solution, this analysis could be used to bound the attitude accuracy required by the Control subsystem in order to meet mission objectives, thus providing a sizing metric for the inertial portion of the navigation system.

4.4 Insertion Accuracy Trade Study

This section describes a trade study on orbit insertion accuracy for existing inertial hardware. By flying out different inertial instrument specifications and configurations it is possible to assess what may be required for a particular mission. If cost information is available, then it becomes possible to consider hardware cost for accuracy in the trade. Common trajectories are used to properly frame comparisons between different inertial hardware. Multiple Navigation system configurations were simulated to maximize the depth in the trade space. The configurations vary in the method in which the initial alignment is determined and in whether the system is aided by GPS. The configurations may or may not be easily realizable. An example of a configuration that is not easily realizable would be a RINU which is aligned by a method other than gyrocompassing or that is aided by GPS during ascent. At very least, a software modification would be required in order to force an alternative alignment solution. Also, knowledge of the sensor frame to an external frame may not be known well enough to directly support the optical alignment accuracy used. Most of the systems and configurations examined are realizable and could potentially represent a Navigation system design if the accuracy and hardware is a match for the vehicle. The configurations examined are:

- Inertial navigation with initial alignment by gyrocompassing
- Inertial navigation with initial alignment by external optical measurement where applicable
- Inertial navigation with GPS aiding

4.4.1 Insertion Accuracy Reference Trajectories

This section details the Reference Trajectories used in the study. A variety of trajectories were chosen representative of different vehicle configurations and missions. A total of three reference trajectories were simulated for the trade study. There is one Ares I trajectory variant. This trajectory was considered during an official Ares I Design and Analysis Cycle. Figure 4.32 describes the Ares I trajectory. Table 4.11 describes the final state for Reference Trajectory 1. The second reference trajectory is an SLS variant with an upper stage. The simulated vehicle is a SLS Block 2 vehicle. Figure 4.33 describes Reference Trajectory 2, and Table 4.12 describes the insertion state. The third trajectory is for an SLS Block 0 variant. Reference Trajectory 3 is described by Figure 4.34. The insertion state is listed in Table 4.13. The three reference trajectories each feature different vehicle configurations, injection masses, times of flight, and orbit insertion targets.

Table 4.11

Trajectory 1, Ares I Variant, Insertion State

Trajectory Orbit Insertion Parameter	
Flight Time (t_{final})	625.0 s
Semi-Major Axis (a)	3489 nmi
Apogee Altitude (Alt_{apogee})	100.1 nmi
Perigee Altitude ($Alt_{perigee}$)	-10.2 nmi
Orbit Insertion Altitude (Alt_{MECO})	71.7 nmi
Inclination (i)	28.5 deg
Right Ascension of the Ascending Node (RAAN, Ω)	170.0 deg

Table 4.12

Trajectory 2, SLS Variant, Insertion State

Trajectory Orbit Insertion Parameter	
Flight Time (t_{final})	754.48 s
Semi-Major Axis (a)	3486 nmi
Apogee Altitude (Alt_{apogee})	130.1 nmi
Perigee Altitude ($Alt_{perigee}$)	-46.7 nmi
Orbit Insertion Altitude (Alt_{MECO})	77.9 nmi
Inclination (i)	29.0 deg
Right Ascension of the Ascending Node (RAAN, Ω)	169.2 deg

Table 4.13

Trajectory 3, SLS Variant, Insertion State

Trajectory Orbit Insertion Parameter	
Flight Time (t_{final})	517.72 s
Semi-Major Axis (a)	3939.0 nmi
Apogee Altitude (Alt_{apogee})	968 nmi
Perigee Altitude ($Alt_{perigee}$)	21.9 nmi
Orbit Insertion Altitude (Alt_{MECO})	93.2 nmi
Inclination (i)	28.5 deg
Right Ascension of the Ascending Node (RAAN, Ω)	178.5 deg

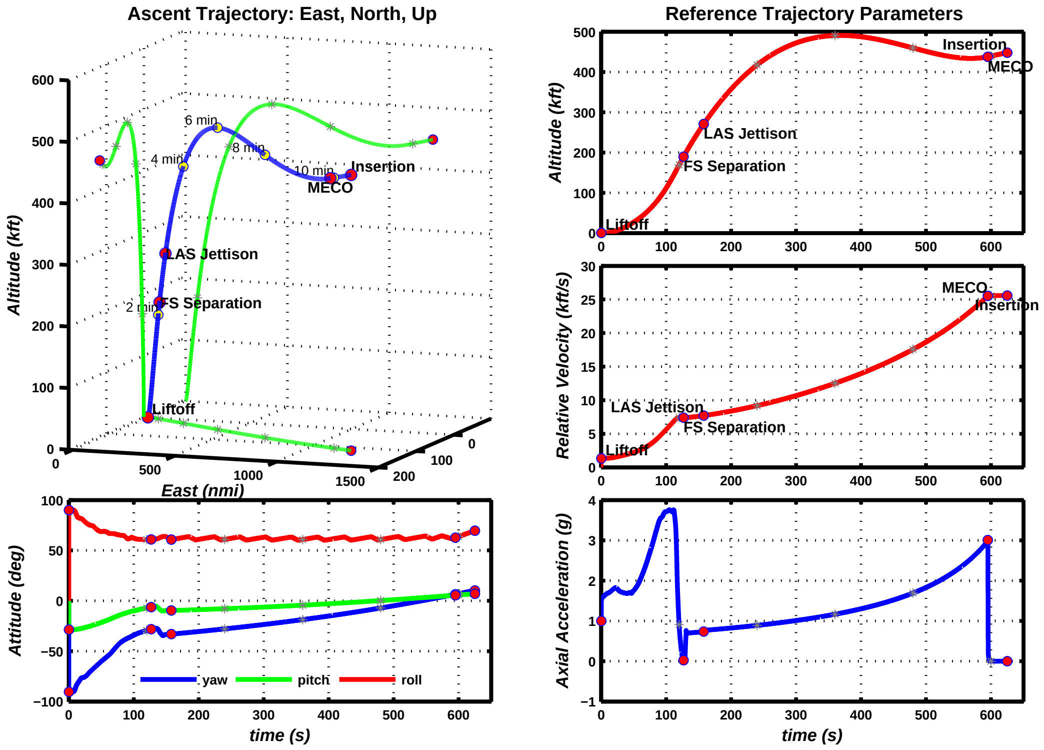

Figure 4.32

Trajectory 1, Ares I Variant

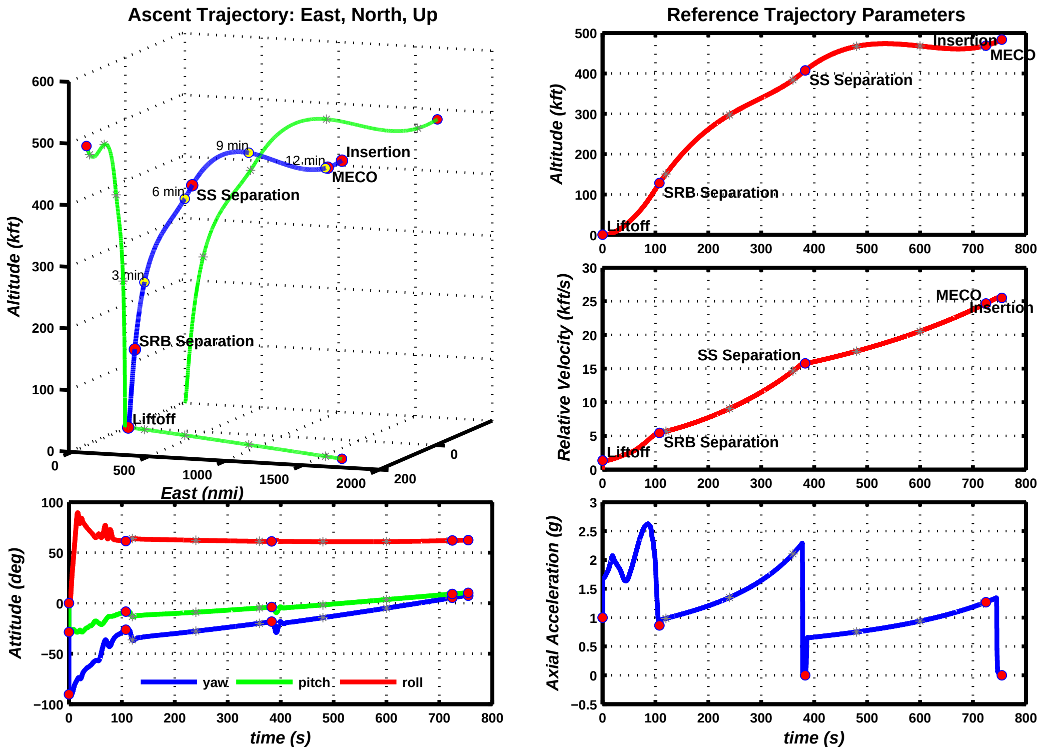

Figure 4.33

Trajectory 2, SLS Variant with Second Stage

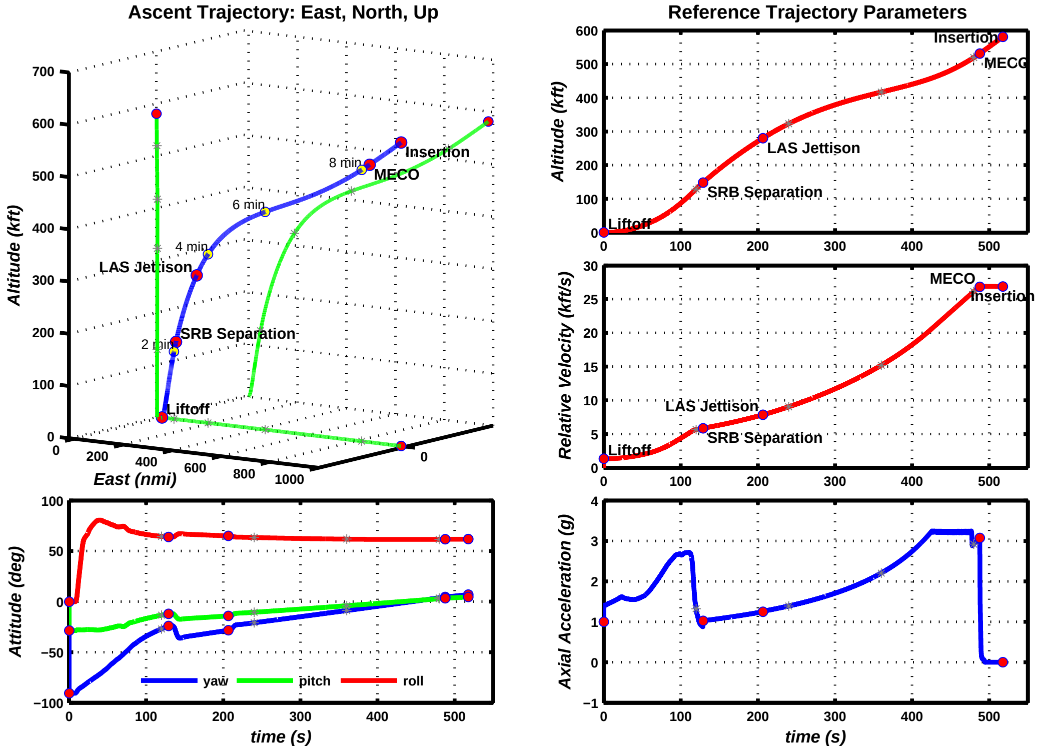

Figure 4.34

Trajectory 3, SLS Variant

4.4.2 Error Budgets

One of the inherent problems with performing a navigation analysis trade that considers actual hardware is that the detailed instrument error budgets for navigation grade inertial hardware are often considered proprietary and are well protected. Some information can be gathered from the vendors' sales brochures or publicly available product specifications, but they commonly leave much to be desired in terms of detail or accuracy of detail over the product line. A formal Request For Information (RFI) to the vendor is a good way to get information; however it is not unheard of that a quoted specifications will change when a vendor comes under contract or receives a Request for Quote (RFQ). This should not be misinterpreted as a dirty trick by the supplier, but rather a method of managing risk and cost associated with instrument qualification. There also seems to be flexibility in instrument specifications within product lines based upon instrument screening.

This section will describe the instrument error budgets used in the trade study. The instruments chosen represent a sample of navigation grade instruments available for purchase at the time of writing. In some cases, the exact error specifications used have been estimated based upon knowledge of the instrumentation used and/or the use of the instruments in other applications. The goal of this study is to get a ballpark estimate for the instrument capability with respect to Ares I and SLS trajectories and insertion accuracy requirements. This should serve as a disclaimer that, although a best effort has been made to estimate the error budgets for the specifically cited inertial instruments, the performance is based upon estimates and may or may not completely represent the cited inertial hardware. It is the hope of the author that these candidates offer a good sample of inertial hardware.

The first candidate for the trade is the Ares I RINU. The RINU is a one fault tolerant strapdown inertial navigation system designed by Honeywell International for use by the Boeing Company on the Ares I Upper Stage Integrated Avionics Contract with NASA originally. The contract to design and manufacture the RINU was extended for the SLS Stages Contract after the cancellation of Ares I. At the time of writing, the RINU design has just passed the Critical Design Review (CDR). The RINU is a high quality strapdown inertial navigation system with excellent gyro bias, gyro noise, and accelerometer noise characteristics. The RINU design was derived from the Fault Tolerant Inertial Navigation Unit (FTINU), also produced by Honeywell International, for use by United Launch Alliance on the Atlas V EELV. The FTINU was also flown on the Constellation program Ares 1-X test flight. The RINU is currently part of the avionics baseline design for SLS. The FTINU is internally redundant at the sensor level featuring 5 independent sensor channels arranged in a pentad configuration each with one 20cm path length GG1320 ring laser gyro and one Honeywell QA3000 accelerometer. This is a clever design which allows for increased system accuracy over the individual component accuracy when not in a fault configuration. Human rating often requires redundancy in avionics, particularly in critical avionics. Being internally fault tolerant is beneficial for human-rated space flight given that multiple boxes can be replaced by the one internally fault tolerant box.[17][86]

The second candidate navigation system for trade is the Space Integrated GPS/INS (SIGI). The SIGI was designed and is produced by Honeywell International. The SIGI is a three axis strapdown inertial navigation system with Tremble Force 19 GPS receiver hardware. The SIGI is capable of producing a GPS position and velocity solution, a GPS aided inertial navigation solution, and an inertial navigation solution independent of the GPS hardware. The SIGI has very good gyro bias and noise characteristics. Being three axis capable, use where human flight rating is required would dictate that multiple boxes be used for redundancy. The SIGI has flown the H-II transfer vehicle, the Japanese Experiment Module (JEM), X-37, and most Launch vehicles from Orbital Sciences. The SIGI GPS solution is used on the ISS and also passively flew on the Space Shuttle without integration into the Shuttle navigation solution. Review of the performance reports for the SIGI GPS accuracy reports for Shuttle show that the SIGI GPS solution was quite accurate compared to the Shuttle Best Estimated Trajectory (BET) despite the reports of issues associated with the use of Common Off The Shelf GPS receivers.[74][57][20]

The third candidate for the trade is the Redundant Inertial Flight Control Assembly (RIFCA). The RIFCA was originally designed and produced by Allied Signals prior to becoming part of by L-3 Communications. The RIFCA is a mixed quality inertial navigation system in that it exhibits excellent gyro noise characteristics but medium quality gyro bias characteristics. The poorer gyro bias performance is somewhat irrelevant given that the RIFCA is likely initially aligned optically by theodolite. The RIFCA is internally triple redundant with six gyro/accelerometer pairs, and it is flown by ULA on all Delta launch vehicles. The RIFCA is similar to RINU in that it uses 20 cm path length ring laser gyros and pendulous accelerometer.[66][70][13][67]

The fourth trade candidate is and LN200S. The LN200 is a tactical grade IMU developed by Litton, now Northrup Grumman. The IMU comes in multiple variants. The LN200S is a space qualified, radiation hardened, version while the LN251 includes an integrated GPS receiver. In terms of what is typically needed for navigation applications, the LN200 has very poor gyro bias and gyro noise characteristics. Multiple units would be required for redundancy. The IMU uses Fiber Optic Gyros and Micro Electro-Mechanical System (MEMS) accelerometers. [38][37][39]

The fifth candidate for the trade is a fictitious IMU, denoted the 1Deg IMU. The IMU was developed to demonstrate the capability of GPS aiding. The IMU specification is based on an LN200 specification with gyro bias and gyro angular walk parameters altered such that the total attitude error during ascent would not exceed one degree. The fictitious unit exhibits poor gyro bias and gyro noise characteristics. Like the LN200, the 1Deg IMU is defined to be a three axis system without redundancy.

The sixth candidate for the trade is the Miniature Inertial Measurement Unit (MIMU). The MIMU is popular for space applications and is targeted for the satellite and spacecraft market. The MIMU is small, lightweight, and radiation hardened. The IMUs used by the Orion Crew Exploration Vehicle, referred to as the Orion Inertial Measurement Unit (OIMU), are derived from the MIMU. The MIMU features very good gyro bias and noise characteristics. The OIMU includes gyros and accelerometers which are very similar to those used in the RINU. Being a three axis IMU, multiple units would be required for redundancy. Among many, a few of the missions flown with the MIMU include the Mars Reconnaissance Orbiter (LRO), the Mars Reconnaissance Orbiter (MRO), and New Horizons.[44][41]

The seventh and last candidate for the trade is the LN100 and LN100LG. The LN100 is a three-axis navigation grade IMU originally designed and produced by Litton and now produced by Northrop Grumman. The LN100LG is the INS variant which includes an optional Tremble Force 5 GPS receiver and produces a full navigation solution in addition to angular rate and specific force measurement data. The LN100 exhibits excellent gyro bias and noise characteristics. The LN100 was flown on a myriad of Orbital Sciences Launch vehicle before being replaced by the Honeywell produced SIGI. The LN100 is used in a variety of other commercial application. One of the key features of the LN100 is the use of patented Zero-Lock ring laser gyros which do not require mechanical dithering to avoid the lock-in effect common in ring laser gyros. The claim of this technology is that the output noise can be greatly reduced. If redundancy is required, multiple boxes would be needed.[36][41][28]

There is a variable amount of confidence in the accuracy of the specifications used. The RINU is simulated as it was specified by the author for SLS. The RINU design is known to a fidelity required for detailed design. The SIGI, RIFCA, LN100, and LN200 specifications are known but with less understanding than would be required for detailed design. The MIMU specification is defined based upon the understanding of the OIMU and from product brochures. The 1Deg IMU is fictitious. The error budgets for the candidates would vary based upon application specific environments and along the product line. Each of the error budgets used is assumed to be adequately known for the purpose of the inertial hardware trade.

4.4.3 Predicted Alignment Capability

Each of the inertial hardware boxes entertained for the trade study differs in instrument specification. As previously considered in the sensitivity study, the ability of the inertial hardware to align through gyrocompassing is primarily a function of the quality of the gyros utilized by the system. The accuracy to which the inertial hardware is capable of aligning is independent of the trajectory that it will subsequently fly out.

In this study, each instrument was gyrocompassed for 20 minutes in a benign pre-launch environment. The filter utilized is a 6-state Kalman filter with states for velocity and attitude. The filter utilizes zero velocity updates and is initialized by a deterministic coarse alignment algorithm for 100 seconds prior to 1100 seconds of fine alignment. The filter was conservatively tuned. Better performance could potentially be achieved if the filter was re-tuned for each instrument. The statistics for achieved alignment accuracy are presented in Table 4.14 in terms of initial heading error and initial leveling error. A 500 run Monte Carlo analysis was performed for each instrument to develop the alignment accuracy statistics.

The RINU and the LN100LG estimates show the best initial alignment accuracy due to superior gyro bias and gyro noise characteristics. The SIGI and MIMU are not far behind. This shows the SIGI to be an excellent inertial navigation system, even without consideration of the embedded GPS receiver. The azimuth alignment capability of the RIFCA is very poor at approximately 4.3 degrees 3σ. This calls in to question the orbit insertion accuracy numbers listed in the Delta IV payload planners guide until the possibility of external alignment aids are considered. Similar to the RIFCA, the simulated initial align-

Table 4.14

Inertial Instrument Trade Study, Gyrocompass Alignment Capability

Inertial Hardware	Heading Error (1σ)	Leveling Error (1σ)
Ares I RINU	87.7 arcsec	5.94 arcsec
SIGI	98.1 arcsec	11.3 arcsec
RIFCA	5185 arcsec	17.3 arcsec
LN200S	18273 arcsec	451 arcsec
1Deg IMU	8809 arcsec	157 arcsec
MIMU	118 arcsec	10.0 arcsec
LN100LG	70.0 arcsec	7.85 arcsec

ment result for the LN200S at 15 degrees 3σ, and 1DegIMU at 7.5 degrees 3σ are not well suited for inertial navigation without the use of aiding. The LN200 result likely represents a divergent alignment solution, i.e. failure to align.

4.4.4 Predicted Ascent Accuracy Capability

In this analysis, the trade study inertial instrument candidates were simulated on the reference trajectories. Statistics were developed based on each 500 run Monte Carlo set at orbit insertion. Two special cases were simulated. The RIFCA was initialized by gyrocompassing and also by optical alignment. The optical alignment was estimated from quoted Delta IV out-of-plane insertion accuracy.[13] For the simulated RINU, the initial alignment was developed for a no-fault configuration assuming a symmetric geometry for the sensor pentad. At launch, a fault was simulated which reduced the effective accuracy. This is actually a benefit to RINU performance given that most of the navigation error is developed during alignment. Among the candidate inertial hardware, the RINU is unique in its redundancy management design. There is no known performance sensitivity to a simulated fault for the other candidate systems. Table 4.15 lists the orbit insertion errors for the inertial instruments flown on Reference Trajectory 1, the Ares I variant. The table includes the magnitudes of the navigation state errors and the errors in the Keplerian elements which are indicative of the in-plane orbit error, semi-major axis and radius of apogee. The wedge angle is also listed as a metric for total error out-of-plane. Figures 4.35, 4.36, and 4.37 re-illustrates the insertion accuracy per instrument in term of the full state error, ECI position, ECI velocity, and attitude.

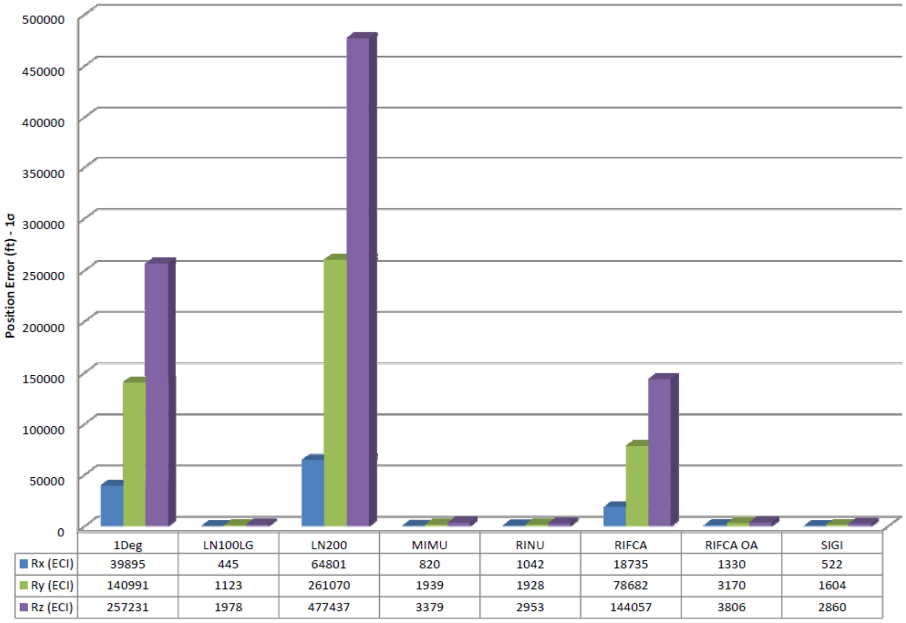

	1Deg	LN100LG	LN200	MIMU	RINU	RIFCA	RIFCA OA	SIGI
🟦 Rx (ECI)	39895	445	64801	820	1042	18735	1330	522
🟩 Ry (ECI)	140991	1123	261070	1939	1928	78682	3170	1604
🟪 Rz (ECI)	257231	1978	477437	3379	2953	144057	3806	2860

Figure 4.35

Inertial Navigation Trade, Position Error at Insertion, Trajectory 1

Data is also presented for the other two reference trajectories considered in the trade study. Table 4.16 lists the orbit insertion errors for the inertial instruments flown on Reference Trajectory 2, the SLS variant with second stage. The position, velocity, and attitude

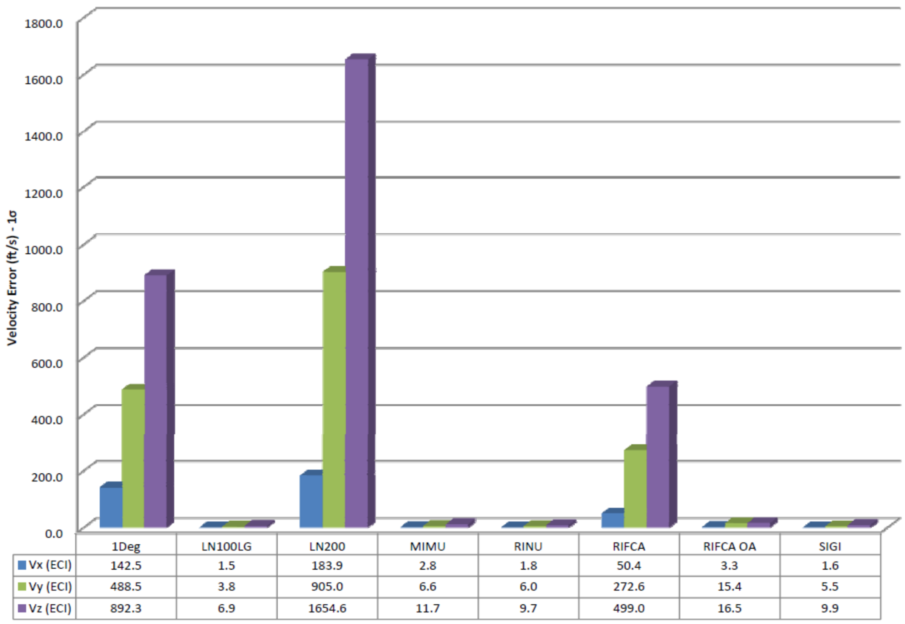

	1Deg	LN100LG	LN200	MIMU	RINU	RIFCA	RIFCA OA	SIGI
🟦 Vx (ECI)	142.5	1.5	183.9	2.8	1.8	50.4	3.3	1.6
🟩 Vy (ECI)	488.5	3.8	905.0	6.6	6.0	272.6	15.4	5.5
🟪 Vz (ECI)	892.3	6.9	1654.6	11.7	9.7	499.0	16.5	9.9

Figure 4.36

Inertial Navigation Trade, Velocity Error at Insertion, Trajectory 1

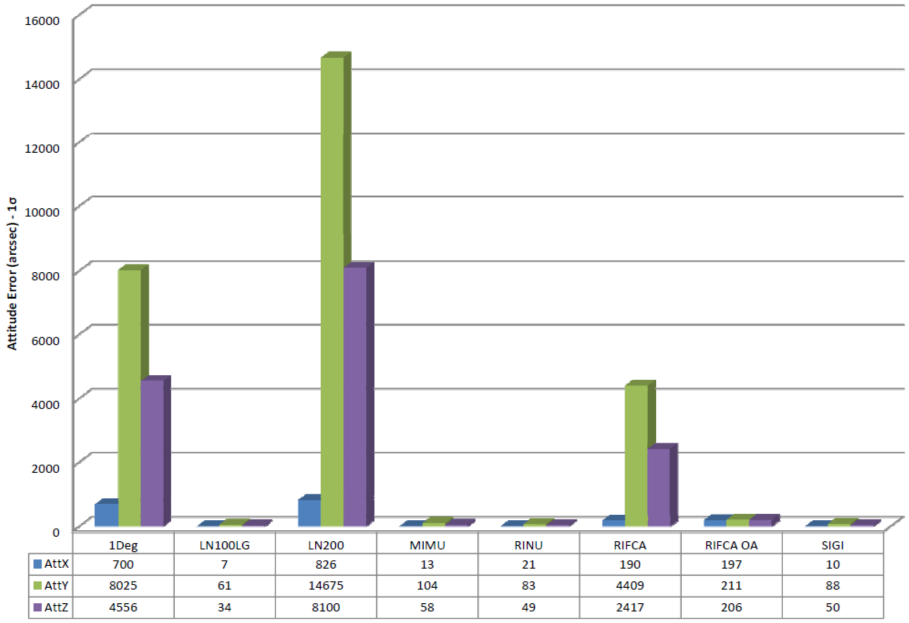

	1Deg	LN100LG	LN200	MIMU	RINU	RIFCA	RIFCA OA	SIGI
🟦 AttX	700	7	826	13	21	190	197	10
🟩 AttY	8025	61	14675	104	83	4409	211	88
🟪 AttZ	4556	34	8100	58	49	2417	206	50

Figure 4.37

Inertial Navigation Trade, Attitude Error at Insertion, Trajectory 1

Table 4.15

Inertial Navigation Trade, Insertion Accuracy Summary, Trajectory 1

	Insertion State Error, 3σ					
	State Error Magnitude			Keplerian Error State		
	$\lvert\delta R_{ECI}\rvert$ (nmi)	$\lvert\delta V_{ECI}\rvert$ (nmi/s)	$\lvert\delta\Theta\rvert$ (arcsec)	δa (nmi)	δR_a (nmi)	$wedge$ (deg)
1Deg IMU	146.2	0.507	27760	32.2	34.0	24
LN100LG	1.144	0.00395	210.6	1.20	1.27	0.577
LN200	270.6	0.936	50340	36.1	36.0	13
MIMU	1.965	0.00679	360.2	2.30	2.45	0.091
RINU	1.816	0.00569	296.8	1.59	1.84	0.074
RIFCA	81.57	0.282	15090	5.17	4.30	3.8
RIFCA Aligned	2.532	0.0112	1065	3.90	3.88	0.11
SIGI	1.639	0.00568	305.3	1.22	1.30	0.08

state errors are plotted in figures 4.38, 4.39, and 4.40. For Reference Trajectory 3, the SLS Block 0 variant, summary state errors are list in Table 4.17, and the position, velocity, and attitude errors are depicted in figures 4.41, 4.42, and 4.43.

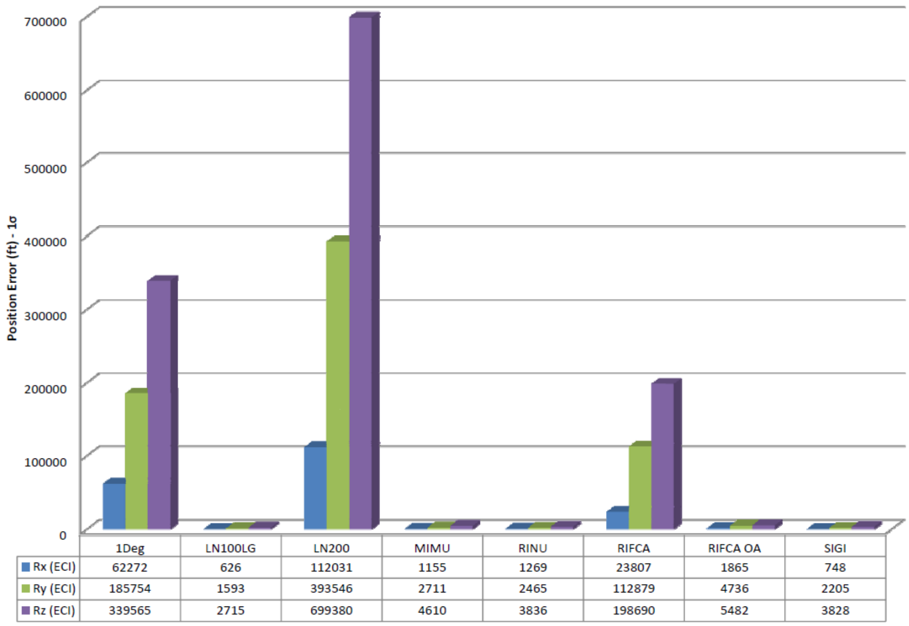

	1Deg	LN100LG	LN200	MIMU	RINU	RIFCA	RIFCA OA	SIGI
■ Rx (ECI)	62272	626	112031	1155	1269	23807	1865	748
■ Ry (ECI)	185754	1593	393546	2711	2465	112879	4736	2205
■ Rz (ECI)	339565	2715	699380	4610	3836	198690	5482	3828

Figure 4.38

Inertial Navigation Trade, Position Error at Insertion, Trajectory 2

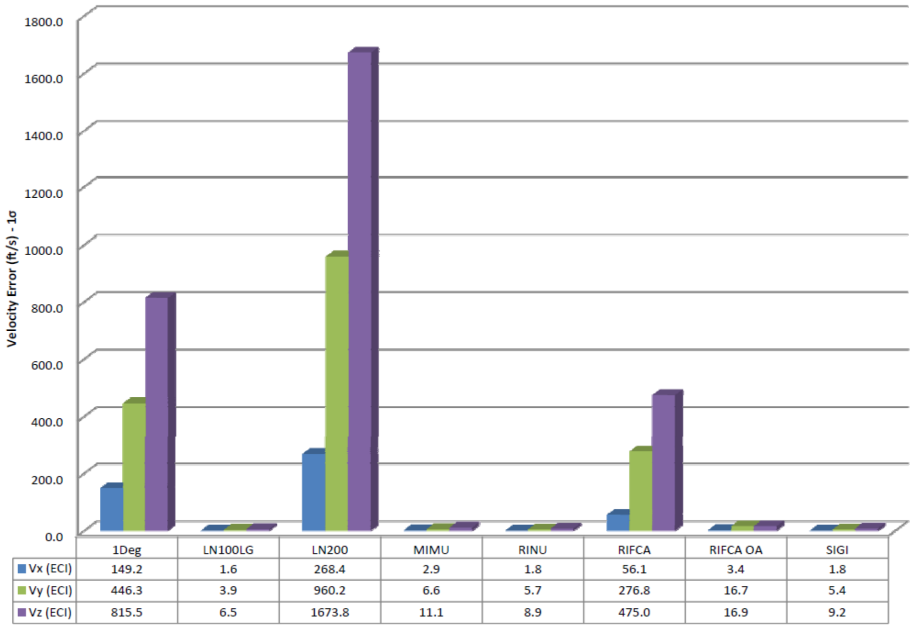

	1Deg	LN100LG	LN200	MIMU	RINU	RIFCA	RIFCA OA	SIGI
■ Vx (ECI)	149.2	1.6	268.4	2.9	1.8	56.1	3.4	1.8
■ Vy (ECI)	446.3	3.9	960.2	6.6	5.7	276.8	16.7	5.4
■ Vz (ECI)	815.5	6.5	1673.8	11.1	8.9	475.0	16.9	9.2

Figure 4.39

Inertial Navigation Trade, Velocity Error at Insertion, Trajectory 2

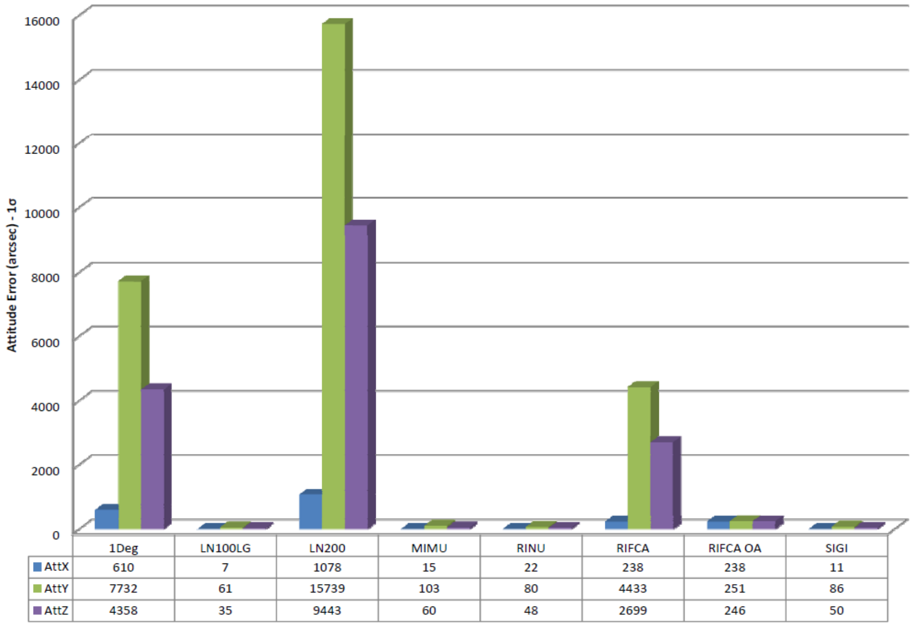

	1Deg	LN100LG	LN200	MIMU	RINU	RIFCA	RIFCA OA	SIGI
■ AttX	610	7	1078	15	22	238	238	11
■ AttY	7732	61	15739	103	80	4433	251	86
■ AttZ	4358	35	9443	60	48	2699	246	50

Figure 4.40

Inertial Navigation Trade, Attitude Error at Insertion, Trajectory 2

Table 4.16

Inertial Navigation Trade, Insertion Accuracy Summary, Trajectory 2

	Insertion State Error, 3σ					
	State Error Magnitude			Keplerian Error State		
	$\lvert\delta R_{ECI}\rvert$ (nmi)	$\lvert\delta V_{ECI}\rvert$ (nmi/s)	$\lvert\delta\Theta\rvert$ (arcsec)	δa (nmi)	δR_a (nmi)	$wedge$ (deg)
1Deg IMU	193.6	0.465	26690	34.6	43.9	17
LN100LG	1.584	0.00382	211.9	1.29	1.60	0.068
LN200	400.1	0.962	55160	46.3	47.0	18.
MIMU	2.701	0.00652	360.4	2.44	3.06	0.11
RINU	2.337	0.00530	286.6	1.707	2.19	0.071
RIFCA	113.4	0.273	15600	6.69	2.81	4.2
RIFCA Aligned	3.694	0.0118	12742	4.61	3.76	0.11
SIGI	2.212	0.0053	300.1	1.36	1.63	0.091

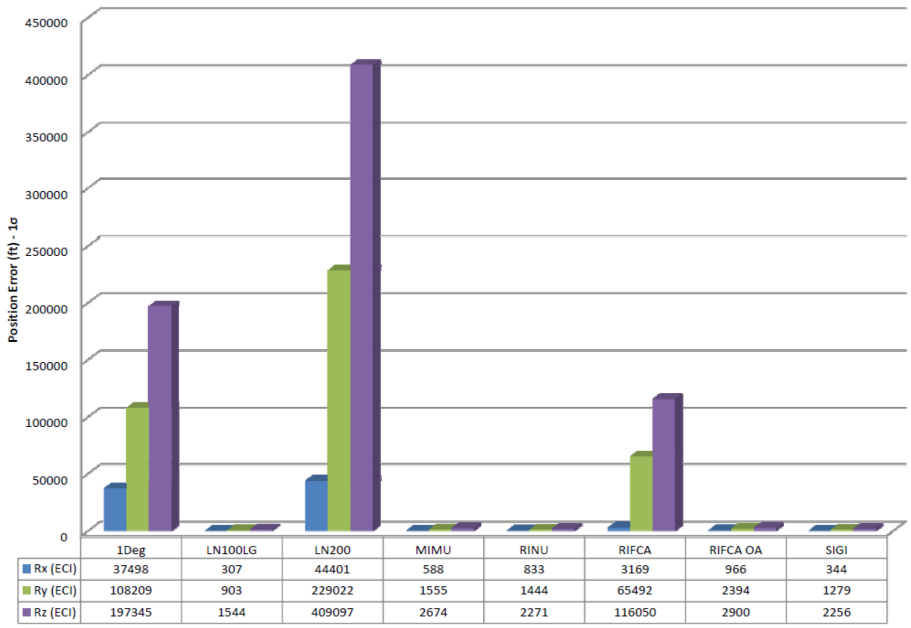

	1Deg	LN100LG	LN200	MIMU	RINU	RIFCA	RIFCA OA	SIGI
■ Rx (ECI)	37498	307	44401	588	833	3169	966	344
■ Ry (ECI)	108209	903	229022	1555	1444	65492	2394	1279
■ Rz (ECI)	197345	1544	409097	2674	2271	116050	2900	2256

Figure 4.41

Inertial Navigation Trade, Position Error at Insertion, Trajectory 3

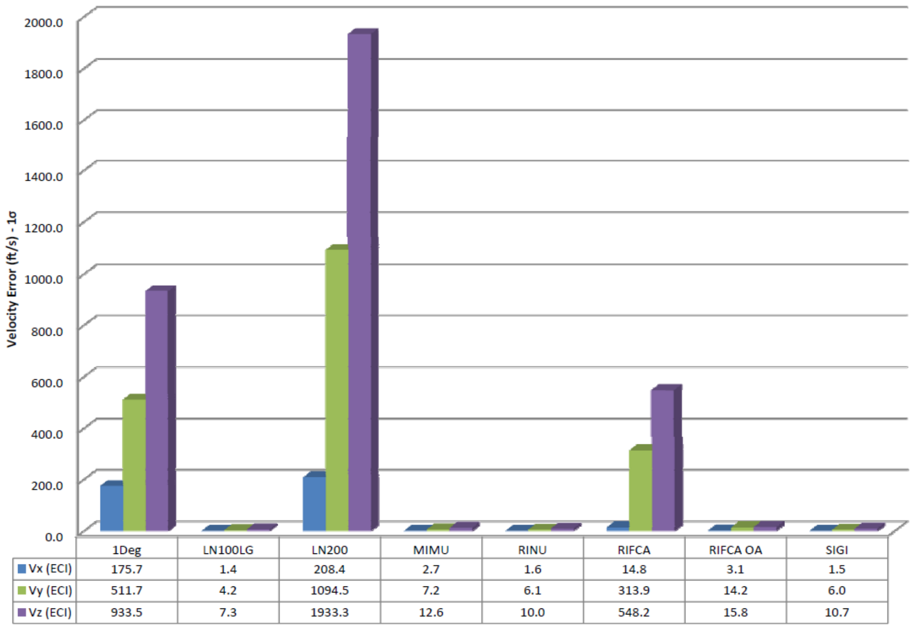

	1Deg	LN100LG	LN200	MIMU	RINU	RIFCA	RIFCA OA	SIGI
■ Vx (ECI)	175.7	1.4	208.4	2.7	1.6	14.8	3.1	1.5
■ Vy (ECI)	511.7	4.2	1094.5	7.2	6.1	313.9	14.2	6.0
■ Vz (ECI)	933.5	7.3	1933.3	12.6	10.0	548.2	15.8	10.7

Figure 4.42

Inertial Navigation Trade, Velocity Error at Insertion, Trajectory 3

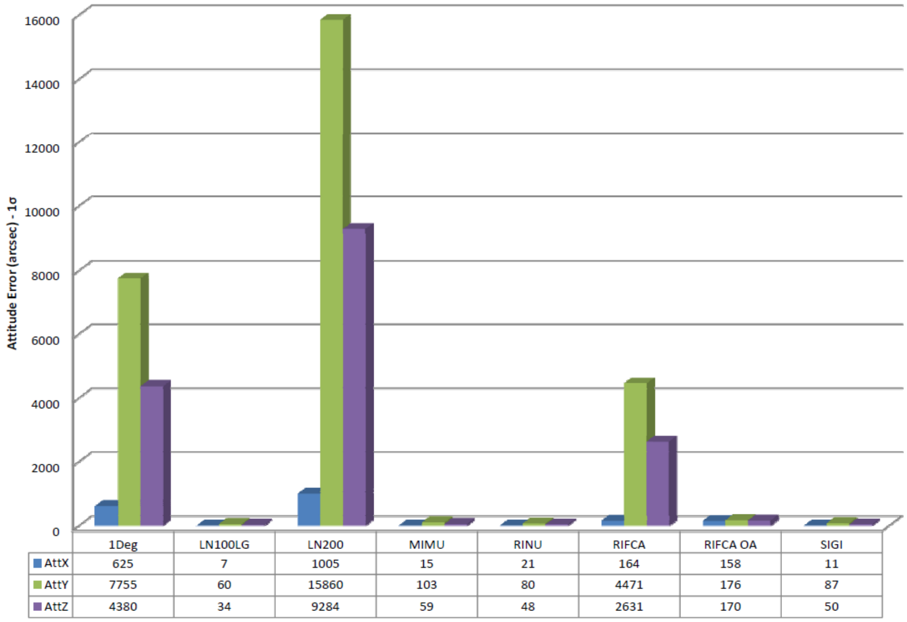

	1Deg	LN100LG	LN200	MIMU	RINU	RIFCA	RIFCA OA	SIGI
🟦 AttX	625	7	1005	15	21	164	158	11
🟩 AttY	7755	60	15860	103	80	4471	176	87
🟪 AttZ	4380	34	9284	59	48	2631	170	50

Figure 4.43

Inertial Navigation Trade, Attitude Error at Insertion, Trajectory 3

Table 4.17

Inertial Navigation Trade, Insertion Accuracy Summary, Trajectory 3

	Insertion State Error, 3σ					
	State Error Magnitude			Keplerian Error State		
	$\|\delta R_{ECI}\|$ (nmi)	$\|\delta V_{ECI}\|$ (nmi/s)	$\|\delta\Theta\|$ (arcsec)	δa (nmi)	δR_a (nmi)	$wedge$ (deg)
1Deg IMU	112.7	0.533	26790	39.1	77.4	17.0
LN100LG	0.8960	0.00421	207.0	1.67	3.28	0.067
LN200	232.5	1.102	55210	47.9	90.7	18
MIMU	1.555	0.00731	358.9	3.25	6.38	0.12
RINU	1.391	0.00584	286.2	2.09	4.00	0.072
RIFCA	65.81	0.312	15570	4.46	7.21	4.2
RIFCA Aligned	1.917	0.0106	874.7	4.15	6.95	0.10
SIGI	1.292	0.00609	302.2	1.76	3.43	0.09

From the ascent Monte Carlo results, the LN100LG, SIGI, RINU, MIMU, and RIFCA, when aided during alignment, appear to make up a class of their own for quality inertial navigation. Needless to say, these particular boxes are marketed for launch vehicles. The results allow for an incorrect interpretation of the relative quality shown between the SIGI and the RINU. For each of the trajectory sets, the SIGI shows slightly better accuracy at insertion than the RINU in both position and velocity despite the RINU having better attitude accuracy. This is not indicative of the relative quality between the two instruments. This is a difference in modeling. The RINU specification is the most well known of the candidate specification. Launch induced errors were simulated for the RINU, but there is not enough information available to do so for the SIGI. The result is the appearance that the SIGI would perform better given the same environment. This is likely not the case, but demonstrates the importance of understanding what is modeled and wariness for what is not modeled.

In addition to the inertial results, a set of candidate inertial systems was simulated with GPS aiding. To facilitate the aiding of the inertial navigation systems with GPS, a 9-state Kalman filter was developed with states for position, velocity, and attitude. During flight the filter took measurements from the GPS error model at 1Hz and updated the position and velocity states. A set of 500 Monte Carlo runs were made for each candidate system. Only results for Reference Trajectory 3, the SLS Block 0 variant are shown. Table 4.18 lists the orbit insertion state errors. Figures 4.44, 4.45, and 4.46 illustrates the insertion accuracy in terms of the state errors with GPS aiding. Note the scales are significantly smaller for the plots depicted the aided performance versus those depicting the aided performance.

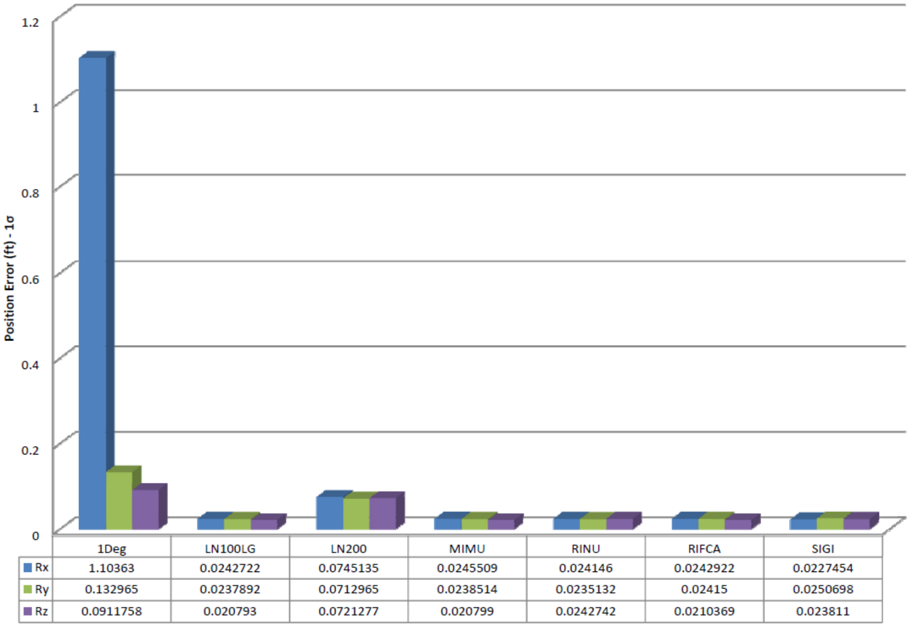

	1Deg	LN100LG	LN200	MIMU	RINU	RIFCA	SIGI
Rx	1.10363	0.0242722	0.0745135	0.0245509	0.024146	0.0242922	0.0227454
Ry	0.132965	0.0237892	0.0712965	0.0238514	0.0235132	0.02415	0.0250698
Rz	0.0911758	0.020793	0.0721277	0.020799	0.0242742	0.0210369	0.023811

Figure 4.44

Inertial Navigation Trade, Position Error at Insertion, Trajectory 3

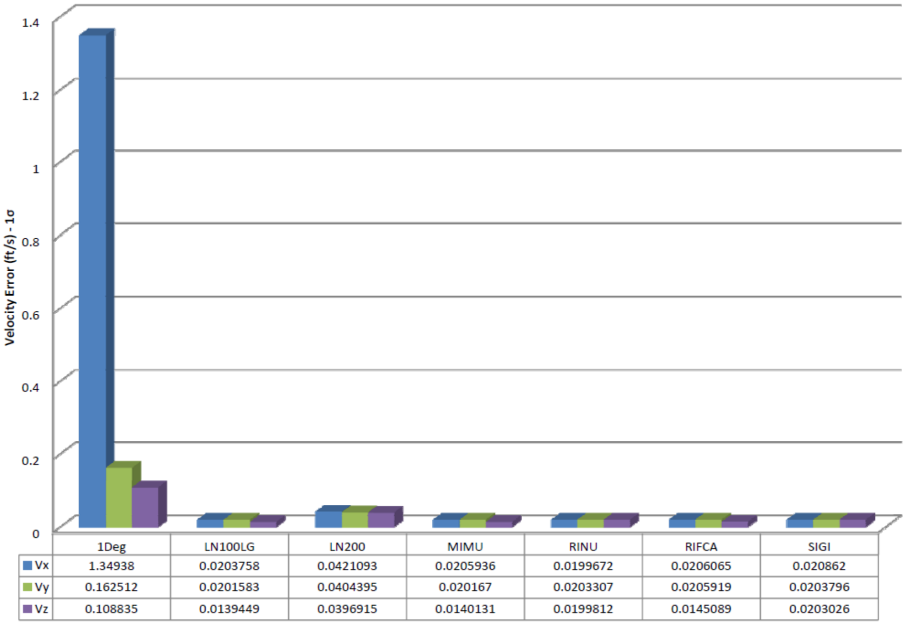

	1Deg	LN100LG	LN200	MIMU	RINU	RIFCA	SIGI
Vx	1.34938	0.0203758	0.0421093	0.0205936	0.0199672	0.0206065	0.020862
Vy	0.162512	0.0201583	0.0404395	0.020167	0.0203307	0.0205919	0.0203796
Vz	0.108835	0.0139449	0.0396915	0.0140131	0.0199812	0.0145089	0.0203026

Figure 4.45

Inertial Navigation Trade, Velocity Error at Insertion, Trajectory 3

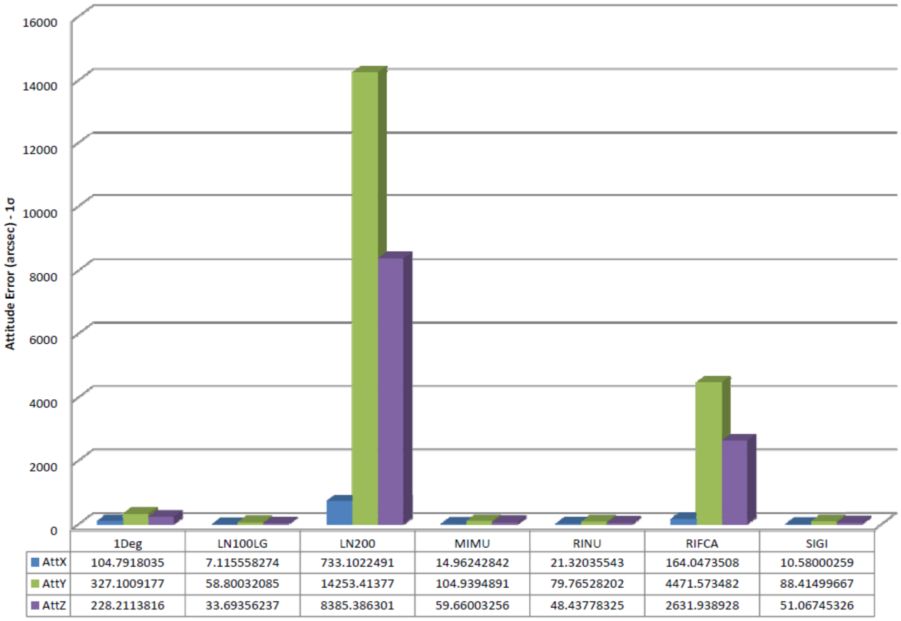

	1Deg	LN100LG	LN200	MIMU	RINU	RIFCA	SIGI
🟦 AttX	104.7918035	7.115558274	733.1022491	14.96242842	21.32035543	164.0473508	10.58000259
🟩 AttY	327.1009177	58.80032085	14253.41377	104.9394891	79.76528202	4471.573482	88.41499667
🟪 AttZ	228.2113816	33.69356237	8385.386301	59.66003256	48.43778325	2631.938928	51.06745326

Figure 4.46

Inertial Navigation Trade, Attitude Error at Insertion, Trajectory 3

Table 4.18

Inertial Navigation Trade, Insertion Accuracy Summary, Trajectory 3

	Insertion State Error, 3σ					
	State Error Magnitude			Keplerian Error State		
	$\lvert\delta R_{ECI}\rvert$ (nmi)	$\lvert\delta V_{ECI}\rvert$ (nmi/s)	$\lvert\delta\Theta\rvert$ (arcsec)	δa (nmi)	δR_a (nmi)	$wedge$ (deg)
1Deg IMU	5.5E-04	6.7E-04	1240	1.5	2.8	0.00015
LN100LG	2.0E-05	1.9E-05	204	0.021	0.041	0.00010
LN200	6.2E-05	5.4E-05	49700	0.045	0.086	0.00023
MIMU	2.0E-05	1.9E-05	365	0.022	0.042	0.00010
RINU	2.1E-05	1.9E-05	287	0.022	0.041	0.00012
RIFCA	2.0E-05	1.9E-05	15600	0.022	0.041	0.00010
SIGI	2.0E-05	2.0E-05	308	0.023	0.043	0.00015

In the unaided inertial navigation analysis, the 1Deg IMU underperformed expectations of producing less than one degree of attitude error during ascent. Time was spent tuning the 9-state Kalman filter specifically for this fictitious IMU. It was also noticed that the time allotted to coarse alignment during gyrocompassing may have been insufficient for some of the candidate boxes with poor gyro noise characteristics, by navigation standards, like the LN200. The 1Deg IMU has very good noise characteristics and a 0.023 deg/hour gyro bias. The investment of time in the 1Deg IMU can be seen in the attitude error state plot. Based upon the findings in the misalignment study, the attitude accuracy could likely be sufficient for flight control. If this were a real box, it could possibly be in the sweet spot in terms of GPS aided inertial navigation.

4.4.5 Predicted Vehicle Insertion Accuracy Impact on Payload

The navigation accuracy at orbit insertion is a sufficient metric of performance for the navigation or GN&C engineer, but there is always the question of how the error affects the overall vehicle performance and, more importantly, the payload. This section attempts to demonstrate how that question is answered within the context of the trade study. The assumption is made that the payload, for the simulated ascent vehicles, is a spacecraft or satellite which is required to correct for the insertion orbit error during a maneuver after the payload has been inserted into the target orbit and separated from the launch vehicle. Each of the reference trajectories insert into a target orbit with negative perigee altitude. A perigee raise maneuver would be required to put the payload into a stable orbit. For this analysis an arbitrary circularization maneuver at apogee was considered. The additional delta velocity required to correct for the navigation error based upon the results in the previous section were calculated over the Monte Carlo sets. The result represents the impact of the navigation error on the payload in terms of delta velocity for continued operation in LEO assuming that that the payload would be required to correct for the error. Errors in-plane and out-of-plane are considered independently.

Table 4.19 list the results for the Ares I Reference Trajectory, Trajectory 1. The table contains statistics for the change in velocity, ΔV, required to correct for the in-plane insertion error and the out-of-plane insertion error, as well as, the total ΔV. The statistics are based upon the Monte Carlo set run for each inertial instrument for each trajectory. Also included in the table are statistics for the computed mass fractions. Impulsive burns were assumed without gravity losses. The mass fractions were computed for three difference

Table 4.19

Inertial Navigation Trade, Payload Impact, Trajectory 1

	Correction ΔV (ft/s), 1σ			Mass Fraction Required for Correction		
INS	in-plane	out-of-plane	total	$I_{sp} = 250s$	$I_{sp} = 323s$	$I_{sp} = 462s$
1Deg IMU	46.1	1040	1040	0.24	0.16	0.095
LN100LG	1.64	4.97	5.19	0.00065	0.00050	0.00035
MIMU	3.15	8.48	9.08	0.0011	0.00087	0.00061
LN200	12.9	365	366	0.049	0.037	0.026
RINU	3.26	7.06	7.96	0.00099	0.00077	0.00054
RIFCA	12.9	365	366	0.049	0.037	0.026
RIFCA Aligned	11.5	10.1	15.1	0.0019	0.0015	0.0010
SIGI	1.68	7.03	7.21	0.00090	0.00069	0.00048

Table 4.20

Inertial Navigation Trade, Payload Impact, Trajectory 2

	Correction ΔV (ft/s), 1σ			Mass Fraction Required for Correction		
INS	in-plane	out-of-plane	total	$I_{sp} = 250s$	$I_{sp} = 323s$	$I_{sp} = 462s$
1Deg IMU	65.5	998	991	0.21	0.14	0.087
LN100LG	2.36	5.80	6.25	0.00078	0.00060	0.00042
LN200	74.6	1380	1370	0.26	0.18	0.11
MIMU	4.49	8.91	9.94	0.0012	0.00096	0.00067
RINU	3.76	6.76	7.66	0.00095	0.00074	0.00052
RIFCA	7.76	368	368	0.050	0.038	0.026
RIFCA Aligned	10.8	10.5	14.9	0.0019	0.0014	0.0010
SIGI	2.44	7.65	8.03	0.0010	0.00077	0.00054

Table 4.21

Inertial Navigation Trade, Payload Impact, Trajectory 3

	Correction ΔV (ft/s), 1σ			Mass Fraction Required for Correction		
INS	in-plane	out-of-plane	total	$I_{sp} = 250s$	$I_{sp} = 323s$	$I_{sp} = 462s$
1Deg IMU	100	908	890	0.18	0.12	0.076
LN100LG	4.23	5.12	6.64	0.00083	0.00064	0.00045
LN200	116	1260	1230	0.22	0.16	0.10
MIMU	8.24	8.00	11.5	0.0014	0.0011	0.00077
RINU	5.12	6.10	8.06	0.0010	0.00078	0.00054
RIFCA	8.76	332	331	0.044	0.034	0.023
RIFCA Aligned	8.57	8.39	12.0	0.0015	0.0012	0.00081
SIGI	4.40	7.02	8.22	0.0010	0.00079	0.00055

Table 4.22

Inertial Navigation Trade, Payload Impact with GPS Aiding, Trajectory 3

	Correction ΔV (ft/s), 1σ			Mass Fraction Required for Correction		
INS	in-plane	out-of-plane	total	$I_{sp} = 250s$	$I_{sp} = 323s$	$I_{sp} = 462s$
1Deg IMU	3.5	0.012	3.5	0.0004	0.0003	0.0002
LN100LG	0.053	0.0082	0.053	6.6e-6	5.1e-6	3.6e-6
LN200	0.11	0.021	0.11	1.4e-5	1.1e-5	7.5e-6
MIMU	0.054	0.0081	0.054	6.7e-6	5.2e-6	3.6e-6
RINU	0.052	0.010	0.053	6.6e-6	5.1e-6	3.6e-6
RIFCA	0.053	0.0083	0.054	6.7e-6	5.6e-6	3.6e-6
SIGI	0.055	0.011	0.056	6.9e-6	5.2e-6	3.7e-6

engine efficiencies, indicated by the specific impulse, I_{sp}. The specific numbers of 250, 323 and 462 seconds were chosen intentionally. A specific impulse of 250 seconds is in the range of solid rocket propellants. A specific impulse of 323 seconds corresponds an estimated I_{sp} for the Orion main engine to be and it does not differ greatly from the specification for the Apollo upper stage engine. The largest number corresponds to an RS-25d, or Space Shuttle Main Engine, under a certain throttle condition. Tables 4.20 and 4.21 list the results for Reference Trajectory 2 and 3. Table 4.18 contains the results from the GPS aided inertial navigation cases. As expected, they are remarkably different. The mass fractions and delta velocities show that the navigation error has a negligible impact on the payload when the navigation system is aided by GPS.

4.4.6 Trade Study Conclusions

Multiple trajectories were included in the study to span the design space given by the vehicle examples. The first Reference Trajectory is representative of an Ares I vehicle and mission. The second and third Reference Trajectories are representative of a SLS vehicle without an upper stage and the with an upper stage, respectively. As expected from the kinematic relationships for position and velocity, the errors in velocity grow as a function of the flight time and the errors in position grow as a function of the square of the flight time. This appears to be the dominant discriminator between the results for the three reference trajectories simulated. There is no discernible variation in the results to indicate a significant system non-linearity which would cause the errors to propagate differently for different trajectories within the context of the Reference Trajectories studied. The error growth in the attitude, which manifests as out-of-plane error, does appear to grow at a slightly higher rate for the Ares I trajectory relative to flight time. This may be due to the inclusion of a Roll Control System (RCS) on Ares I and the additional angular rate content associated with the use of the RCS. The effect is small.

The choice of instrument error budgets was made to span the design space with regard to existing Inertial Navigation Systems used on similar launch systems. The first observation from the analysis is a defined class of instruments suited for inertial navigation. The RINU, SIGI, MIMU, and LN100 are obviously built for inertial navigation for launch vehicle or similar systems. When external alignment is considered, the system used on the Delta IV rocket, RIFCA, also falls into this class. The inertial navigation results explicitly depict the dependence on initial alignment for accurate orbit insertion. For this reason, the LN200 and fictitious 1Deg IMU are shown to not be suitable to inertial navigation on a launch vehicle. The RIFCA falls into this class if assumed to autonomously align through gyrocompassing.

The aided inertial results really show the potential of GPS aiding for orbit insertion error reduction. In this respect, the results depict a clear paradigm shift from traditional inertial navigation. Due to the decoupling of the position and velocity state accuracy from the initial alignment, and thus the quality of the gyros, the inertial instruments all appear to perform about equally well. Further, even the poorest performing inertial instrument exceeds the best inertial navigation solution when aided by GPS position and velocity measurements. The clear conclusion is that GPS is a powerful navigation aid. From the payload impact results, the savings in terms of the delta velocity required by the payload to correct for navigation error at orbit insertion is small. The difference between a GPS aided system and a reasonable unaided system is only on the order of 3 to 12 ft/s. Beyond the direct delta velocity impact, the result implies that the cost associated with expensive inertial systems may be unjustified except in cases where autonomy is required, such as with strategic systems. This is a significant, although obvious, conclusion.

4.5 Lunar Injection/Trajectory Correction Maneuver Sensitivities

This section details the analysis performed to assess the impact of navigation errors on Lunar bound missions. The analysis is based on the SLS mission described in Chapter 2. It is assumed that the spacecraft has perfect knowledge of the state but is not in control of the vehicle until after separation with the second stage. At each burn the accumulated navigation error manifests as a guidance error, that is, an error in course. It is also assumed that at some time later, along the Trans-Lunar Injection (TLI) trajectory when the spacecraft is in control of the vehicle, the spacecraft will have to correct course to the intended course.

This mid-course correction is called the Trans-Lunar Correction Maneuver (TCM). The delta velocity required to complete the TCM is treated as a metric from which to gauge the impact of the navigation system errors on the Lunar mission.

The method of estimating the TCM is taken from the work of Dukeman and Hill.[15][27] The method is derived from Battin's Fixed-Time-of-Arrival Orbit Corrections method. [3] For determining the size of the TCM, the impact of the perturbation to the trajectory must be estimated.

To relate the error in the trajectory at time t_0 to the error at some later time t, the state transition matrix, Φ_{t,t_0}, can be used. The state transition matrix, Φ_{t,t_0}, is a function of the linearized trajectory dynamics, f_x, about the reference trajectory and is used to relate the state error at time t_0, $x(t_0)$, to the state error at some later time, $x(t)$. The state transition matrix is defined in general by Equation (4.26) for the state defined for this case by Equation (4.27).

$$x(t) = \frac{\partial x(t)}{\partial x(t_0)} x(t_0) = \Phi_{t,t_0} x(t_0) \tag{4.26}$$

$$x(t) = \begin{bmatrix} \delta r(t) \\ \delta v(t) \end{bmatrix} \tag{4.27}$$

The state transition matrix can then be defined in terms of Battin and Lanning's partitioned state transition matrix, Equation (4.29). Equation (4.28) defines the system with the partitioned state transition matrix. [4] [3]

$$\Phi_{t,t_0} = \begin{bmatrix} \tilde{R}^*_{t,t_0} & R^*_{t,t_0} \\ \tilde{V}^*_{t,t_0} & V^*_{t,t_0} \end{bmatrix} = \begin{bmatrix} \frac{\partial r(t)}{\partial r(t_0)} & \frac{\partial r(t)}{\partial v(t_0)} \\ \frac{\partial v(t)}{\partial r(t_0)} & \frac{\partial v(t)}{\partial v(t_0)} \end{bmatrix} \tag{4.28}$$

$$\begin{bmatrix} \delta r(t) \\ \delta v(t) \end{bmatrix} = \begin{bmatrix} \tilde{R}^*_{t,t_0} & R^*_{t,t_0} \\ \tilde{V}^*_{t,t_0} & V^*_{t,t_0} \end{bmatrix} \begin{bmatrix} \delta r(t_0) \\ \delta v(t_0) \end{bmatrix} \tag{4.29}$$

If fixed-time-of-arrival is assumed, then $\delta r(t) = 0$. The delta velocity required is the difference in the actual velocity perturbation at the time the TCM is performed due to navigation error at the TLI maneuver, $\delta v(t^-)$, and the velocity required to intercept, $\delta v(t^+)$, given by Equation (4.30). The perturbations are known at t_0. For this analysis, the perturbation is the navigation error and t_0 is the end of the TLI burn at which point the second stage navigation error becomes the spacecrafts error in course.

$$\Delta v_{TCM}(t) = \delta v(t^+) - \delta v(t^-) \tag{4.30}$$

$$\Delta v_{TCM}(t) = \Big(-\left(R^*_{t^+,t^-}\right)^{-1} \tilde{R}^*_{t^+,t^-} \delta r(t^-)\Big) - \Big(\tilde{V}^*_{t^-,t_0} \delta r(t_0) + V^*_{t^-,t_0} \delta v(t_0)\Big) \tag{4.31}$$

Equation (4.31) differs from Battin's explanation of how to obtain the velocity to intercept in that Battin uses different components of the partitioned state transition matrix. Simulation of Battin's version produces significantly different, and erroneous, results. The variable $\delta r(t^-)$ represents the perturbation at the time when the correction is applied. Equation (4.32) relates the perturbation at the point where the mid-course correction is applied to the TLI perturbation.

$$\delta r(t^-) = \tilde{R}^*_{t^-,t_0} \delta r(t_0) + R^*_{t^-,t_0} \delta v(t_0) \tag{4.32}$$

The state transition matrix is obtained by integrating the variational equations over the reference trajectory. The partition components can be obtained from the state transition matrix directly for t_0 or by Equation (4.33).

$$\Phi_{t_a,t_b} = \Phi_{t_a,t_0} (\Phi_{t_b,t_0})^{-1} \tag{4.33}$$

The reference trajectory in this case was a 3-DOF Lunar free return trajectory produced in Copernicus. Along the trajectory, the state transition matrix was computed by integrating the variational equations for the Sun-Earth-Moon system. The navigation perturbations, or error, were sampled from an error covariance matrix representing the predicted navigation error ellipsoid at the end of the TLI maneuver. To produce the TLI error covariance, a series of Monte Carlo analyses were performed consisting of 500 runs per instrument error budget and navigation configuration being simulated. The initial Monte Carlo analysis was performed with the SLS Block 0 trajectory with high apogee insertion orbit.

To propagate the error statistics from the LEO ascent target orbit to the end of the TLI maneuver, another 500 run Monte Carlo analysis was performed for the second stage flight. Initially a 3DOF trajectory generated in Copernicus was used for this leg of the analysis. Attitude rates were added to the trajectory consistent with a fixed attitude relative to the ECI radius vector and a vector normal to the plane developed by the ECI position and velocity vectors. The analysis was eventually re-run with a 6-DOF trajectory developed in Maveric with simulated attitude maneuvers. Plots of the trajectory specific force and angular rates are shown in Figure 4.47 and 4.48. The position, velocity and attitude state time history is depicted in Figure 4.49, 4.50, and 4.51. The trajectory from the 6-DOF simulation contained attitude maneuvers that the original trajectory generated from the 3-DOF trajectory did not. This is shown in Figure 4.51. The attitude maneuvers actually reduced the navigation error due to the canceling effect from the accelerometer biases being integrated in different directions over the flight. The attitude maneuvers are also well depicted in Figure 4.48

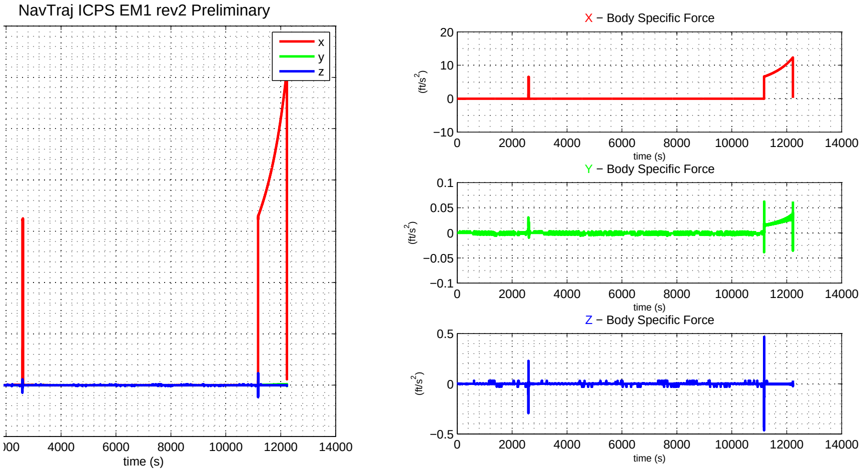

Figure 4.47

ICPS Analysis, 6DOF Trajectory, Specific Force

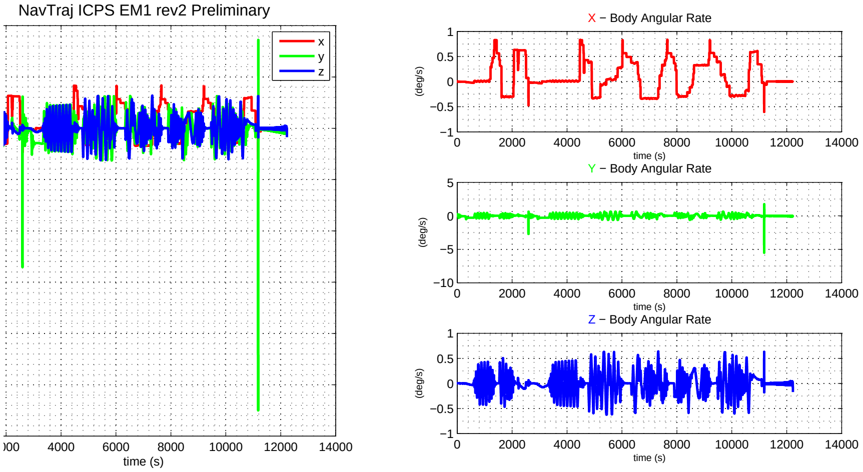

Figure 4.48

ICPS Analysis, 6DOF Trajectory, Angular Rate

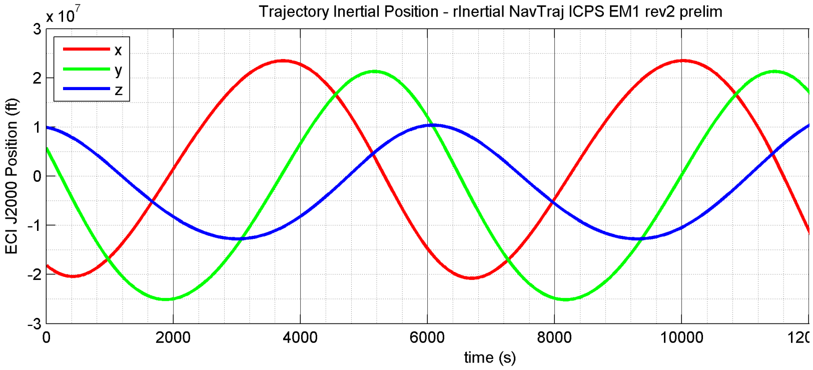

Figure 4.49

ICPS Analysis, 6DOF Trajectory, Position

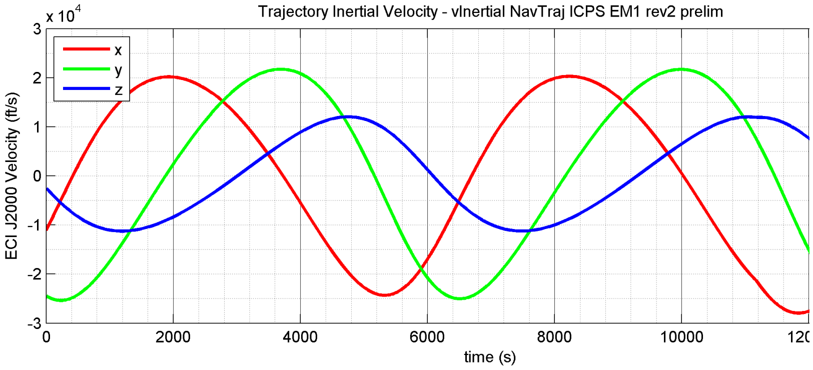

Figure 4.50

ICPS Analysis, 6DOF Trajectory, Velocity

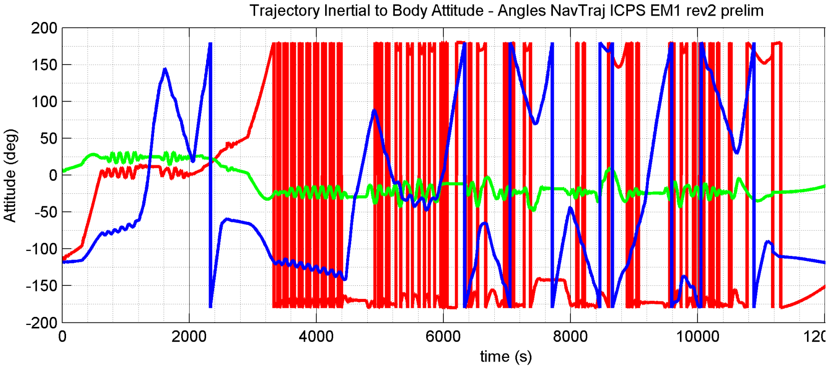

Figure 4.51

ICPS Analysis, 6DOF Trajectory, Attitude

To accommodate the differences in trajectory epochs, initial state, and final state between the ascent and second stage trajectories, the errors were transformed into a coordinate frame that was a function of the trajectory and independent of the inertial position of the Earth and the vehicle inertial state. The orthogonal coordinate frame was defined, consistent with the fixed attitude maneuver, as having one axis in the direction of the Earth relative position vector and the second axis defined as being normal to the vehicle velocity and radius vectors. This is sometimes referred to as a UVW frame or a Radial, Tangential, Normal (RTN) frame. The second stage trajectory ended at engine shutdown for the TLI maneuver. Error covariance matrices were produced for each configuration to initialize the algorithm used for estimating the magnitude of the TCM maneuver.

The TCM correction maneuver prediction algorithm was performed as a Monte Carlo analysis. The navigation error covariance matrices were each randomly sampled from 2000 times for 2000 random sets of correctly correlated position and velocity state perturbations. The state transition matrix was developed along the free lunar return trajectory and a velocity correction, ΔV_{TCM}, was computed at 1 hour intervals along the trajectory for each set of the 2000 sets of position and velocity perturbations. The result is shown in Figures 4.52 and 4.53.

The analysis which produced the results contained in Figures 4.52 and 4.53 assumes that the trajectory course correction occurs at a fixed time. The lunar sphere of influence is taken to be the intercept point where the perturbed and the nominal trajectories converge. The correction is assumed to consist of a single maneuver performed at the time indicated on the plot without re-optimization. This is a considered to be a conservative approach. It is possible that the delta velocity requirement could be relaxed with re-optimization of the correction maneuver while in orbit if the time of arrival and the time of correction were allowed to vary. Even considering re-optimization, the GPS aided solution would likely remain the optimal choice for reduced impact to payload in terms of the delta velocity required for trajectory correction due to navigation error.

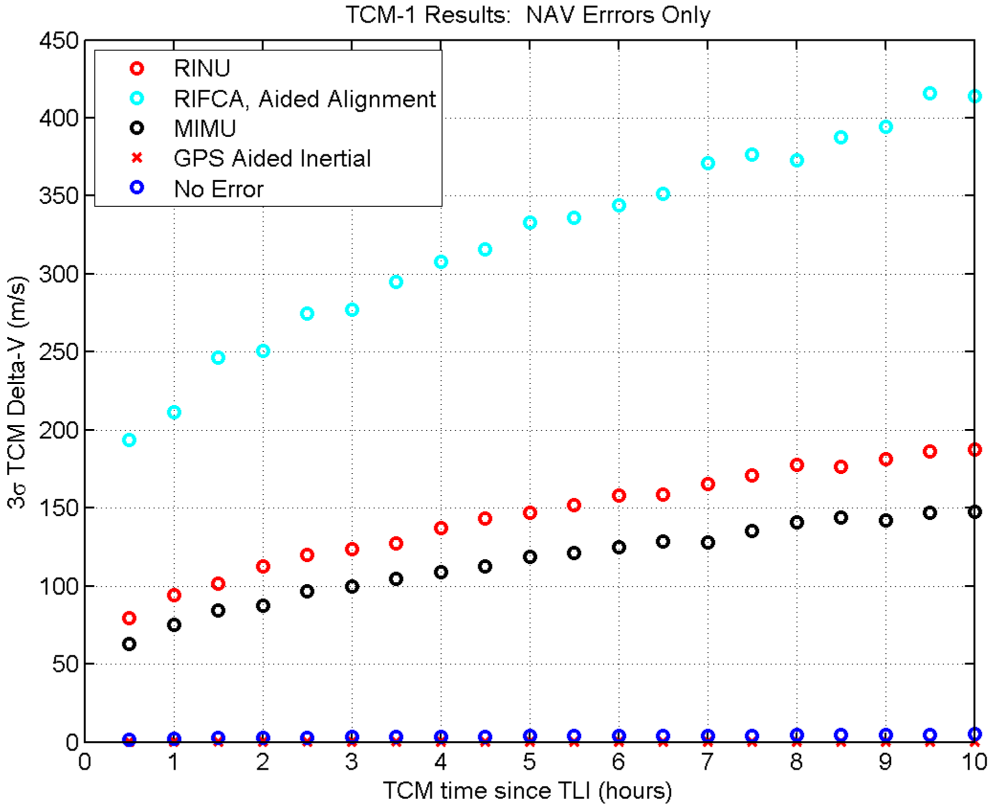

Figure 4.52

ICPS Analysis, TCM ΔV from Navigation Error

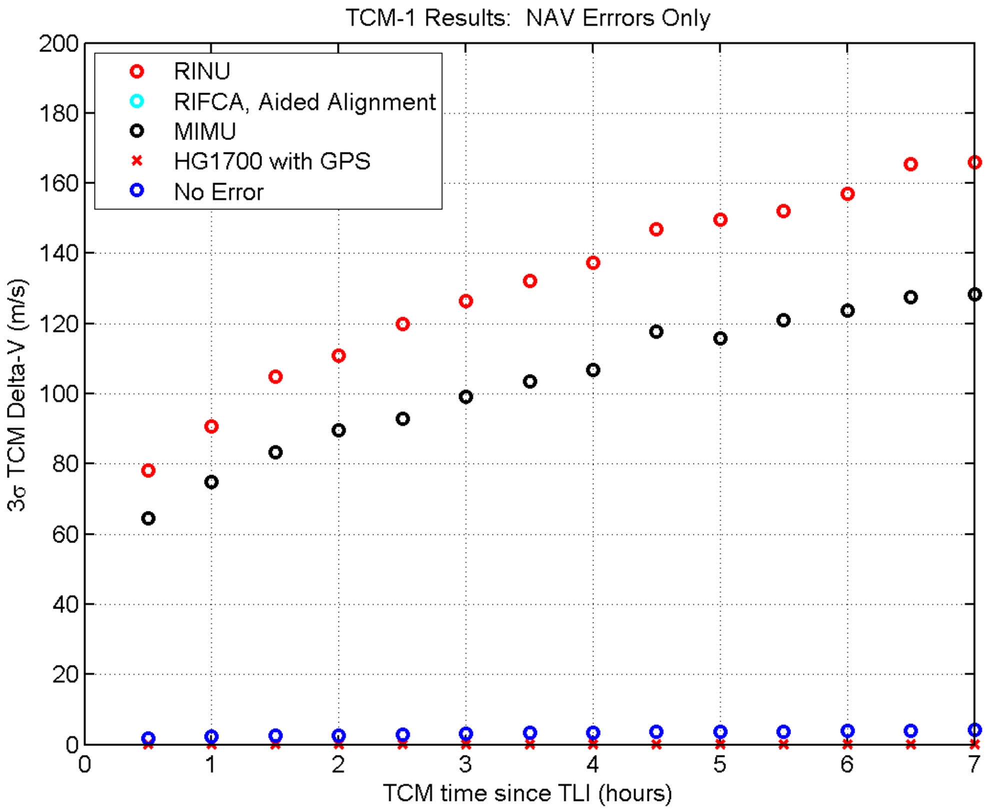

Figure 4.53

ICPS Analysis, TCM ΔV from Navigation Error, Close-up

CHAPTER 5

CONCLUSIONS

This work takes an end-to-end look at preliminary Navigation system design and development. The discussion ranges from the assessment of vehicle level requirements and vehicle level sensitivities to the assessment of the performance of specific navigation hardware choices and their impact to mission success. The objectives of the thesis were stated in Chapter 1. Here, the bulletized list is repeated. This thesis will:

- identify constraints and Navigation sub-system requirements from vehicle level requirements
- define a navigation system design and analysis process from a systems level approach
- define modeling and analysis techniques for launch vehicle navigation
- define navigation sub-system sensitivities and trades

Chapter 2 presented a vehicle system level approach to navigation. Types of launch vehicle navigation were introduced in detail. Vehicle and system level requirements typical of launch vehicles were presented. Those system level requirements were decomposed. Vehicle level constraints were presented and an approach to sizing the Navigation system accuracy was discussed. A design and analysis cycle was presented which incorporated a navigation system and integrated vehicle analysis process. The process is complete and self-contained offering mitigation strategies for all possible outcomes within the design and analysis cycle.

Also in Chapter 2, the different parameterizations of the vehicle and navigation accuracy were examined. Dominant drivers and constraints were identified and data from simulation was presented for evidence. It was found that the vehicle accuracy is constrained primarily by the impact to the payload and the re-entry footprint. The vehicle orbit insertion accuracy was shown to be a function of both constraints. The insertion accuracy was shown to be primarily dependent on the navigation solution error and the upper stage shutdown transient uncertainty. Metrics were introduced for assessing the impact to the payload. Models were developed to assess the impact of insertion accuracy on the re-entry footprint.

Software tools were introduced. The design and analysis cycle developed recommends open-loop design tools for navigation analysis, including analysis of the initial alignment process. The design and analysis cycle requires the integration of the model and performance into the closed loop simulation with iteration.

Navigation principal technologies were introduced. The historic concepts of position fixing and dead reckoning were introduced and applied to modern navigation. The concept of inertial navigation was introduced and the two categories of implementation were discussed. The concept of marrying the two navigation principal technologies was introduced in the form of aided inertial navigation. The possible benefit of combining these two distinctly different methods was described.

Chapter 3 focused on implementation of the principal navigation technologies discussed in Chapter 2. Within Chapter 3, the INS model is developed for navigation and vehicle level analysis in accordance with the model based design paradigm. Model components pertinent to the simulation of a Navigation system were presented with appropriate detail given to the flow of data through the model. The INS model was described to lend insight into the mechanization of the Navigation system. An extensive instrument error model was defined with examples and navigation algorithms are presented. The navigation algorithms consisted of inertial navigation and initialization as well as an aided inertial algorithm.

Chapter 4, began by introducing the primary analysis method used. The errors associated with the analysis method are assessed and a model is developed to bound the error due to sampling. The analysis method is then used to decompose the navigation accuracy defined in Chapter 2 and categorize the navigation error by contribution from inherent error sources. In doing so, a firm understanding of the dominant sensitivities, both in terms of error sources and operations, is acquired. The sensitivity study makes evident the criticality of the initial attitude error for the inertial navigation system. Gyro bias and gyro random walk are shown to be the dominant error sources in terms of the overall impact on the initial alignment and therefore on the insertion accuracy, particularly in the out-of-plane portion of the error. For the in-plane error, high sensitivity to the modeled accelerometer scale factor errors was shown. For the aided inertial navigation sensitivity study, the navigation solution showed almost no sensitivity to the instrument error in the state except in attitude. The integration of GPS measurements was shown to effectively decouple the position and velocity state errors from the initial attitude error. The misalignment study performed for Ares I and SLS showed a relaxed sensitivity to physical misalignment error, suggesting a higher than expected tolerance to large attitude errors during flight. The combination of the misalignment study findings and the GPS aided inertial sensitivity study findings suggest that excellent gyro performance characteristics can be traded for the integration of GPS onto the vehicle and into the navigation solution for an improvement in performance over all of the inertial systems reviewed.

In the trade study, a survey of available inertial hardware is performed. Representative mission trajectories were generated. Inertial navigation performance was assessed for example missions on the representative mission trajectories, given estimated sensor specifications from commercially available inertial hardware. The trade went to the level of the requirements analysis in Chapter 2 by assessing the potential impact to the payload in terms of delta velocity and mass fraction for feasible engine designs. The analysis in Chapter 4 made it apparent that there exists a defined distinction within the industry for inertial hardware suitable for launch vehicle inertial navigation and inertial hardware not designed for launch vehicle inertial navigation. The results also showed the amazing capability of an aided inertial navigation system. Even the poorest performing inertial navigation system performed better than the best inertial system with aiding. For the lunar bound missions, the navigation accuracy was assessed relative to the fuel cost to correct for the navigation error on the way to the moon. The impact of aiding in this situation could mean the difference between a mission which is feasible versus one which is not.

REFERENCES

[1] "Atlas V Launch Services Users Guide," United Launch Alliance, Centennial, CO, Mar. 2010, Revision 11.

[2] R. R. Bate, D. D. Mueller, and J. E. White, *Fundamentals of Astrodynamics*, Dover publications, Dover, NY, 1971, pg. 422 with errata.

[3] R. H. Battin, *An Introduction to the Mathematics and Methods of Astrodynamics*, American Institute of Aeronautics and Astronautics, 1999.

[4] R. H. Battin and J. H. Laning, "A Navigation Theory for Round-Trip Reconnaissance Missions to Venus and Mars," *Planetary and Space Science*, vol. 7, 1961, pp. 40–56.

[5] W. P. Bernard, "SNAP to NEAT Comparisons," Unpublished, Mar. 2007.

[6] W. P. Bernard, "Covariance to Monte Carlo Comparisons," Unpublished, Mar. 2009.

[7] W. P. Bernard, "Verification of MAVERIC Navigation Code," Technical Memorandum TM_NAV_DCI_037. Dynamic Concepts, Inc, Feb. 2009.

[8] J. Bortz, "A New Mathematical Formulation for Strapdown Inertial Navigation," *Aerospace and Electronic Systems, IEEE Transactions on*, vol. AES-7, no. 1, 1971, pp. 61–66.

[9] M. Carter, J. Bush, S. Hough, E. Oliver, and J. Compton, "Model-Based Design Considerations for GN&C Flight Software Development," Presented to NASA Marshall Space Flight Center GN&C as part of Model Based Design Pilot Activity, Nov. 2010.

[10] D. A. Cicci, *Mathematical Modeling of Inertial Measurement Units*, Technical Report, Dynamic Concepts, Inc., Aug. 2006.

[11] J. F. Connolly, "Constellation Program Overview," Constellation Program Office, Oct. 2006.

[12] J. L. Crassidis and J. L. Junkins, *Optimal Estimation of Dynamic Systems*, vol. 24, Chapman & Hall, 2011.

[13] "Delta IV Payload Planners Guide," United Launch Alliance, Centennial, CO, Sept. 2007, 06H0233.

[14] R. C. Dorf and R. H. Bishop, *Modern Control Systems (10th Edition)*, 10 edition, Prentice Hall, 4 2004.

[15] G. Dukeman, "Computation of State Transition Matrices and Application to Trans-Lunar Trajectory Mid-Course Correction Analysis," Unpublished, July 2012.

[16] G. Dukeman, "Orbit Insertion Accuracy Sensitivities," Presented to SLS-Trade-021 Team, Jan. 2013.

[17] "Fault Tolerant Inertial Navigation Unit, Next Generation High Accuracy Navigation System," Honeywell Defense and Space, Clearwater, FL, Dec. 2006.

[18] A. Gelb, ed., *Applied Optimal Estimation*, MIT press, Cambridge, MA, May 1974.

[19] "Sensor Misalignments," Constellation Program Ares I Guidance, Navigation, and Control (GN&C) System Design Document Volume III: GN&C Analysis, Section 4.1.6. CxP 72069-03. pg 212., June 2008.

[20] J. L. Goodman, "Lessons Learned From Flights of Off the Shelf Aviation Navigation Units on the Space Shuttle," *Joint Navigation Conference, NASA Johnson Space Center*, 2002, pp. 6–9.

[21] L. Goodman and A. Robinson, "Effect of Finite Rotations on Gyroscopic Sensing Devices," ASME, 1957.

[22] M. S. Grewal, L. R. Weill, and A. P. Andrews, *Global Positioning Systems, Inertial Navigation, and Integration*, Wiley-Interscience, 2001.

[23] J. H. Halton, "A Retrospective and Prospective Survey of the Monte Carlo Method," *Siam Review*, vol. 12, no. 1, 1970, pp. 1–63.

[24] J. Hanson, "DAC-1 Requirements Analysis," Upublished, 2007.

[25] J. Hanson and B. Beard, *Applying Monte Carlo Simulation to Launch Vehicle Design and Requirements Analysis*, NASA/TP 2010-216447, Marchall Space Flight Center, Huntsville, AL, Sept. 2010.

[26] J. Hanson and C. Hall, "Learning About Ares I from Monte Carlo Simulation," *AIAA Guidance, Navigation and Control Conference and Exhibit*, Guidance, Navigation, and Control and Co-located Conferences, American Institute of Aeronautics and Astronautics, Aug. 2008.

[27] A. Hill, "TCM_deltaV.m: Trajectory Correction Maneuver Delta-V Estimate," Unpublished, July 2012.

[28] G. Holt and C. D Souza, "Orion Absolute Navigation System Progress and Challenges.," *Papers - American Institute of Aeronautics and Astronautics*, 2012, vol. 7 of *American Institute of Aeronautics and Astronautics Guidance, Navigation, and Control Conference*, pp. 5215 – 5231.

[29] M. B. Ignagni, "Optimal Strapdown Attitude Integration Algorithms," *American Institute of Aeronautics and Astronautics, Journal of Guidance, Control, and Dynamics*, vol. 13, no. 2, Mar. 1990, pp. 363–369.

[30] F. James, "Monte Carlo Theory and Practice," *Reports on Progress in Physics*, vol. 43, no. 9, 2000, p. 1145.

[31] J. Jang, R. Hall, N. Bedrossian, and C. Hall, "Ares-I Bending Filter Design Using A Constrained Optimization Approach," *AIAA Guidance, Navigation and Control Conference and Exhibit*, Guidance, Navigation, and Control and Co-located Conferences, American Institute of Aeronautics and Astronautics, Aug. 2008.

[32] A. H. Jazwinski, *Stochastic Processes and Filtering Theory*, Dover Publications, 11 2007.

[33] E. D. Kaplan and C. J. Hegarty, *Understanding GPS: Principles and Applications*, 2 edition, Artech House Publishers, 11 2005.

[34] M. Lehman, *This High Man: The life of Robert H. Goddard*, Farrar, Straus, 1963.

[35] "LN-100LG, Launch and Reentry Vehicle GPS-Inertial Navigation System," Northrop Grumman Corporation Navigation Systems, Woodland Hills, CA, 2000, 22944 LN100LG/05-06/2000/Crawford.

[36] "LN-100G, Embedded INS/GPS (EGI)," Northrop Grumman, Navigation and Maritime Systems, Woodland Hills, CA, 2013.

[37] "LN-200 FOG Family, Advanced Airborne IMU/AHRS," Northrop Grumman, Navigation and Maritime Systems, Woodland Hills, CA, 2013.

[38] "LN-200S Inertial Measurement Unit," Litton Space, Launch & Strategic Systems, Goleta, CA, Jan. 2000.

[39] "LN-251 Advanced Airborne INS/GPS (EGI)," Northrop Grumman, Navigation and Maritime Systems, Woodland Hills, CA, 2013.

[40] D. MacKenzie, *Inventing Accuracy: A Historical Sociology of Nuclear Missile Guidance*, MIT Press, 1993.

[41] B. Malay, D. Gaylor, and G. Davis, "Stellar-Aided Inertial Navigation Systems for Lunar and Mars Exploration," *Flight Mechanics/Estimation Theory Symposium*, Greenbelt, MD, 2005, NASA Goddard Space Flight Center.

[42] J. McCarter, "MAVERIC Version 3.6 User's Guide," DESE Research, Inc., June 2009.

[43] R. A. McKern, *A Study of Transformation Algorithms for Use in a Digital Computer*, doctoral dissertation, Massachusetts Institute of Technology, 1968.

[44] "MIMU, Minature Inertial Measurement Unit," Honeywell Defense and Space, Clearwater, FL, Sept. 2003.

[45] F. C. Mish, ed., *The Merriam-Webster Dictionary*, Merriam-Webster, Inc., Springfielf, MA, 1997.

[46] O. Montenbruck and E. Gill, *Satellite Orbits: Models, Methods and Applications*, Springer, 2005.

[47] D. C. Montgomery and G. C. Runger, *Applied Statistics and Probability for Engineers*, 3 edition, Wiley, 1 2003.

[48] "Process for Limiting Orbital Debris," NASA-STD 8719.14, July 2009.

[49] D. Odette, "Analysis of Ares I Sensitivity to Sensor-to-Body Axes Uncertainty," Technical Memorandum, EV42-02. Guidance, Navigation and Mission Analysis Branch. Marshall Space Flight Center, July 2008.

[50] D. Odette, "Sensitivity Analysis of IMU Alignment Error," Technical Memorandum, Qualis Corporation, July 2008.

[51] T. E. Oliver, "NEAT-Draper Test Case 1," Technical Memorandum TM_NAV_DCI_018. Dynamic Concepts, Inc, Dec. 2007.

[52] T. E. Oliver, "MAVERiC 3.4 Sensor Model," Technical Memorandum TM_NAV_DCI_021, Dynamic Concepts, Inc, Mar. 2008.

[53] T. E. Oliver, "NEAT-Draper Test Case 1," Technical Memorandum TM_NAV_DCI_024. Dynamic Concepts, Inc, Apr. 2008.

[54] T. E. Oliver, "NEAT-Draper Test Case 2," Technical Memorandum TM_NAV_DCI_023. Dynamic Concepts, Inc, Apr. 2008.

[55] T. E. Oliver, "Dynamic Concepts, Inc. (DCI) GN&C Group Capability, Navigation," Dynamic Concepts, Inc., Feb. 2010.

[56] T. E. Oliver, "AFSIM: ICPS Preliminary Navigation Planning for DAC1," Presented to the SLS Ascent Flight System Integration Group (AFSIG), NASA Marshall Space Flight Center, Nov. 2011.

[57] T. E. Oliver, "Review of Flight Design and Dynamics Shuttle GPS Post-Flight Reports," Unpublished. Presented to SLS-Trade-021 Trade Team, NASA Marshall Space Flight Center, Dec. 2011.

[58] T. E. Oliver, "Orbit Insertion Accuracy Preliminary TD1A (3.9.005) MC Results and Navigation Sensitivities," Presented to SLS-Trade-021 Team, NASA Marshall Space Flight Center, Jan. 2013.

[59] T. E. Oliver and W. P. Bernard, "NEAT User's Manual Version 1.06," Dynamic Concepts, Inc., July 2007.

[60] T. E. Oliver, W. P. Bernard, C. Zimmerman, and J. Chuang, "Sensor Modeling, TD7 and Beyond," Presented to Marshall Space Flight Center GN&C Panel, Dec. 2009.

[61] T. E. Oliver and B. Burger, "RINU Sensor to Body Misalignment Study," Technical Memorandum TM_NAV_DCI_025_Rev01. Dynamic Concepts, Inc, July 2008.

[62] T. E. Oliver and A. Hill, "HLV RAC1 - Insertion Accuracy Trade," Unpublished, Jan. 2011.

[63] T. E. Oliver and A. Hill, "RAC1 Team 2 Insight, Insertion Accuracy and Footprint," Unpublished, Prepared for Heavy Lift Vehicle Requirements Analysis Cycle, Team 2, Jan. 2012.

[64] J. Orr and E. Oliver, "Evaluation of RINU Aliasing Effects," Presented by SLS Vehicle Managment Discipline Lead Engineer to SLS Chief Engineer Board, NASA Marshall Space Flight Center, Dec. 2011.

[65] M. Phillips, J. Hanson, T. Schmitt, G. Dukeman, J. Hays, A. Hill, and J. Garcia, "Preliminary Performance Analyses of the Constellation Program ARES I Crew Launch Vehicle (AAS 07-058)," *Advances in Astronautical Sciences*, vol. 128, 2007, p. 437.

[66] "Space & Navigation, Redundant Inertial Flight Control Assembly," L-3 Communication, Space and Navigation, Bud Lake, NJ, Mar. 2008.

[67] "Are Theodolites Still Used Today?," http://forum.nasaspaceflight.com/index.php?topic=3362.0, Forum Post.

[68] R. M. Rogers, "Navigation Sensor Models," *Applied Mathematics in Integrated Navigation Systems, Second Edition*, AIAA Education Series, American Institute of Aeronautics and Astronautics, Jan. 2003, pp. 101–115.

[69] K. M. Roscoe, "Equivalency Between Strapdown Inertial Navigation Coning and Sculling Integrals/Algorithms," *Journal of Guidance, Control, and Dynamics*, vol. 24, no. 2, 2001, pp. 201–205.

[70] R. Sablynski and R. Pordon, "A Report on the Flight of Delta II's Redundant Inertial Flight Control Assembly (RIFCA)," *Position Location and Navigation Symposium, IEEE 1998*, 1998, pp. 286–293.

[71] P. G. Savage, "Strapdown Inertial Navigation Integration Algorithm Design Part 1: Attitude Algorithms," *Journal of Guidance, Control, and Dynamics*, vol. 21, no. 1, Jan. 1998, pp. 19–28.

[72] P. G. Savage, "Analytical Modeling of Sensor Quantization in Strapdown Inertial Navigation Error Equations," *Journal of Guidance, Control, and Dynamics*, vol. 25, no. 5, Sept. 2002, pp. 833–842.

[73] P. G. Savage, *Introduction to Strapdown Inertial Navigation Systems*, Strapdown Associates, Maple Plain, Minn., 2010.

[74] "SIGI - Space Integrated GPS/INS, Inertial Navigation System with Embedded GPS Receiver," Honeywell Defense and Space, Clearwater, FL, Dec. 2006.

[75] J. Singer, "Space Launch System (SLS) Program Overview," Advanced Development NASA Research Announcement, Industry and Academia Day, Feb. 2012.

[76] W. Stockwell, "Angular Random Walk," Crossbow Technology, Inc., 2008.

[77] S. Tamblyn, J. Henry, and E. King, "A Model-Based Design and Testing Approach for Orion GN&C Flight Software Development," *Aerospace Conference, 2010 IEEE*. The Institute of Electrical and Electronics Engineers, 2010, pp. 1–12.

[78] B. Tapley, J. Ries, S. Bettadpur, D. Chambers, M. Cheng, F. Condi, B. Gunter, Z. Kang, P. Nagel, R. Pastor, T. Pekker, S. Poole, and F. Wang, "GGM02 An Improved Earth Gravity Field Model from GRACE," *Journal of Geodesy*, vol. 79, 2005, pp. 467–478.

[79] B. Tapley, B. Schutz, and G. H. Born, *Statistical Orbit Determination*, Academic Press, 2004.

[80] D. H. Titterton, *Strapdown Inertial Navigation Technology*, second edition, American Institute of Aeronautics and Astronautics, 2004.

[81] *MIL-STD-1750a: Military Standard Sixteen-Bit Computer Instruction Set Architecture*, United States Air Force, July 1980.

[82] M. Vajta, "Some Remarks on Padé-Approximations," *Proc. 3rd TEMPUSINTCOM Symp. Intelligent Systems in Control and Measurement*, vol. 6, no. 2, 2000, pp. 53–58.

[83] H. Wang and T. Williams, "Strategic Inertial Navigation Systems - High-Accuracy Inertially Stabilized Platforms for Hostile Environments," *Control Systems, IEEE*, vol. 28, no. 1, 2008, pp. 65–85.

[84] S. Weir, Kent A Neale and S. Weir, “Strapdown Navigation Analysis Program User’s Manual, Volume I,” Control Dynamics Company, Nov. 1989.

[85] J. Williams, J. S. Senent, and D. E. Lee, “Recent Improvements to the Copernicus Trajectory Design and Optimization System (AAS 12-236).,” *Advances in the Astronautical Sciences*, 2012, vol. 143 of *Spaceflight mechanics 2012*, pp. 1977 – 1998.

[86] J. Wright, R.J. and J. Sponnick, “A Ring Laser Gyro Based Navigator for Space Launch Vehicle Guidance,” *Aerospace and Electronic Systems Magazine, IEEE*, vol. 4, no. 3, 1989, pp. 29–38.